SILICON DANGLING BOND CHAINS

by

JOHN A. WOOD

A thesis submitted in partial fulfillment of the requirements for the degree of
Master of Science

Department of Physics
University of Alberta

ABSTRACT

We present the characterization of close-spaced linear dangling bond structures, or dangling bond chains, two to seven dangling bonds long, on a hydrogen terminated silicon (100)-2x1 surface using a scanning tunnelling microscope. Constant height differential conductance maps reveal their local density of states. We demonstrate maximal charging configurations for odd numbered chains, rendering dangling bonds of the chain alternately negatively and non-negatively charged. Perturbing a chain electrostatically with negatively charged single dangling bonds, we find that we significantly change the electronic structure of the chain, shifting its electronic state density away from the perturbing charge. Turning the single dangling bond into a bare dimer, the chain takes on its unperturbed character, proving that bare dimers do not support localized charge. Using the differential conductance mapping technique, we measure the energetic position of an unexplained bright feature often seen between two dangling bonds.

PREFACE

Some experimental data found in Chapter 6 and 7, involving the characterization of DB chains and the perturbation of the 7 DB chain respectively, have appeared in Wood et al. [1].

Experimental data on the negative differential resistance of an isolated dangling bond, specifically the I–V curve and the constant height image found in Figure 4.4, was collected in Rashidi et al. [2].

Figure 4.3 is an edited version of a figure found in the supplementary section of Taucer et al. [3]. The ball and stick model of H-Si(100)-2x1, found in Figure 4.1, was made by Dr. Mohammad Koleini. Figure 8.1 is original, but its layout is a replication of a figure found in Schofield et al. [4].

There must always be room for coincidence, Win had maintained. When there's not, you're probably well into apophenia, each thing then perceived as part of an overarching pattern of conspiracy.

—William Gibson, *Pattern Recognition*

ACKNOWLEDGEMENTS

My family has given me that which is innumerable and immeasurable. Of it, I'd like to thank my mother for the food and the Star Trek, my father for the garage full of junk and the early morning coffee visits, my brother for the raucous play, and my sister for the pastries and the books.

The group could not have been more supportive and thrilling to work with. Thanks to each of you: Erika Lloyd, Taleana Huff, Roshan Achal, Wyatt Vine, Jeremy Croshaw, Dr. Bruno Martins, Dr. Hatem Labidi, Dr. Marco Taucer, Dr. Isil Oxfidan, Dr. Mohammad Koleini, Dr. Hedieh Kalachahi, Dr. Paul Piva, Dr. Radovan Urban, and Dr. Jason Pitters, for the stimulating discussion and the depths of background knowledge available to plumb. Especially, I want to thank Martin Cloutier and Mark Salomons for helping me (and us all) operate and maintain the highly complex machines that we use daily. Our work would be impossible without your technical bedrock.

Dr. Mohammad Rashidi, or Moe, was a constant companion in this work. He taught me how to use the LT2, from tip and sample preparation to DB patterning to dI/dV mapping. His insight, experimental tenacity, and gaiety were indispensable in the production of these results.

Finally, I'd like to thank my supervisor, Dr. Robert Wolkow, or Bob, for not only the opportunity to work with him and his group, but more importantly the framework upon which this work rests, that atomisitic intuition and propulsive joy in discovery imparted in the many, many discussions and suggestions and stories and jokes. And thank you for saying I should try putting DBs in a line.

CONTENTS

LIST OF FIGURES

1

AN INTRODUCTION

Scanning tunnelling microscopy, or STM, was the second experimental technique developed capable of spatially resolving atomic features. It is the premier tool for the characterization and manipulation of matter on the atomic scale since its first demonstration by Binnig and Rohr in 1982 [5]. Since then, a veritable explosion of work has been done in the field, yielding such famous results as the surface reconstruction of Si(111) [6], the fabrication of quantum corrals [7], and measuring the highest occupied and lowest unoccupied molecular orbitals (HOMO, LUMO) of pentacene molecules [8].

A property of STM is that the derivative of the tunnelling current with respect to voltage is proportional to the density of states (DOS) at that voltage. This means that the electronic structure of any atomic surface feature is directly measurable [9, 10]. Through $\mathrm{d}I/\mathrm{d}V$ mapping we recover the local density of states (LDOS), finding where and at what energy electronic state density exists [8].

Of interest in relation to this work are those systems where linear arrangements of atomic features are patterned and characterized, most often revealing bonding and antibonding interactions between two single features, and 1 D electron quantization for many arranged in a line. As will be discussed more in detail in Chapter 5, most often we see metal adatoms moved about on a certain surface to form the linear structures, be it Au on NiAl(100) [11], Cu on Cu(111) [12], or Ag on NiAl [13]. There are also examples involving vacancies, be they Cl atoms missing from an NaCl surface [14] or porphyrin molecules missing from a layer of them upon an Ag(111) surface [15].

Our experimental system is the hydrogen terminated Si(100)-2x1 surface. The atomic features we pattern and study are dangling bonds (DBs), formed when single hydrogen atoms are removed from the surface. DBs are essentially unsatisfied valency states of the underlying silicon atom, and exhibit three charge states: positive, neutral, and negative, all of which exist within the bandgap of silicon [3, 16, 17].

This means that DBs are atomic size quantum dots, capable of localizing discrete charge on the surface.

The tunnel-coupling and charge-sharing that occurs between DBs [18, 19] holds promise for their employment as the functional elements in a computational model built around electrostatically interacting quantum dots, the most famous theoretical architecture being that of quantum-dot cellular automata, or QCA [20, 21]. Furthermore, two tunnel coupled DBs could act as a single qubit, the information stored in their collective charge state [22].

We set out in this work to explore the electronic structure of close-spaced linear ensembles of DBs, which we call DB Chains. The spacing between DBs in these structures is 3.84 Å, so we expect great interaction between constituent DBs. These have been patterned and characterized before [23, 24], but comprehensive filled state dI/dV mapping has never been done. Questions regarding the constituent DB occupation, the degree of coupling, and the possible presence of 1 D electron quantization have yet to be answered.

Meeting these questions, and exploring our ability to affect change on the electronic structure of DB chains through electrostatic perturbation, will prove invaluable to both our scientific mandate and our attempts to fabricate and utilize atomic scale structures in computational capacities.

2

STM THEORY

2.1 MULTI-ELECTRON TUNNELLING

The basic features of multi-electron tunnelling between two reservoirs can be understood using a time-dependent perturbation approach first used by John Bardeen to describe "the tunnelling current flowing between two metals separated by a thin oxide layer" [25]. It was later extended by Tersoff and Hamann to describe the scanning tunnelling microscope [9]. More readily accessible tutorials of this treatment can be found easily [10].

2.1.1 *Time Dependent Perturbations*

The first assumption is that electron-electron interactions can be ignored. This allows us to use the single-particle Hamiltonian with the Schrödinger equation to describe each electron independently, writing

$$i\hbar\frac{\delta}{\delta t}\Psi(\mathbf{r},t) = \mathcal{H}\Psi(\mathbf{r},t) = -\frac{\hbar^2}{2m}\nabla^2\Psi(\mathbf{r},t) + V(\mathbf{r})\Psi(\mathbf{r},t) \tag{1}$$

We split the Hamiltonian into separate sample and tip Hamiltonians, $\mathcal{H}_S$ and $\mathcal{H}_T$, with respective potentials $V_S(\mathbf{r})$ and $V_T(\mathbf{r})$, and stationary states $\psi_i^S(\mathbf{r})$ and $\psi_n^T(\mathbf{r})$. The tunnelling is considered as a transfer of electrons from stationary states in the sample to those of the tip (or vice versa) under a perturbation induced by bringing the two reservoirs close together. Our goal is to find an expression which describes the transfer rate between the two, from which we can derive the tunnelling current.

The time-dependent evolution of an electron in a sample stationary state is given by $\Psi(\mathbf{r},t) = \exp(-itE_i^S/\hbar)\psi_i^S(\mathbf{r})$, where E_i^S is the energy of the stationary state. In an attempt to model the small probability of

transitioning into a tip state, or tunnelling, we introduce a sum over tip stationary states, so

$$\Psi(\mathbf{r},t) = e^{-itE_i^S/\hbar}\psi_i^S(\mathbf{r}) + \sum_n a_n(t)\psi_n^T(\mathbf{r}) \tag{2}$$

Because the electron starts in a sample stationary state, the time dependent coefficients $a_n(t)$ satisfy $a_n(0) = 0$. The probability of a transition to a certain state, in our case the tip state ψ_n^T, is given by $|\langle\psi_n^T(\mathbf{r})|\Psi(\mathbf{r},t)\rangle|^2$. The inner product is evaluated with our expression for $\Psi(\mathbf{r},t)$ to see how it relates to the coefficients $a_n(t)$, revealing

$$\left\langle \psi_n^T(\mathbf{r}) \middle| \Psi(\mathbf{r},t) \right\rangle = e^{-itE_i^S/\hbar} \left\langle \psi_n^T \middle| \psi_i^S \right\rangle + a_n(t) \tag{3}$$

Here we make another large assumption: that tip and sample states are nearly orthogonal, justified by the requirement that we have weak tunnelling. This means that we can neglect the inner product on the right hand side of Equation 3. The conclusion is that the transition probability is simply given by

$$\left| \left\langle \psi_n^T(\mathbf{r}) \middle| \Psi(\mathbf{r},t) \right\rangle \right|^2 \approx |a_n(t)|^2 \tag{4}$$

Knowing this transition probability, $|a_n(t)|^2$, it will be relatively simple to find the transition rate, and finally the tunnelling current once the appropriate states have been summed over. To that end we take Equation 2 and plug it into the Schrödinger equation, further substituting $\mathcal{H} = \mathcal{H}_S + (\mathcal{H} - \mathcal{H}_S)$ and $\mathcal{H} = \mathcal{H}_T + (\mathcal{H} - \mathcal{H}_T)$ to find that

$$\begin{aligned} i\hbar\frac{\delta}{\delta t}\Psi &= e^{-i\hbar E_i^S/\hbar}[\mathcal{H}_S + (\mathcal{H} - \mathcal{H}_S)]\psi_i^S \\ &\qquad + \sum_n a_n(t)[\mathcal{H}_T + (\mathcal{H} - \mathcal{H}_T)]\psi_n^T \\ &= E_i^S e^{-i\hbar E_i^S/\hbar}\psi_i^S + e^{-i\hbar E_i^S/\hbar}(\mathcal{H} - \mathcal{H}_S)\psi_i^S \\ &\qquad + \sum_n a_n(t)[E_n^T\psi_n^T + (\mathcal{H} - \mathcal{H}_T)\psi_n^T] \end{aligned}$$

We then take the time derivative of Equation 2 and multiply it by $i\hbar$. These two expressions are combined and the inner product is taken with tip stationary states ψ_j^T, resulting in

$$i\hbar\frac{\delta}{\delta t}a_j(t) = e^{-itE_i^S/\hbar}\left\langle \psi_j^T \right| \mathcal{H} - \mathcal{H}_S \left|\psi_i^S\right\rangle + E_j^T a_j(t) + \sum_n a_n(t)\left\langle \psi_j^T \right| \mathcal{H} - \mathcal{H}_T \left|\psi_n^T\right\rangle$$

Remembering that $a_n(0) = 0$ and knowing that the tunnelling is weak it is reasonable to assume that at small times, $a_n(t)$ is also small. So, as a first order approximation, we neglect all terms included in the sum over n in the previous expression to find a differential equation for the coefficients $a_j(t)$. The closed form solution, knowing the initial conditions $a_j(0) = 0$, is given by

$$a_j(t) = \frac{e^{-itE_i^S/\hbar} - e^{-itE_j^T/\hbar}}{E_i^S - E_j^T}\left\langle \psi_j^T \right| \mathcal{H} - \mathcal{H}_\mathcal{S} \left|\psi_i^S\right\rangle \tag{5}$$

The transition probability is then, substituting n for j,

$$|a_n(t)|^2 = \frac{4sin^2(t(E_n^T - E_i^S)/2\hbar)}{(E_n^T - E_i^S)^2}\left|\left\langle \psi_n^T \right| \mathcal{H} - \mathcal{H}_S \left|\psi_i^S\right\rangle\right|^2 \tag{6}$$

2.1.2 *Fermi's Golden Rule*

We sum over all tip states and take a derivative with respect to time to find the transition rate from a sample state to any tip state,

$$\frac{d}{dt}\sum_n |a_n(t)|^2 = 4\frac{d}{dt}\sum_n P_t(E_n^T - E_i^S)|M_{in}|^2 \tag{7}$$

Where $P_t(E) = sin^2(tE/2\hbar)/E^2$ and $\mathcal{M}_{in} = \langle\psi_n^T|\mathcal{H} - \mathcal{H}_S|\psi_i^S\rangle$. $\mathcal{M}_{in}$ is known as the matrix element; it encapsulates the distance dependence of the tunnelling current, as will be discussed later.

Upon examination, $P_t(E) \approx 0$ except for $E \in (-2h/t, 2h/t)$. For a large enough time, this energy window is small enough that the tip density of states, $D_T(E)$, is constant over all energy within the

window. Similarly the matrix element $\mathcal{M}_{in}$, which is dependent on energy through the stationary state ψ_n^T, is constant as well.

We can therefore replace the sum over tip states with an integral over tip density of states (DOS) for energies within this domain. Integrating $P_t(E)$ over all energy yields the value $\pi t/2\hbar$, allowing us to write

$$\begin{aligned}\frac{d}{dt}\sum_n |a_n(t)|^2 &= 4\frac{d}{dt}\int_{E_i^S-2h/t}^{E_i^S+2h/t} D_T(E)P_t(E-E_i^S)|\mathcal{M}_{in}|^2 dE \\ &\approx 4\frac{d}{dt}D_T(E_i^S)|\mathcal{M}_{in}|^2\int_{-2h/t}^{+2h/t} P_t(E)dE \\ &\approx 4\frac{d}{dt}D_T(E_i^S)|\mathcal{M}_{in}|^2\frac{\pi t}{2\hbar}\end{aligned}$$

And so the transition rate from a sample state ψ_i^S to any tip state takes on the form of Fermi's golden rule,

$$\Gamma_i = \frac{2\pi}{\hbar}|\mathcal{M}_{in}|^2 D_T(E_i^S) \tag{8}$$

We note that it also represents the reverse rate for transitions from any tip state to the sample state ψ_i^S, because of the symmetry of the arguments involved. This transition rate is for a single electron. Tunnelling is a multi-electron process; therefore, to find the tunnelling current, we must sum over all sample states that contribute. In doing so we must take into account electron occupation.

Electrons are fermions and thus obey the Pauli exclusion principle: only one electron can exist in one state at a time. The occupation probability of a fermionic state is given by the Fermi-Dirac distribution, written as

$$f(E_i,\mu) = \frac{1}{e^{(E_i-\mu)/k_BT}+1} \tag{9}$$

Where E_i is the energy of the state, μ is the total chemical potential, k_B is the Boltzmann constant, and T is the temperature in Kelvin. In our system, the applied sample bias V induces a difference between the chemical potential of the sample and tip, so $\mu_T - \mu_S = eV$.

Because they are fermions, electrons can only tunnel from filled states to empty states, with the occupation modulated by correctly chosen Fermi-Dirac functions. In sample to tip tunnelling at an energy E_i^S, the probability of the sample state being filled is $f(E_i^S, \mu_S)$, and the probability of the tip state being empty is $1 - f(E_i^S, \mu_T)$.

In the limit of zero temperature, the Fermi-Dirac distribution becomes a step function where the step occurs at the chemical potential. Below this energy all states are filled and above it all states are empty. This particular energy is known as the Fermi energy E_F.

2.1.3 *The Tunnelling Current*

Now we write an expression for the tunnelling current from sample to tip by summing over all sample states and multiplying the resulting transition rate by the charge carried by a single transition, the elementary charge, revealing

$$I_{S\to T} = \frac{2\pi e}{\hbar} \sum_i f(E_i^S, \mu_S)\big(1 - f(E_i^S, \mu_T)\big)|\mathcal{M}_{in}|^2 D_T(E_i^S) \tag{10}$$

By swapping μ_S and μ_T in Equation 10, one obtains the tip to sample tunnelling current, $I_{T\to S}$. The total current is the difference between the two, $I = I_{T\to S} - I_{S\to T}$. By convention the tunnelling from tip to sample is considered a positive current, which is the case for a positive sample bias. The full expression is

$$I = \frac{2\pi e}{\hbar} \sum_i \Big[f(E_i^S, \mu_T)\big(1 - f(E_i^S, \mu_S)\big) - f(E_i^S, \mu_S)\big(1 - f(E_i^S, \mu_T)\big) \Big] |\mathcal{M}_{in}|^2 D_T(E_i^S) \tag{11}$$

The Fermi temperature for metals is about two orders of magnitude above room temperature. Considering that STM experiments are usually performed at room temperature and below, we take the limit of zero temperature and approximate the Fermi functions as step functions.

We also substitute the sum over sample states for an integral over the sample density of states, $D_S(E)$. The step functions reduce the

integral over all energy to an integral between tip and sample Fermi levels, the difference of which is eV. We arrive at an elegant expression for the tunnelling current,

$$I = \frac{2\pi e}{\hbar} \int_{E_F^S}^{E_F^S + eV} |\mathcal{M}_{in}|^2 D_T(E) D_S(E) dE \tag{12}$$

The tunnelling current is essentially an integral over a window of tip and sample electronic structure multiplied by a term that describes the link between the two.

The polarity of the sample bias determines whether current flows into, or out of, the sample. Examining Equation 12, we see that if the sample bias is positive, we are tunnelling from the tip into states above the sample Fermi level. And if the sample bias is negative, we are tunnelling from states below the sample Fermi level into the tip.

The distinction here is made between imaging empty states or filled states of the sample, for a positive and negative bias respectively. Band diagrams of these imaging modalities are shown in Figure 2.1.

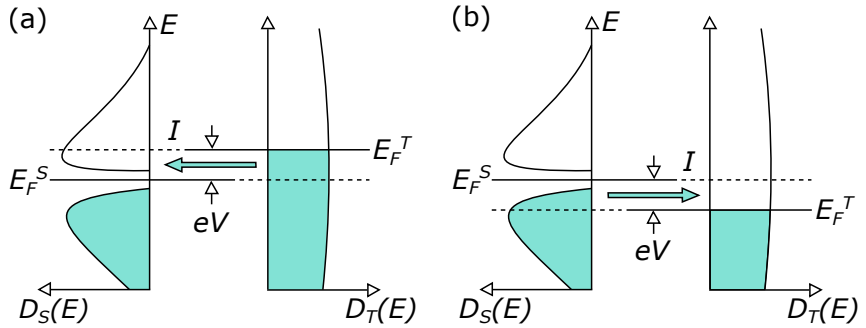

Figure 2.1: (a) Band diagram of empty state imaging. (b) Band diagram of filled state imaging. In each band diagram the sample DOS is on the left and the tip DOS is on the right.

2.2 THE MATRIX ELEMENT

Up until this point we have not paid much thought to the matrix element, $\mathcal{M}_{in} = \langle \psi_n^T | \mathcal{H} - \mathcal{H}_S | \psi_i^S \rangle$, which describes how tip and sample states are coupled. It is responsible for the distance dependence of the current and the resolution of the STM.

A matrix element can be defined in terms of any initial state and any final state, regardless of the individual energies of the separate states. However, in our derivation of Fermi's golden rule, we found that the sample and tip states that had any significant probability of transitions occurring between them were those of the same energy. In the following it is assumed that the matrix element is evaluated with sample and tip states of the same energy.

Bardeen showed that the volume integral could be approximated by a surface flux integral in the region between the two reservoirs [25],

$$\mathcal{M}_{in} \approx -\frac{\hbar^2}{2m} \int \left[\overline{\psi_i^S} \nabla \psi_n^T - \psi_n^T \nabla \overline{\psi_i^S} \right] \cdot d\mathbf{n} \tag{13}$$

Tersoff and Hamann took this result and evaluated it with approximate tip and sample wavefunctions with exponential decay within the junction. The tip was modelled as having a hemispherical apex, so the tip wavefunctions were made to be radially symmetric about a point within the apex of the tip [9].

They found the current has an exponential dependence on the tip-sample separation and concluded that the sample state density that exists on the central tip axis is responsible for passing the bulk of the tunnelling current. Because of the sharpness of the tip, the current is localized to atomic scale features.

We will reach a similar conclusion by using the one dimensional Schrödinger equation.

2.2.1 *A One Dimensional Model*

The potential of the tunnelling junction, $V(z)$, is modelled as a simple rectangular barrier of height Φ from $z = 0$ to $z = d$, where d is the tip-sample separation and $\Phi = (\Phi_S + \Phi_T)/2$ is the average of the work functions of the sample and tip. Zero energy is taken as the Fermi level. We split this potential into tip and sample potentials:

$$V_S(z) = \begin{cases} 0 & z \leq 0 \\ \Phi & 0 < z \end{cases} \qquad V_T(z) = \begin{cases} \Phi & z < d \\ 0 & d \leq z \end{cases} \tag{14}$$

The stationary states, $\Psi_i^S(z)$ and $\Psi_n^T(z)$, take on oscillatory exponential forms in the $V = 0$ regions and exponentially decaying forms in the $V = \Phi$ regions of their respective potentials, written as

$$\Psi_i^S(z) = \begin{cases} Ae^{ikz} + Be^{-ikz} & z \leq 0 \\ Ce^{-\beta z} & 0 < z \end{cases}$$
$$\Psi_n^T(z) = \begin{cases} De^{-\beta(d-z)} & z < d \\ Fe^{ikz} + Ge^{-ikz} & d \leq z \end{cases} \tag{15}$$

Where $k = \sqrt{2mE/\hbar^2}$, and $\beta = \sqrt{2m(\Phi - E)/\hbar^2}$. A to C and D to G are sets of constants that can be solved in terms of one another by matching boundary conditions.

It is easy to evaluate the matrix element for tip and sample states of energy E. We find that its modulus squared, and thus the tunnelling current through Equation 12, is exponentially dependent on tip-sample separation, as in the statement

$$|\mathcal{M}_{in}|^2 \propto e^{-2\beta d} \tag{16}$$

This exponential dependence is responsible for the incredible resolution of an STM. If the tip has a single atom that is 1.5 Å closer to the surface than all other atoms, its matrix element is 130 times greater, so about 99% of the tunnelling current will flow through it. We can thus measure a signal channelled through atomic scale features.

2.3 THE DENSITY OF STATES

The differential conductance, $\mathrm{d}I/\mathrm{d}V$, is relatively easy to derive from Equation 12 as

$$\frac{\mathrm{d}I}{\mathrm{d}V} = \frac{2\pi e^2}{\hbar}|\mathcal{M}_{in}|^2 D_T(eV + E_F^S) D_S(eV + E_F^S) \tag{17}$$

The decay constant $\beta = \sqrt{2m(\Phi - eV)/\hbar^2}$ encapsulates the energy dependence of the matrix element. Because eV is usually small compared to Φ, we claim that $|\mathcal{M}_{in}|^2$ is nearly constant over the voltage range that we consider.

Being a metal, the density of states of the tip is nearly constant over this voltage range as well; we therefore conclude that the differential conductance is proportional to the sample density of states near the Fermi level, expressed as

$$\frac{\mathrm{d}I}{\mathrm{d}V} \propto D_S(eV + E_F^S) \tag{18}$$

This density of states has heretofore been rather vague in its definition. It includes all states available for tunnelling by the tip.

From our discussion of the matrix element, we found that the wavefunction overlap that enables tunnelling occurs at the very apex of the tip—a consequence of the exponential decay of tip and sample states. So we reason that the surface states in a small volume near the apex of the tip are the main contributor to the measured density of states.

However, the STM must form a complete circuit, so current must flow through bulk states; therefore the measured density of states will reflect some convolution with bulk states. We note that the bulk states need not be perfectly aligned in energy with the surface states to enable current. For example, electrons within the bulk can emit phonons and gain access to conducting states that are lower in energy.

Still, by measuring the density of states at different positions on the surface, we are able to map out the surface local density of states (LDOS) at different energies, as the bulk contribution changes little over the spatial scale of our map.

3

INSTRUMENT & PREPARATION TECHNIQUES

All results in this thesis were obtained using an Omicron low temperature STM, mounted within an ultra high vacuum system, shown in Figure 3.1. As the second Omicron low temperature STM in our group, the entire system is named the LT2.

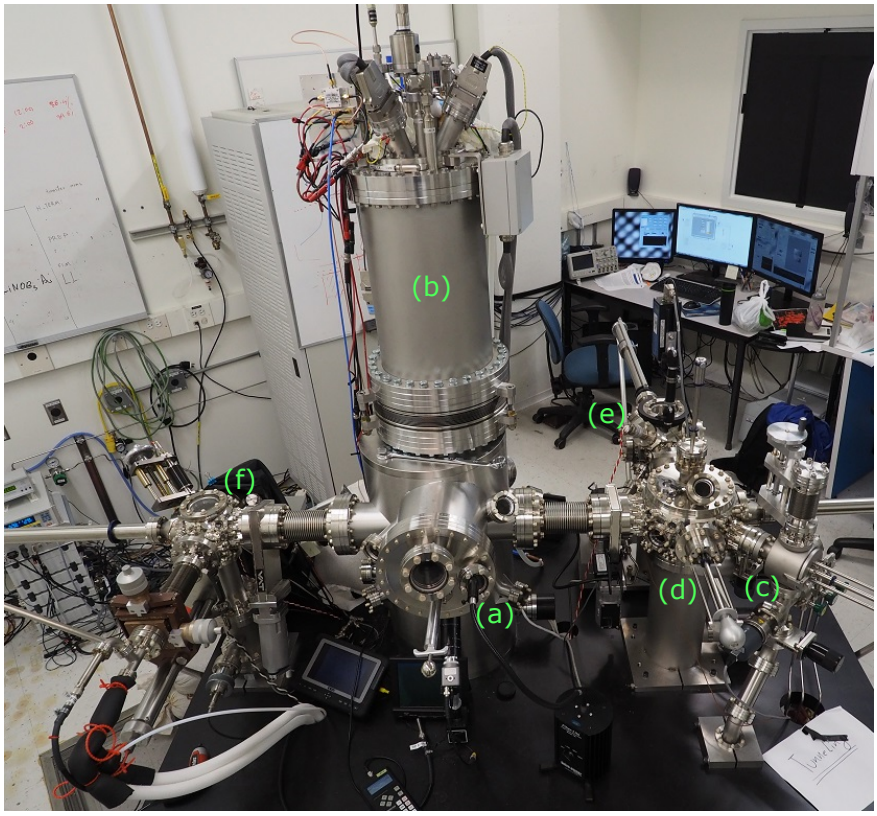

Figure 3.1: LT2 system, including the (a) STM chamber, (b) cryostat, (c) loadlock chamber, (d) transfer chamber, (e) sample preparation chamber, and (f) tip preparation chamber.

3.1 ULTRA HIGH VACUUM

To study surfaces at the atomic scale, we require them to be clean. Unfortunately, the atmosphere that we live in ensures that surfaces exposed to it do not stay clean for very long. The solution is to do

experiments at a low enough pressure that surfaces do not become contaminated for the duration of the experiment.

The monolayer formation time is defined as the average time it takes for a monolayer of adsorbed gas particles to form on a surface at a certain pressure, assuming all particles that hit the surface are adsorbed. At $2x10^{-6}$ Torr, a monolayer is formed in 1s. At $2.6x10^{-11}$ Torr, a monolayer is formed in a day. This is about the pressure necessary for our multiple hour STM experiments, between $1x10^{-10}$ and $1x10^{-11}$ Torr, firmly within the regime considered ultrahigh vacuum (UHV), which is between $1x10^{-9}$ and $1x10^{-12}$ Torr [26].

3.1.1 *Vacuum Pumps*

To achieve UHV pressures, we employ various pumps routinely [26]. Roughing pumps are the first to be switched on, taking a chamber at atmospheric pressure, 760 Torr, down to pressures near $1x10^{-3}$ Torr where a high vacuum pump can begin to operate.

Turbomolecular pumps, or turbo pumps, are used when we require fast pumping to UHV. On the LT2, turbo pumps are used in the load-lock, the FIM chamber, and the gas lines that supply any leak valves on the system. A column of moving rotors (alternating with stationary rotors, stators) spinning at near the molecular gas velocity impart momentum to any colliding gas particle, batting it from the inlet toward the outlet.

Sputter-ion pumps, or ion pumps, are the high vacuum pumps that we use on all other chambers in the LT2. They operate with no moving parts—so do not produce mechanical noise that would disturb an STM experiment. A swirling electron cloud ionizes gas molecules that accelerate in an electric field and impact the titanium cathode, sputtering titanium onto many surfaces within the pump. Pumping of gas occurs due to chemisorption on titanium surfaces, burial of gases under layers of sputtered titanium, and diffusion into the cathode lattice after ion implantation.

Titanium sublimation pumps (TSP) also use titanium as a gettering pump, spraying sublimated titanium over the chamber walls that pump for hours after filament heating ceases.

In cryopumping, elements of the pump are taken to very low temperatures, often down to 4 K or further. Any gas molecules that hit the cold element are physisorbed to the surface. The cryostat which keeps the STM at 4.5 K cryopumps significantly.

3.1.2 *Baking*

When a chamber is evacuated, layers of adsorbates (mostly water) degas slowly, preventing UHV from being reached. To remove them, the chamber is heated to 150 °C for a number of days. Adsorbates evaporate off the walls and are pumped away, rendering UHV possible when the machine is cooled to room temperature [26].

We do not wish to bake every time we change tips or samples, so we use a loadlock routinely exposed to atmosphere that can quickly obtain an intermediate pressure of about $1x10^{-7}$ Torr. This pressure corresponds to a monolayer formation time of 22 s, which will not ruin a baked UHV surface exposed to it for the few minutes necessary to transfer between the two chambers.

3.2 STM CHAMBER

The STM chamber, the heart of the vacuum system, is engineered to vibrationally isolate the experiment and maintain a temperature of 4.5 K [27].

3.2.1 *Thermal Regulation*

Many challenges exist in room temperature STM experiments. Thermal drift causes the sample and tip to move in relation to one another at random. Of more fundamental import, at room temperature the average thermal energy is $k_B T = 25.7$ meV; one cannot study physical systems of lower per-particle energy here. So we perform our experiments at 4.5 K, where the thermal energy is $k_B T = 0.389$ meV, and thermal drift is dramatically decreased.

The centre of the STM, which contains the tip and sample, is completely enclosed by two cryoshields in thermal contact with their respective cryostats, the inner at 4.5 K cooled by liquid helium and the

outer at 77 K cooled by liquid nitrogen. The cryopumping performed keeps the pressures within the cryoshields far below pressures measured by the ion gauge outside, allowing samples to stay clean for weeks at a time.

The liquid helium cryostat, from a full 3 L, empties in about 2 days. A typical fill, necessitating the cooling of transfer lines, consumes about 9 L of liquid helium. A helium recovery system, shared by the different low temperature STMs within the group, takes cryostat boiloff and liquefies it for reuse as a cryogen at a rate of 22 L/day.

3.2.2 *Vibration Isolation*

When tunnelling, the tip is less than 1 nm from the surface. As discussed before, the tunnelling current is exponentially dependent on the tip-sample separation. Any external vibrations coupled between the tip and sample will cause unwanted noise in our tunnelling current signal, and in a worst-case scenario, crash our tip into the sample, effectively ending the experiment.

It is therefore necessary to isolate the STM from any possible vibrations, be they footsteps next to the machine or landscaping done outside the building. This is achieved through air legs which support the entire vacuum chamber and a spring stage with eddy current damping that bears the sample and tip.

3.3 FABRICATING SHARP TIPS

Most experiments were performed with tungsten (W) tips. Polycrystalline W wire is sharpened through an electrochemical etching process [28] followed by cleaning and further sharpening using a field ion microscope (FIM) within the tip preparation chamber.

3.3.1 *Electrochemical Etch*

The wire is dipped 3 to 5 mm into a 2 M solution of NaOH and a DC bias is applied. W atoms are oxidized by OH^- and form WO_4^{2-}, which is heavy in the solution and migrates downward, causing etch-

ing to occur primarily near the meniscus where there is the highest concentration of OH^-.

Eventually, the thinnest part of the wire is unable to support the remainder beneath the solution and breaks, leaving behind a tip apex of less than 20 nm radius. The current flowing through the wire and solution suddenly lowers greatly, which is detected by a circuit that shuts off the etching voltage in less than a microsecond, before the sharp tip can be blunted by further electrochemical reaction.

3.3.2 *Field Ion Microscopy*

Once inside the tip preparation chamber, the tip is heated to 900 °C for a minute to clean off any contaminants, mainly water and other weakly bound adsorbates, then put into the FIM.

A positive voltage on the order of kilovolts is put on the tip. An imaging gas, helium (He), is introduced at a pressure of $1x10^{-5}$ Torr. By field polarization and subsequent acceleration, its particles impact the tip and thermalize through a series of 'bounces' along the shank, migrating on the surface to the apex by the attractive field.

The field is made strong enough to ionize any gas particle in the vicinity of the apex. The newly formed ion is accelerated away from the apex toward a screen, where it impacts and is detected. The corrugation of the field reflects the atomic structure of the apex—gas particles are more likely ionize over apex atoms than between them. As a multitude of atoms are ionized, an atomically resolved image of the apex appears [29].

Any lightly bound adsorbates on the tip are easily removed by the field. If more strongly bound, the voltage is increased such that the field removes apex atoms in a process called field evaporation. We are able to ensure a clean apex [29].

FIM can be used to sharpen tips as well [30, 31]. Another gas with a lower ionization field that is known to be corrosive to the tip material in field conditions is introduced at a partial pressure of $1x10^{-6}$ Torr. We use molecular nitrogen (N_2). This etching gas reacts with tip material, forming small protrusions that are removed by the field—taking away some tip material. Any etching gas particles that come near the apex

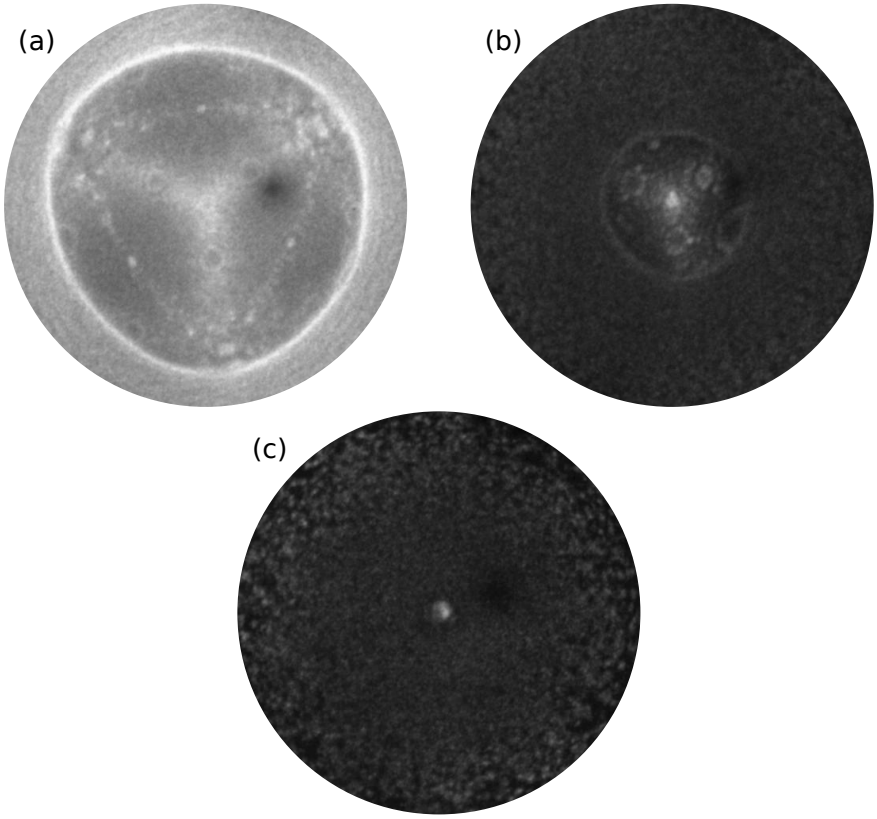

Figure 3.2: A series of FIM images showing the etching of a W single atom tip. (a) An atomically resolved He image of a large diameter tip apex with a bright N_2 etching gas ring surrounding it farther down the tip. (b) A He image of a small diameter tip apex image; the bright ring is still visible but is darker because the N_2 partial pressure is lower. (c) A He image of a single atom tip.

are ionized in the regular fashion, accelerated away before they can react with the tip.

Thus the etching only occurs in a ring below the apex—where the field is high enough to cause corrosion but low enough that etching gas can reach the surface and react. The tip becomes sharper. By carefully lowering the voltage, a tip can be fabricated such that the ion beam is only produced at a single atom. We call this a single atom tip; it is ideal for STM experiments.

3.4 PREPARING HYDROGEN TERMINATED SILICON

We use highly n doped silicon (Si) wafers of orientation (100), with a nominal room temperature resistivity of 0.003 to 0.004 Ω·cm. Cleaved strips are mounted in an Omicron sample holder and placed in the sample prep chamber. A current through the crystal is applied to heat it to 600 °C for multiple hours to degas.

In a process called flashing, the crystal is brought to either 1050 or 1250 °C for less than a second three to four times to remove the oxide and vaporize any remaining adsorbates [32]. The exact flashing temperature determines the number of near surface dopants that exist in the sample. At the higher temperature, dopants about 150 nm close to the surface diffuse and evaporate from the surface, leaving this region absent of dopants [33].

Molecular hydrogen (H_2) is introduced at a pressure of $1x10^{-6}$ Torr while a filament of tungsten wire in the chamber is heated to 1700 °C. H_2 molecules that hit the filament crack into two H atoms. The sample, at room temperature, is bombarded by molecular hydrogen for two minutes, etching and cleaning the surface slightly. With H still present, the sample is flashed a last time and immediately brought to 330 °C and kept there for 20 s. At this temperature, the surface reconstructs to the 2x1 form, with each surface silicon atom capped by one H atom [34, 35]. The H-Si(100)-2x1 surface is formed.

3.5 OPERATING THE STM

The basic geometry of our STM is shown in Figure 3.3. A tip is placed on the end of a tube piezo scanner, which is fixed to x,y, and z piezo slipstick motors. The sample is mounted on a stationary platform with the plane orthogonal to the axis of the tip. A more negative z piezo displacement is considered closer to the sample [27].

Piezos allow for extremely fine movement; we routinely control movement in single picometer increments. These materials will deform predictably under application of an electric field and we exploit this in the STM to move our scanner in an atomically precise manner. We call these the fine piezos.

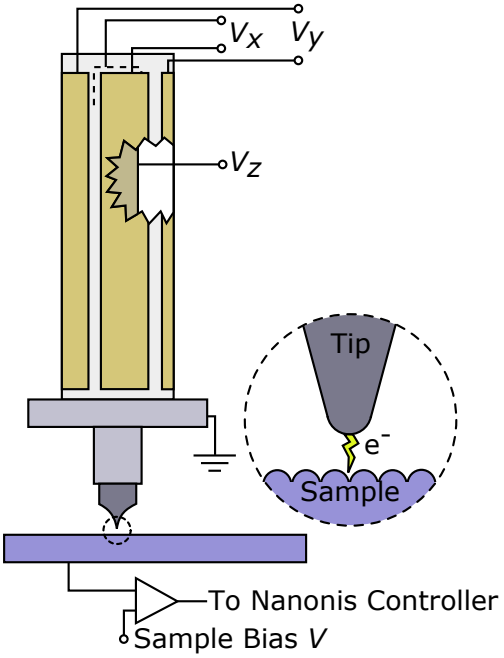

Figure 3.3: Diagram of an STM. The tube scanner bends under application of V_x and V_y on either side of the scanner, and stretches under application of V_z on an electrode within the tube whose counter electrode is those of x and y. The current to voltage pre-amplifier connected to the sample is floated to the sample bias V.

A feedback loop is defined such that the z piezo voltage, or tip height, is controlled to keep the tunnelling current at a chosen value.

The piezo slipstick motors, or coarse motors, work by moving a piezo bearing a mass slowly in one direction, then moving it back very quickly. The mass, because of its inertia, slips during the fast movement, displacing it slightly. Repetitions of this cycle allow fast multi-mm scale movement with nm scale control

The software and electronic hardware package that controls the STM is manufactured by Nanonis. A tool package allows us to write LabVIEW programs which interface with the Nanonis software and control the STM. Thus we are able to create custom experiments and automate many tasks.

3.5.1 *Approaching the Sample*

The piezos on the tube scanner have only a movement range of about 400 nm at 4.5 K under our high voltage amplifier setup, so the coarse motors are necessary to move the tip within scanning range of the surface.

Once the tip is brought as close to the sample as the operator can judge by eye, the auto-approach algorithm is utilized to reach tunnelling distance within the range of the piezos without crashing the tip. The fine z piezo is actuated to move the tip toward the sample with the feedback loop on in an attempt to reach the sample. If the fine z piezo reaches its maximum extension without the tip reaching the sample, it is withdrawn from the sample and 1–2 coarse motor steps are taken toward the sample. These steps repeat until the tip reaches the surface, i.e. tunnelling distance is within the z fine piezo range.

3.5.2 *Scanning*

The most common kind of STM imaging is known as constant current imaging. A voltage and current setpoint are chosen (specified for each image), and the tip is scanned over the surface. The feedback loop maintains a constant tunnelling current during the scan by adjusting the tip-sample distance, or tip height, for its duration. One obtains a topographical map of a constant electron density overlap; examples of filled and empty state images are shown in Figure 3.4.

Another form of imaging is called constant height imaging. Here, a voltage and tip height are chosen, the feedback loop is deactivated, and the tip is scanned over the surface; the changes in the tunnelling current are mapped.

The images produced with STM are atomic in their detail and offer a glimpse into a physical realm far removed from our Newtonian intuitions.

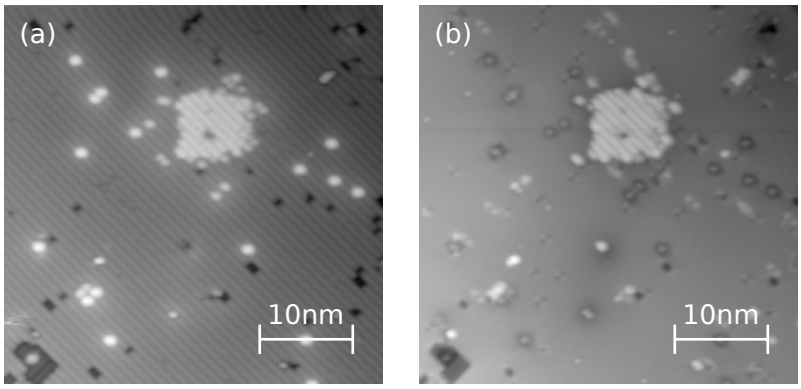

Figure 3.4: (a) Filled state STM image of an H-Si(100)-2x1 surface with feedback settings of −1.8 V, 50 pA. (b) Empty state image of the same surface region at 1.4 V, 50 pA. The dimer rows are evident as diagonal lines in (a). DBs appear as bright white spots in in (a) and as white spots within dark halos in (b). The square patch in both images is a region where all surface H atoms have been desorbed by moving the tip over it at 4 V, 150 pA.

3.5.3 *Tip Conditioning*

Often the tip is less than perfect, and we wish to improve its imaging capability without replacing it entirely. These kind of imperfections manifest as multi-tip imaging, where images have features that repeat spatially due to multiple sharp points on the tip contributing to the image. An example of a double-tip is shown in Figure 3.5.

Field emission up to 1 nA into the surface for 20 to 30 s acts to clean the tip and produces large, round, desorption regions. Alternatively, a small area can be scanned at relatively high voltages and currents, greater than 4 V and 100 pA. This forms desorption regions loosely bounded by the area scanned, as seen in Figure 3.4.

To induce small tip changes, we move the tip toward the surface a certain amount far closer than in regular tunnelling, even to the point of touching the surface lightly. The extreme conditions shift the atoms of the apex largely uncontrollably, with luck resulting in a sharper tip. The distance ranged from 600 pm for small changes to 1.2 nm for great changes. -2.0 to -3.0 V were applied during movement. This process, called tip shaping, seems to work better on large desorption patches. Modelling attempts, and tip imaging and shaping with field ion mi-

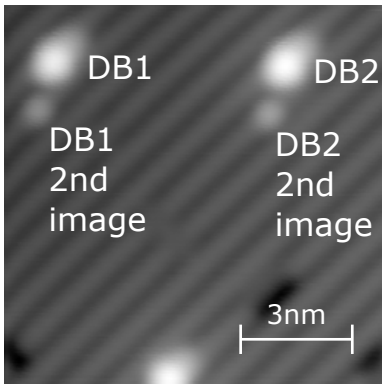

Figure 3.5: Double tip image of two DBs at −1.8 V, 50 pA. Both DB1 and DB2, as labelled, each exhibit secondary images caused by imaging with a secondary tip apex atom.

croscopy have not fully resolved the uncertainties of tip structure and changes thereof.

3.5.4 *Thermal Drift & Piezo Creep*

Temperature variations within the STM cause uncontrolled movement of sample with respect to tip. We call this thermal drift. It appears as motion of the tip over time without direct input—the region being scanned will move slightly, and the z position of the tip will appear to shift as the feedback loop compensates for the drift.

If a certain voltage is applied to a piezo, it will deflect a certain amount very quickly, and continue moving slightly in that same direction. This phenomenon is known as piezo creep, and is a consequence of very small shifts of the position of boundaries between polarized domains within the piezo material upon application of an electric field. It is evident as a logarithmic change in z position as a function of time, after a tip approach, as the feedback loop compensates for the piezo movement. It also appears as distorted STM images when the tip is moved a great distance across the surface, and as a small, sub-Å scale mismatch of features in forward and backward scans.

Experiments that involve deactivating the feedback loop, or locking the loop, are highly sensitive to drift and creep. These effects impose a certain time limit to locking the loop before the dataset is ruined or worse, the tip is crashed. Operating at 4.5 K causes the entire STM to be nearly isothermal, eliminating nearly all thermal drift and largely

preventing piezo creep, a thermally activated process. We alleviate the remaining creep by waiting about half an hour to perform experiments after a large tip move, be it from approaching the tip or moving to a new area of the sample. The mismatch of forward and backward scans can be eliminated by scanning at slow enough speeds, less than about 10 nm/s. Under these conditions we can image an area and then reliably move the tip to a point of interest within that area by a mouse click. Furthermore, the loop can remain locked for up to 20 to 30 minutes before the ill effects of drift and creep become visible. This contrasts with room temperature experiments, where these effects are relatively enormous and the loop can be safely locked for only fractions of a second.

3.6 SPECTROSCOPY

Current-voltage (*I*-*V*) spectroscopy, also known as scanning tunnelling spectroscopy (STS), allows us to directly measure the electronic structure of the sample. In a traditional STS experiment, the height is set by choosing a certain voltage and current for the feedback loop before deactivating it, thereby fixing the tip-sample separation. The voltage is then swept while the tunnelling current is collected and to an I-V curve.

To find $\mathrm{d}I/\mathrm{d}V$ as a function of voltage—a quantity proportional to the sample density of states as discussed in Section 2.3—we can numerically differentiate the I-V curve. This is often noisy, so we prefer to directly measure $\mathrm{d}I/\mathrm{d}V$ by employing a lock-in amplifier.

Obtaining trustworthy STS data is not trivial. One must choose a voltage range and tip height that are unlikely to destroy the tip, include enough points for the required resolution, and use a long enough integration time per point for acceptable noise levels. If the STS takes too long, drift and creep will affect the measurement.

We find that STS with a duration of a few minutes is sufficient to produce excellent datasets, far below the 20 to 30 minute limit imposed by drift and creep.

3.6.1 *Lock-in Amplifier*

A lock-in amplifier measures a signal at a very specific frequency, rejecting signals from all other frequencies. The input signal is multiplied by a reference signal and integrated over a long time. Due to the orthogonality of sinusoids, all signals that are not at the frequency of the reference do not contribute to the output, which is dependent only on the amplitude of the two signals and their relative phase.

In our experiments, we modulate the DC tip-sample bias voltage with a 30 mV peak to peak signal at about 800 Hz. The lock-in amplifier then isolates the component of the tunnelling current at that frequency. If we assume that $\mathrm{d}I/\mathrm{d}V$ is almost constant over the 30 mV range, then this component must be proportional to $\mathrm{d}I/\mathrm{d}V$ at the DC bias voltage. This modulation width limits the precision of our measurement, and acts to broaden and smear those features which change over smaller voltage increments.

3.6.2 *dI/dV Mapping*

As mentioned in Chapter 2, mapping $\mathrm{d}I/\mathrm{d}V$ spatially gives the local density of states over that region at a particular sample energy with respect to the Fermi level. Our measurements follow a certain algorithm, which has been automated in a number of LabVIEW programs.

1. The tip height, which remains a constant for the entire experiment, is set by choosing a particular sample bias and tunnelling current over a certain region, in our case an H-Si region. The feedback loop is given time to stabilize at these settings before being deactivated; a slight tip retraction is sometimes added here.

2. The bias voltage is changed to the level we currently wish to probe.

3. The tip is moved through a region of interest, either a plane or a line, that is parallel to the average surface plane while the lock-in amplifier collects the $\mathrm{d}I/\mathrm{d}V$ signal.

These three steps are repeated for all bias voltages of interest to form a full dataset. If the region is a plane or a line we refer to the datasets as a collection of $\mathrm{d}I/\mathrm{d}V$ maps or $\mathrm{d}I/\mathrm{d}V$ linescans respectively.

In the 3rd step, the tip must move fairly slowly to ensure a good signal. This is equivalent to increasing the integration time of an STS experiment—it increases the averaging time at each point and limits noise. For $\mathrm{d}I/\mathrm{d}V$ maps and linescans, the tip is moved at 1 and 0.4 nm/s, resulting in about 10 minutes and 10 s per scan respectively.

We reset the tip height after each scan because time spent with the feedback loop deactivated should be limited to avoid the effects of drift and creep. The maximum we use, 10 minutes, is well below those times where drift and creep become evident in our system.

The $\mathrm{d}I/\mathrm{d}V$ signal from the lock-in amplifier takes on arbitrary units, and is dependent on some calibration factors. This brings concerns about comparing different datasets with different specific calibrations. If data is collected with the same tip height and lock-in calibration, it can be directly compared; all other comparisons must only consider spatial variations in the $\mathrm{d}I/\mathrm{d}V$ maps.

4

HYDROGEN TERMINATED SILICON

In the clean silicon (100)-2x1 surface, each Si atom pairs with one other to form dimers with bonds parallel to the surface plane. Each atom then shares three Si-Si bonds and has one remaining valence electron, a dangling bond. Upon H-termination, the dangling bond is replaced by a covalent bond to one H atom, forming the H-Si(100)-2x1 surface shown in Figure 4.1.

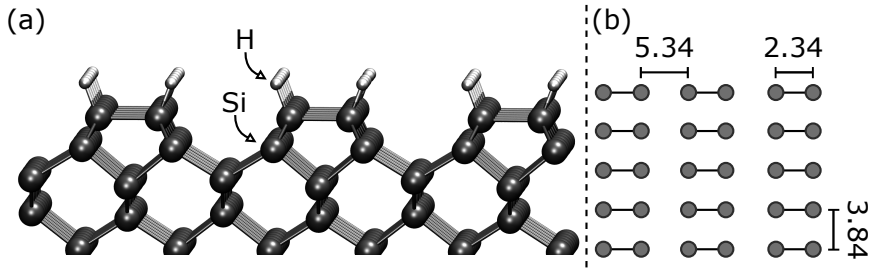

Figure 4.1: (a) 3 D ball and stick model of the H-Si(100)-2x1 surface from the side, showing the formation of dimer rows as pairs of Si atoms lean toward each other and bond covalently. (b) Diagram of the surface from a top-down view, with solid lines representing dimers and small grey circles representing surface H atoms. The relevant surface lattice constants shown are in units of Angstrom (Å)

In STM images the dimer rows are most visible in filled state imaging, and appear as lines going across the surface, as seen in Figure 3.4. At step edges, the direction of the lines rotates by 90 °, a consequence of the diamond structure of the bulk crystal.

4.1 SILICON BANDS

Silicon is a semiconductor; when free of dopants, the Fermi energy lies in the middle of a bandgap of width 1.14 eV. The lower and higher energy bands are called the valence and conduction bands (VB and CB) respectively.

The incorporation of dopants into the lattice with four covalent bonds is predicated on the dopant atom either accepting an electron from or donating one to a crystal band. Acceptors, or p type dopants, are usually from group III; donors, or n type dopants, are usually from group IV. Doping causes an excess of free carriers, those being electrons for n type and holes for p type.

At doping densities less than $10^{18}/\text{cm}^3$, thermal energy is needed for dopants to ionize, thereby creating excess free carriers. For higher, degenerate doping levels, the dopants are close enough that electrons can directly 'hop' between dopants, forming a band that remains conductive at low temperatures. At 4.5K, we require degenerately doped silicon to complete the tunnelling circuit—we used As doped n type silicon of doping density $10^{19}/\text{cm}^3$. We represent this doping level, which forms the donor band, by placing the Fermi level within the conduction band on the Fermi diagram.

Flashing samples to 1250 °C removes dopants in the 150 nm region from the surface. This contrasts with 1050 °C flashed samples, which retain dopants all the way to the surface. Their contrasting band diagrams are shown in Figure 4.2.

4.2 BAND BENDING

Semiconductors do not have the supply of free electrons necessary to keep their bulk at a constant potential when an electric field is applied close by. So, the tip field penetrates into the sample and near surface free carrier occupation changes to accommodate it. A significant amount of the applied voltage between tip and sample thus drops within the silicon bulk. On a band diagram it is represented as a spatial bending of the bands near the surface with a constant Fermi level. Surface states shift up or down the same amount the bulk bands do at the surface, borne by the band bending.

The effect on STM experiments is considerable. We do not probe the states of the sample at a certain bias voltage, but at a voltage minus some contribution from band bending. As the surface states are borne by band bending, tunnelling can occur between electrons in mid-gap surface states, such as DBs, and deeper bulk bands not affected by band bending.

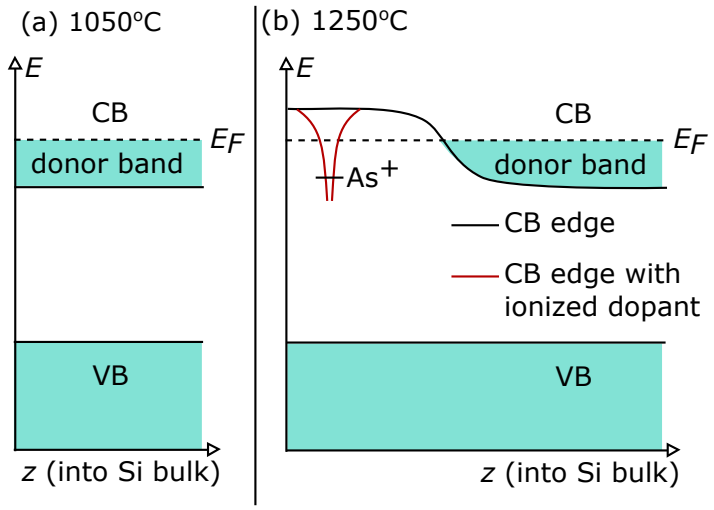

Figure 4.2: (a) Band diagram of a 1050 °C flashed sample, with the donor band that extends to the surface. (b) Band diagram of a 1250 °C flashed sample, with an absence of a donor band near the surface. The conduction band edge in the presence of an isolated ionized As dopant atom in the near surface region is shown. "CB" and "VB" refer to the conduction and valence bands respectively. The diagram is not to scale.

4.3 SPECTROSCOPY OF H-SI

Over H-Si, all surface states are passivated. STS here reveals only bulk states, the valence and conduction band evident as sharp onsets of current. The donor band is only seen in 1050 °C flashed samples, because dopants extend right to the surface. The width of the gap appears to be larger than the real value, further increasing for smaller tip-sample separation, as band bending stretches surface features to seemingly larger energies.

To further explore these well known STS results for W tips at varying height over H-Si, we performed similar experiments with an iridium (Ir) tip. We found that the I-V curves at each height to be very similar to those with W tips at about 200 pm larger tip-sample separation.

Ir has a larger work function than W, so the average work function defined in Chapter 2, $\Phi = (\Phi_T + \Phi_S)/2$, is greater for the Ir tip, leading to a greater decay constant β and a smaller matrix element

for a given tip height. So the Ir tip has to be 200 pm closer to the sample to get the same tunnelling current as the W tip.

4.4 DANGLING BONDS

4.4.1 *Charge States and Wavefunctions*

Dangling bonds (DBs) are unsatisfied valence orbitals found at the surface of hydrogen terminated semiconductor surfaces. They are mid-gap localized surface states capable of holding zero to two electrons, corresponding to a positive (+), neutral (0), and negative (–) charge state. Only the energies at which the DB charge state changes are experimentally accessible—we refer to them as the charge transition levels (+/0) and (0/–), where below and above the level the DB is in the charge state to the left and right of the slash respectively [3]. The charge transition levels of isolated DBs $E^{+/0}$ and $E^{0/-}$ have been calculated with density functional theory (DFT) for isolated DBs, yielding 0.35 eV and 0.85 eV above the valence band respectively [16, 17].

The DB wavefunction can be approximated by a slater type orbital with the symmetry of a p orbital. The decay rate of the wavefunction, hence its spatial extent, is a function of the electron ionization potential. Because the bulk and vacuum have greatly differing dielectric constants, this decay rate is much faster in vacuum than in the bulk. We find wavefunctions shown in Figure 4.3 for the neutral and negative DB [36].

The (+/0) and the (0/–) transition levels are not two separate orbitals, rather the same orbital with the ability to accept two electrons. When the DB is neutral the lone electron has an energy of $E^{+/0}$. The second electron added to the orbital, rendering the DB negative, has an energy of $E^{0/-}$—higher than the first because of the Coulomb repulsion acting on the second electron from the first. This implies that when the (+/0) level is empty, the (0/–) level does not exist [2].

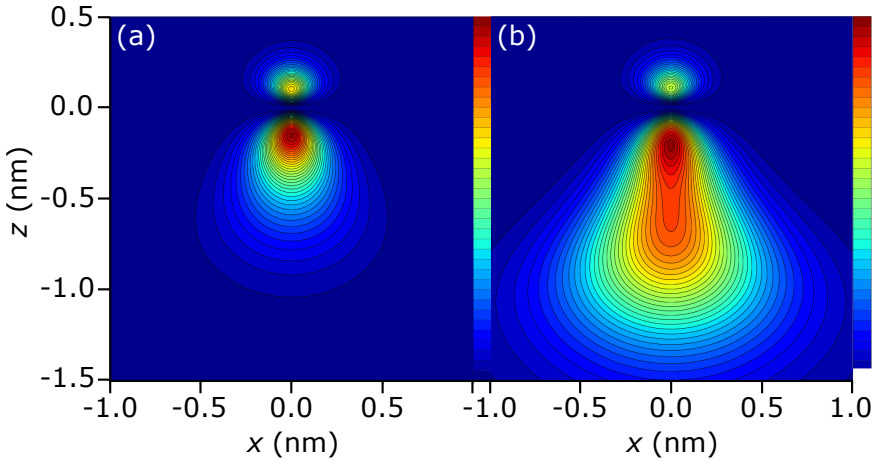

Figure 4.3: Isodensity plots of the neutral (a) and negative (b) DB wavefunctions, with the surface plane at $z = 0$ nm. The colour scale in (a) and (b) run from 0.00–1.08x10^{28} and 0.00–1.44x10^{27} respectively [3].

4.4.2 *Band Bending of DBs*

DBs, when localizing a positive or negative charge, bend bands nearby. A positive DB bends bands downward, lowering the energy of electrons in the region. A negative DB bends bands upward, increasing the energy of electrons in the region. DB band bending changes the tunnelling current at a specific tip height and voltage depending on the tip's lateral proximity to the DB. This effect is most clearly seen in empty state imaging where each DB appears as a small bump surrounded by a dark halo, further surrounded by a speckled region. Both areas are a result of the different DB charge states bending the bands and modulating the tunnelling current to different degrees [3, 36].

In the halo region, injection from the tip to the DB keeps the DB negative—bending the bands up and making the H-Si appear lower [36]. Within the speckled region all three states have a chance to exist, so the tunnelling current at a specific location and voltage can take on three distinct values. The resulting time trace contains three state "telegraph noise" which can be analyzed to determine transition rates between the states [3].

4.4.3 *DB Wavefunction overlap*

One could reasonably expect that when placed close enough together, the overlap of single wavefunctions is great enough to cause significant electron sharing between DBs, rendering the isolated wavefunction inadequate to describe each electron. A number of molecular orbitals will form, each describing a single state with density across two or more nuclei, in our case the DB centres.

Neglecting any buckling effects, a single bare dimer on the H-terminated Si(100) surface exhibits these effects. Here, the DBs are separated by only 2.34 Å and form π and π^* bonding and antibonding molecular orbitals visible in filled and empty state images respectively. In $\mathrm{d}I/\mathrm{d}V$ spectroscopy over a bare dimer, their state density manifests as two peaks within the gap, with an energy splitting so great that the states overlap somewhat with the valence and conduction bands [37, 38]. This overlap means that electrons can transition from those states to the bulk bands; the bare dimer is unable to support a localized charge.

4.4.4 *Filling and Emptying DB levels*

When probing filled states, DB levels are refilled by bulk bands as they are emptied by the tip, proceeding at a certain rate which can affect the magnitude of the tunnelling current. This then, in part, determines how the current and $\mathrm{d}I/\mathrm{d}V$ change with voltage.

On 1050 °C samples, donors are as plentiful at the surface as in the bulk and therefore the donor band exists up to the surface. Current from the donor band fills the DB states inelastically, at a rate that becomes greater as the levels are made higher [2]. Via this process current onset is observed at as low as –0.4 V.

The (0/–) state is close in energy to the dopant band, and so is filled at a fast rate through a near-elastic process. The (+/0) state has a much lower energy than the dopant band, so transitions from it to the (+/0) level are inelastic, the electrons losing energy through phonon emission or local vibronic excitation [39]; the filling rate is relatively slow. When band bending is great enough, the (+/0) level can be brought below the valence band edge in unbent regions deeper in

the bulk, and can be filled by tunnelling from this band. Tunnelling is elastic and much faster than the inelastic process necessary to fill the (+/0) state from the dopant band. The difference in filling rate between the two transition levels is the cause of the negative differential resistance observed on DBs on 1050 °C samples.

On 1250 °C samples, near surface donor atom concentration is reduced by as much as two orders of magnitude and as a result the donor band does not exist at the surface. Unlike in the bulk of the crystal where the Fermi level is within the conduction band, in this surface region the Fermi level is below the conduction band edge causing the surface region to be non-metallic. Electrons originating at the bulk conduction band must therefore traverse a barrier to reach the surface. A spattering of isolated non-ionized dopant atoms (as we are working at 4 K) remain in the surface region. At certain voltages, the tip field ionizes these single dopants, with donors nearer the surface ionizing at lower voltages. When a donor ionizes, the barrier in the near surface region is lowered slightly and the DB levels are filled at a greater rate. Experimentally, we observe a sharp rise in tunnelling current and a peak in $\mathrm{d}I/\mathrm{d}V$. Current begins to flow at relatively higher voltages, such as –1.6 V, and rises in a 'choppy' manner.

DBs probed on 1250 °C samples can still show effects relating to the different filling rates of the two transition levels, especially in regions where there happens to be an above average concentration of dopants remaining in the near surface region—enough to ensure a good supply of electrons to the surface. However, for most DBs on 1250 °C samples, current as a function of voltage is dominated by tip field ionization of the randomly distributed network of isolated dopants found near the DB. Accordingly, spectroscopy of DBs is highly varied on 1250 °C samples.

To empty a DB, tunnelling from a charge transition level to the tip is only allowed if there are empty tip states at that energy—when the tip Fermi level is below the transition level. Once allowed, the emptying rate is dependent on the matrix element for that process, increasing for a smaller tip-DB separation.

4.5 NEGATIVE DIFFERENTIAL RESISTANCE OF ISOLATED DBS

As mentioned before, on 1050 °C samples and sometimes on 1250 °C samples, spectroscopy over an isolated DB will exhibit negative differential resistance (NDR) between about –1.0 and –1.3 V. NDR is a general term for the phenomenon in some electrical devices where increasing the voltage across the terminals causes a decrease in current through them, first seen in the Esaki diode [40]. NDR associated with DBs can be understood by carefully considering the nature of the two charge transition levels, their filling and emptying rates, and the energetic alignment of the tip, DB, and bulk levels [2].

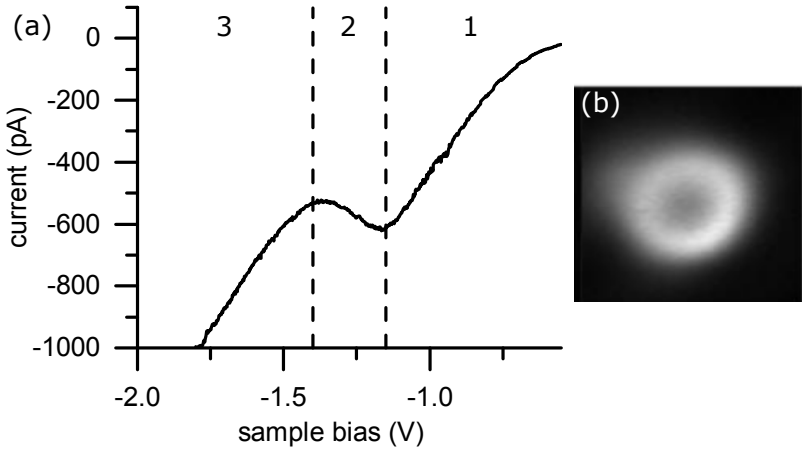

Figure 4.4: (a) *I–V* curve above a single DB on a 1050 °C sample at a –250 pm tip offset from the initial tip height of –1.8 V and 30 pA set over the DB. The three regimes are labelled, with NDR apparent in regime 2. (b) Constant height image of a single DB on a on a 1050 °C sample, at imaging conditions of –1.7 V and –210 pm tip offset.

An *I-V* curve over a DB on a 1050 °C sample is shown in Figure 4.4 (a). We identify three regimes, the first from the onset of the current rise (∼ –0.5,V) to the onset of NDR (∼ –1.1,V), the second to the onset of the second current rise (∼ –1.3 V), and the third at larger voltages. In the first regime (Fig. 4.5 (a)), the tip level is between the (0/–) and (+/0) levels—it can empty the former but not the latter. As the tip empties the (0/–) level it is easily filled by the dopant band and we observe an increase of current with sample bias.

Once the tip reaches the (+/0) level, that level can be emptied, thus eliminating the (0/–) level and turning off any current that was flowing through it (Fig. 4.5 (b)). For current to flow through the (0/–) level once more, the (+/0) level must be filled. Its slow filling rate from the dopant band thus limits the total tunnelling current, and the current lowers as the voltage is raised. NDR is only observed if the tip emptying rate is much greater than the filling rate of the (+/0) level, when the tip is close to the DB, and becomes more pronounced for smaller separation.

At a certain bias, the band bending of the tip brings the (+/0) level into resonance with the valence band edge, thereby allowing tunnelling from one to the other (Fig. 4.5 (c)). This filling is fast compared to the tip emptying rate, and so both the (+/0) level and the (0/–) level are able to effectively pass current: the current rises as voltage is increased.

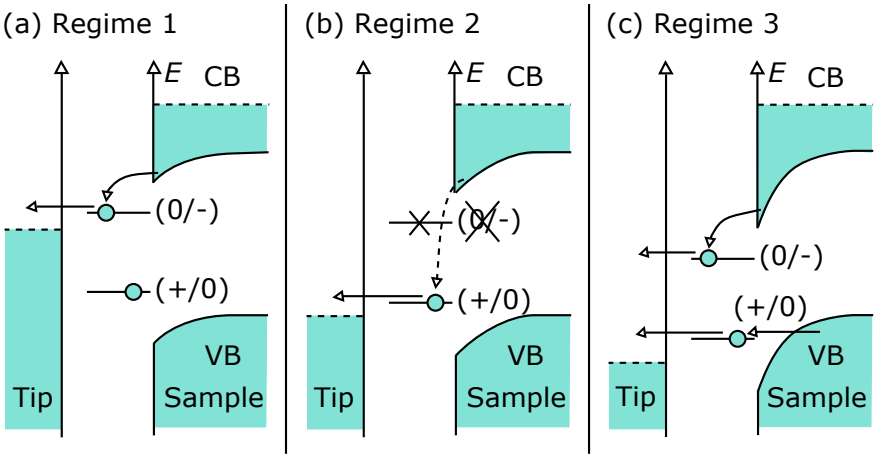

Figure 4.5: Regimes in spectroscopy of a single DB on a 1050 °C flashed sample. (a) Regime 1, where current flows easily from the conduction band (CB) through the (0/–) state into the tip: current rises with voltage. (b) Regime 2, where the tip can empty the (+/0) state faster than it can be filled by the dopant band, the slow filling of (+/0) represented by the dotted arrow. When it does, (0/–) is unavailable to conduct current: current falls with voltage and we observe NDR. (c) Regime 3, where band bending renders the valence band (VB) able to fill (+/0) at a fast rate through tunnelling: current again rises with voltage.

When imaging a DB in the NDR regime, we observe a bright ring surrounding a central dark region, as in Figure 4.4 (b). In the bright region, far from the DB laterally, the tip does not effectively empty the (+/0) level: the tunnelling current is not limited. The emptying rate increases as the tip moves closer, until at a certain distance it exceeds the filling rate, and the tunnelling current falls as the NDR effect becomes fully visible: the region just above the DB appears dark.

5

ATOMIC LINES

There exist several examples of atomic scale line structures composed of multiple close coupled surface defects studied in STM; we outline some important ones here. Alongside, we include numerical solutions to chosen 1 D potentials using the 1 D Schrödinger equation, designed to emulate the experiments and illustrate the basic physics at work.

5.1 1 D MODEL FOR LINEAR WELL STRUCTURES

The model we show here was initially developed to replicate that of a particular publication [4], where it was used to describe linear structures of close spaced dangling bonds with one intervening H atom; this publication is discussed in Section 5.5 and in Chapter 8. The wells used are Pöschl-Teller potentials, given by

$$V(x) = \frac{-\hbar^2\lambda(\lambda-1)}{2m\alpha^2\cosh^2(x/\alpha)} \tag{19}$$

where α = 0.24 nm sets the width of the well and λ = 2.2 sets the depth of the well. These constants were chosen such that its two bound states fit within the silicon bandgap, with the ground state at –0.95 eV, near the valence band maximum, and the first excited state at –0.02 eV, just below the conduction band, taken as 0 eV. It also does not exceed the Coulomb potential for a single electron and proton, $-e^2/4\pi\epsilon x$, where $\epsilon = (\epsilon_0 + \epsilon_{Si})/2$ is the average of the permittivity of vacuum and silicon. For these reasons, the authors considered it a good approximation of the DB energy well.

We use this potential well for illustrative purposes, varying its depth and the separation between multiple model wells to expound the different regimes of coupling between surface wells, as will be seen in the next examples. We note that the solutions found are for single particles in the potential. They do not consider inter-electron effects, such as coulombic repulsion and exchange coupling. For many

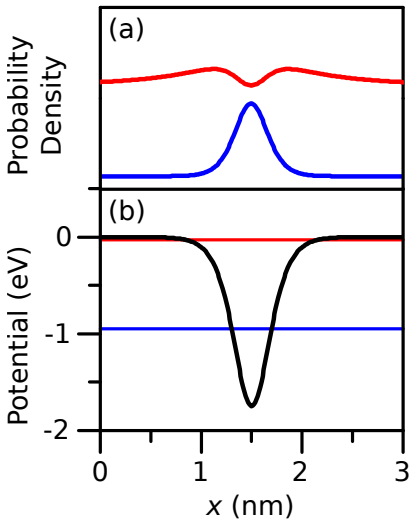

Figure 5.1: (a) Probability density of the two bound states of a Pöschl-Teller potential well, with lower to higher energy states plotted from bottom to top. (b) Plot of the potential well, with horizontal lines at –0.95 and –0.03 eV marking the energies of the two states.

systems, this works, as such effects are too weak to affect the single particle solutions significantly.

5.2 BONDING AND ANTIBONDING STATES

One of the consequences of two wells interacting is the formation of bonding and antibonding states, splitting from the initial single levels of each isolated well. We illustrate this in Figure 5.2, where we see that the initial isolated well level at –0.95 eV has split into a symmetric bonding state at –1.06 eV and an antisymmetric bonding state at –0.89 eV, a splitting of $\sim$ 0.2 eV.

Bonding and antibonding states have been characterized for various surface defect wells. We highlight the interaction of two wells formed through removal of two porphyrin molecules from dense-packed adsorbed arrays of molecules on the Ag(111) surface [15]. Taking dI/dV scans along the axis, the individual vacancy displayed a single peak in $\mathrm{d}I/\mathrm{d}V$ at $\sim$ 90 mV, while two coupled vacancies with one molecule between the two displayed a peak at $\sim$ 80 mV localized spatially between the two and $\sim$ 100 mV on each side of a vacancy furthest from the other.

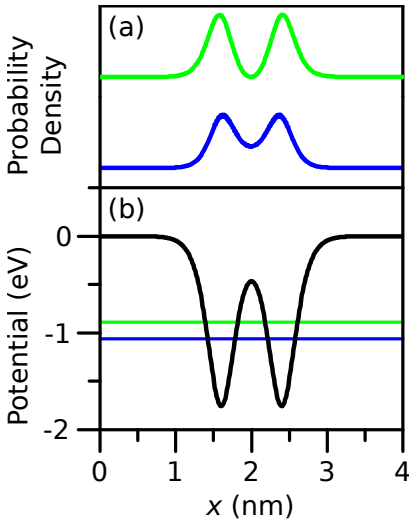

Figure 5.2: (a) Probability density of the bonding and antibonding states of two wells separated by 8 Å; the lower energy bonding state is plotted below the higher energy antibonding state. (b) Plot of the potential well, with horizontal lines at –1.06 and –0.89 eV marking the energies of the two states.

Cl vacancies on an NaCl bilayer atop a Cu(111) surface also produce coupling that, in its simplest case with two vacancies, produces a splitting of the states observed on an isolated vacancy [14]. The valency states at $\sim$ 2.8 V split into symmetric and antisymmetric states at $\sim$ 2.4 V and $\sim$ 2.9 V for three nearest neighbour separation and the localized interface states at $\sim$ –0.25 V split into states at $\sim$ –0.3 V and $\sim$ –0.23 V for five nearest neighbour separation.

Within the quantum dot system of close-spaced In adatoms on an InAs(111)*A*-2x2 surface, two quantum dots each composed of six In adatoms showed a splitting of the original –114 mV level into a –167 mV bonding and a –97 mV antibonding level with a separation of two vacancy sites between the two dots [41]. The formation of the quantum dots themselves will be discussed in the next section.

5.3 MULTIPLE INTERACTING WELLS

When multiple wells are brought close together, bound states take on features of 1 D particle in a box states, where each higher energy state has one more peak in probability density than the one before; the

lowest energy state has one peak. We identify two different regimes: weakly interacting wells and strongly interacting wells.

5.3.1 *Weakly Interacting Wells*

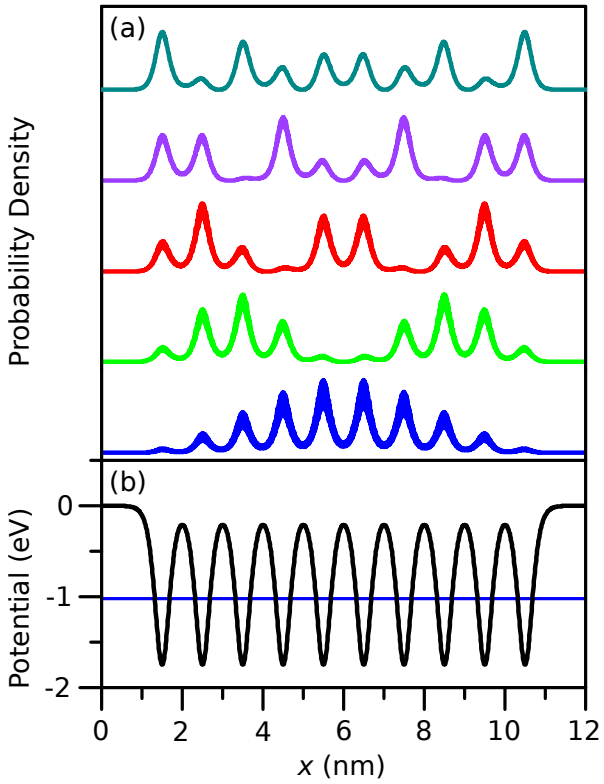

Figure 5.3: (a) Probability density of the first five bound states of ten wells with 10 Å spacing. The states, of energy –1.02, –1.01, –1.00, –0.99, and –0.97 eV, are plotted in order of ascending energy from the bottom to the top of the frame. (b) Plot of the potential well, with a horizontal line at –1.02 eV marking the energy of the first bound state.

Here, the wells are brought close enough together to interact, but far enough apart that each well maintains its basic shape. We see pronounced barriers between the wells. The resulting bound states exhibit peaks in probability density that remain centred over each well, but the envelope that encloses the peaks resembles 1 D particle in a box states. We see this regime in Figure 5.3, where we plot the lowest five calculated bound states of ten wells with 10 Å spacing. The

energy spacing between them is nearly equal, $\sim$ 0.01 eV, as expected for particle in a box states.

5.3.2 *Strongly Interacting Wells*

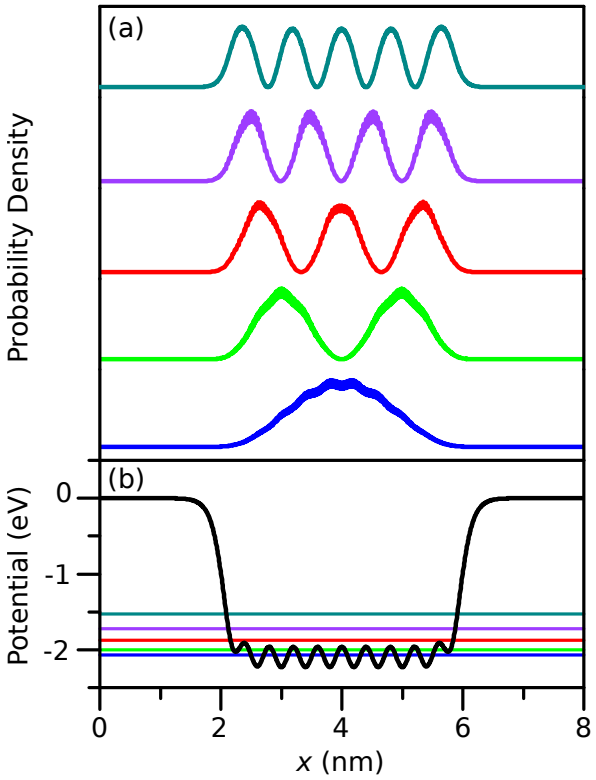

Figure 5.4: (a) Probability density of the first five bound states of ten wells with 4 Å spacing. The states, of energy –2.07, –2.00, –1.88, –1.72, and –1.53 eV, are plotted in order of ascending energy from the bottom to the top of the frame. (b) Plot of the potential well, with horizontal lines marking their energies.

If the wells are brought close enough for each to overlap greatly, the final potential appears as one large well with ripples at the bottom. The probability density peaks of the bound states are no longer localized over each well, instead totally delocalized over the entire ensemble, taking the form of 1 D particle in a box states. This regime is modelled in Figure 5.4, where the lowest five calculated bound states of ten wells with 4 Å spacing are shown. The energy spacing between states is not equal, those states with energy within the ripple at the

bottom of the potential spaced at ~ 0.1 eV and those above the ripple spaced at ~ 0.2 eV.

There are many examples of 1 D electron quantization in the literature. Most involve many metal adatoms coupling on a certain surface to form the 1 D band. The main examples are Au adatoms on a NiAl(110) surface [11], Cu adatoms on a Cu(111) surface [12, 13], and Ag adatoms on a NiAl substrate [42]. In the case of the Ag adatoms, photon emission was measured from transitions between two of the 1 D states described. The Si(111)-(5x2)-Au surface displays self-assembled Au atomic wires truncated by Si adatoms. Here the Si adatoms "act as strong scatterers to confine and quantize 1 D electrons" [43].

As mentioned in Section 5.2, In adatoms on an InAs(111)*A* surface, when placed in the closest spaced arrangement possible, form weakly interacting wells as described here, the 1 D particle in a box envelope clearly visible [41, 44]. Each In adatom acts as a well for surface states of the surface, confining them and forming the quantized states described. Furthermore, the Cl and porphyrin vacancies described in that section both form 1 D particle in a box states [14, 15] when more than two wells are placed close to one another.

5.4 END STATES

When a three dimensional crystal terminates, the bulk crystal arrangement is often no longer energetically favourable for the surface atoms. A reconstruction occurs in this case, with surface structure different from the bulk. A famous example is the Si(111)-7x7 reconstruction, which supports new 2 D surface states not found in the bulk [6, 45]. Similarly, the edges of 2 D structures often support 1 D states [46]. In the case of 1 D structures, we can expect zero dimensional 'end states' to form, as the end atoms reconstruct slightly.

In Figure 5.5, we extend our 1 D model to include end states by taking the ten-well structure of 10 Å spacing and setting $\lambda = 3$ for the two end atoms. We effectively make the end wells deeper than the body wells, approximating a reconstruction of end atoms that supports end states. The two degenerate lowest energy states are zero dimensional, each localized to one of the two end atoms. At greater

energy, the regular 1 D particle in a box envelope states are visible, but only over the inner eight wells; the end wells do not support the 1 D band.

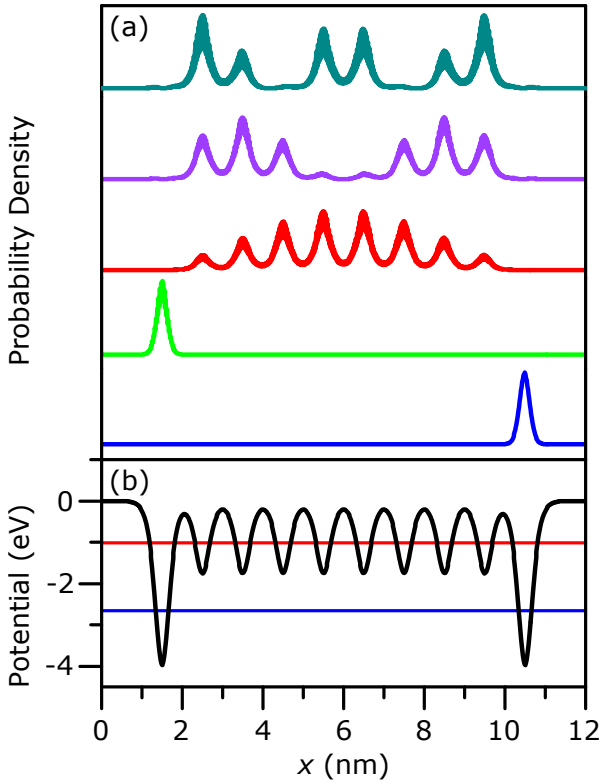

Figure 5.5: (a) Probability density of the first five bound states of ten wells with 10 Å spacing, with the two end wells of greater depth. The states, of energy –2.65, –2.65, –1.02, –1.01, and –1.00 eV, are plotted in order of ascending energy from the bottom to the top of the frame. (b) Plot of the potential well, with a horizontal line at –2.65 and –1.02 eV marking the energy of the degenerate end states and the first 1 D particle in a box state.

Similar local zero dimensional end states have been observed at the ends of gold chains self assembled on the vicinal Si(553) surface [47], and the ends of Fe adatom chains on an InAs(100) surface [48].

5.5 SILICON DANGLING BOND LINES

We turn now to previous work with silicon dangling bond lines, work which our study greatly builds upon and expands. The first study

fabricated lines by setting a high voltage and setpoint current (~ -3 V, ~ 1 nA) and scanning over a line on to the surface. This relatively crude fabrication method led to many errors in patterning. Still, lines of single DBs across and along dimer rows in the closest spacing possible were fabricated [49].

In a subsequent publication, DB chains of the type we present here, along one side of a dimer row in the closest spacing possible (3.84 Å), were fabricated; those of length up to five DBs were characterized with constant current imaging in filled and empty states [23]. In filled states, the authors found that 2 DB chains imaged with both DBs bright, 3 DB chains with the two end DBs bright, 4 DB chains with all four bright, and 5 DB chains with only the end DBs and the middle DB bright.

They explained their observations as a Jahn-Teller distortion occurring for the Si atoms of each DB, the electronic sharing between the DBs of the chain forcing a lattice relaxation along its length. This distortion results in the Si atoms of the chain to be shifted slightly above or below the surface plane, in an alternating fashion along the chain. The brighter DBs are those of Si atoms shifted above the plane, the darker DBs those of Si atoms below the plane. For even numbered chains, specifically the 4 DB chain, they explained the appearance of four bright DBs, not two as would be expected from this explanation, as a thermally induced 'flipping' between two bistable Jahn-Teller configurations at a much faster rate than the STM can resolve in time. The measured signal is the average between the two.

The electronic structure of dangling bond lines of different width along a dimer row was explored previously. DB Chains of 7 DBs long were patterned and characterized with $\mathrm{d}I/\mathrm{d}V$ mapping techniques, along with single, double, and triple bare dimer lines patterned adjacent to one another [24]. For all structures but the DB chains, 1 D electron quantization as discussed in Section 5.3 was visible in empty state $\mathrm{d}I/\mathrm{d}V$ imaging, at energies corresponding to the π^* band of a bare dimer.

Close spaced linear arrangements of DBs, with a separation of 7.68 Å between DBs, were patterned by desorbing one H atom at a time and characterized with filled and empty state imaging at various voltages and setpoint currents [4]. They claimed that bright features seen between the DBs at certain imaging conditions are signatures of

molecular orbitals formed through interaction between DBs. A thorough discussion of the work, including comparison with some new experimental observations we have made, is found in Chapter 8.

6

DANGLING BOND CHAINS

As discussed before, the overlap between close spaced DBs can form molecular orbitals. The most well-known example is that of the π and π^* orbitals formed on a dimer structure of the reconstructed Si(100) surface [37, 38]. The next closest spacing possible is along a dimer row, 3.84 Å. The dimer row allows for any number of DBs at this spacing in a linear arrangement, forming structures we call DB chains.

6.1 CREATING DB CHAINS

DBs can be created with the STM upon application of a 2 to 3 V sample bias voltage pulse over an H atom. A significant portion of the tunnelling current excites vibrations in the H-Si bond faster than can be dissipated in the lattice, eventually breaking the bond [50, 51]. The process can be modelled as a truncated harmonic oscillator, where inelastic tunnelling electrons increase the oscillator energy to beyond an effective bond energy barrier [51]. Because the STM is able to inject current into single H-Si bonds, we can pattern DBs one at a time. We used this desorption method to pattern DB Chains.

A LabVIEW program was developed by members within the group to pattern DBs automatically. The user must calibrate with the surface measured by the STM by adjusting two variables: surface lattice constant and angle. The pattern is chosen and the tip is moved to the start point defined by the user upon which this sequence proceeds:

1. The feedback loop is turned off and the tunnelling current of a 'check' voltage is recorded.

2. To desorb, a train of progressively larger voltage pulses is applied in concert with a tip movement closer to the sample, between which the tunnelling current at the check voltage is compared to the initial value. If it shows significant change, it is assumed a DB is created, as DBs generally conduct a greater current for a given height at normal check voltages; they are

higher than H-Si in constant current images. There is a maximum pulse magnitude that when reached ends this step if no DB creation is detected.

3. The feedback loop is reactivated, the tip is moved to the next spot, and the process is repeated.

Once finished, STM images were taken to evaluate the success or failure of the pattern before further characterization.

6.1.1 *Patterning Errors*

The program knows where to place the DBs by extrapolating from the start point based on the calibration factors. Improper calibration and the effects of drift and creep will cause divergence of the tip placement and the desired DB location, leading to errors.

Breaking the H-Si covalent bond necessitates rather extreme tunnelling conditions that can change the tip, most often for the worse. If the tip changes during patterning, the pattern invariably fails. Even if it remains sharp, a shift in the calibration will be introduced.

Sometimes, because of its local environment, a particular H atom will require an unusually high voltage pulse to desorb, greater than the maximum set by the program. The completed pattern will be missing this DB. Returning to the spot, the necessary voltage is often so high that neighbouring H atoms are desorbed or the tip is changed.

Some DBs have the tendency to flip to the other side of the dimer row, spurred by a high negative sample bias voltage (>–2.1 V) during fabrication or, more commonly, characterization of the chain. Although isolated DBs can be controllably flipped on a dimer row with voltage pulses, we have not to date been able to flip a DB back into a chain configuration.

6.1.2 *Desorption Parameters & Success Rate*

Through trial and error, we found a set of parameters that worked often enough to enable a characterization of DB chains. We stress that further optimization is possible, but it is not the focus of this study.

We used feedback settings of –1.8 V and 50 pA, a check voltage of –1.8 V, and a 10 ms pulse width for all samples. The tip movement and maximum pulse voltage were varied based on the particular tip and sample and errors occurring that day. For example, if many 'no desorption' errors were occurring, the tip movement or the maximum voltage would be increased. Tip movement varied from 20 pm to 45 pm and maximum voltage pulses from 2.3 V to 3.0 V. We noticed that larger tip movement and smaller maximum pulses were optimal for 1250 °C samples, with the opposite for 1050 °C samples.

6.2 CHARACTERIZING DB CHAINS

To achieve a tunnelling current through whatever mid-gap states we probe, a dynamic equilibrium must be established as the mid-gap levels are emptied by the tip and filled by the bulk bands. They are filled primarily through inelastic processes from the donor band. The dopant concentration profile and the shape of the donor band thus has a profound effect on the current flow through the levels and subsequently any measurements we make.

6.2.1 *Constant Current STM images*

We patterned DB chains up to 7 DB long. In empty state images all chains take on the form of a single elongated bright spot along the chain axis. In filled state images they take on more complex forms, with bright spots that do not necessarily correspond to the number of DBs on the chain. We see this in Figure 6.1, where the 3 DB chain appears to have two bright spots and the 5 DB Chain appears to have four.

6.2.2 *dI/dV Mapping*

To explore the electronic structure of these chains, we employed $\mathrm{d}I/\mathrm{d}V$ mapping. In this mode of imaging, we recover the surface local density of states, or LDOS. The tip height and maximum probing voltage during mapping was variable, chosen as a compromise between signal strength and chain stability. At the proper tip height the tun-

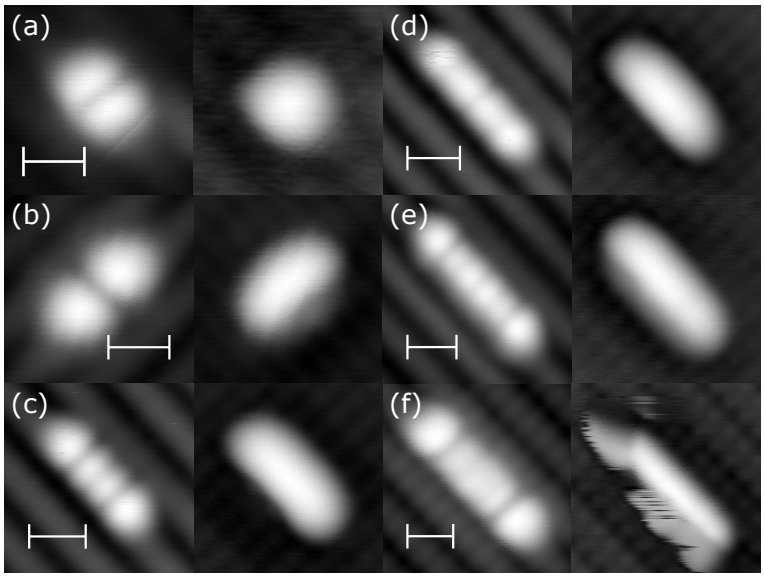

Figure 6.1: Constant current images of DB Chains (a) 2 DB, (b) 3 DB, (c) 4 DB, (d) 5 DB, (e) 6 DB, and (f) 7 DB long. For a pair, images on the left and right are of filled states and empty states at –1.8 and 1.4 V, 50 pA. Each scale bar is 1 nm; each pair of images has the same scale.

nelling current routinely reached hundreds of pA during mapping; a higher current risks destroying the chain. Because 1050 °C samples are more conductive than 1250 °C samples, we found that the tip had to be further away with a smaller maximum voltage than on 1250 °C samples.

H-Si regions within dI/dV maps and linescans show almost no signal. At the voltages and tip heights used in mapping, very little tunnelling current flows through them compared to that which flows through the DB chain. Furthermore, being a passivated region, there are no surface states to measure. The only signal in filled states is from the valence band, with little interesting variation in dI/dV. In some dI/dV maps, in concurrence with a low signal from the chain, we sometimes see a slight variation in the H-Si regions resembling dimer rows in filled state images. In all cases, however, the signal from the DB chain eclipses that from over H-Si.

We present a number of fully characterized DB chains from 2 to 7 DB long, including constant current images and dI/dV maps and linescans. For all but the 7 DB chain, we had at least one example on a 1050 and a 1250 °C sample. As noted earlier, 1050 °C samples have

an intact donor band up to the surface, whereas 1250 °C samples do not, as the flashing temperature is so high that dopants as deep as 150 nm evaporate and are removed from the sample [33].

There are similarities between different chains of the same length; we present a taxonomy.

6.2.3 *2 DB Chains*

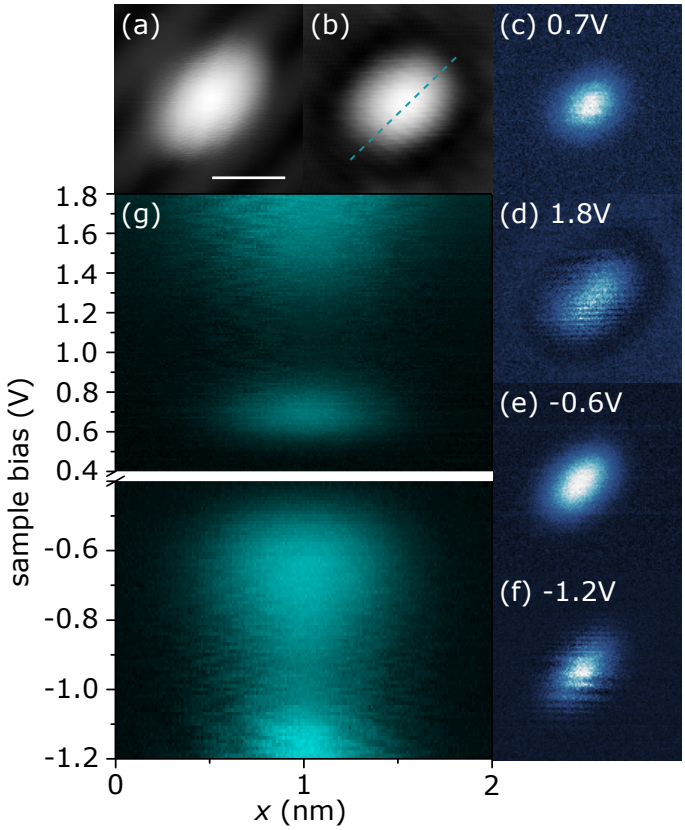

Figure 6.2: Two DBs with zero intervening H atoms, or a 2 DB chain, on a 1050 °C sample. (a,b) STM images at –1.8 and 1.4 V, 50 pA. (c-f) dI/dV maps at constant voltages. (g) dI/dV linescans over the dotted line in (b). The tip height for dI/dV mapping was –1.8 V, 20 pA with 60 pm tip retraction over H-Si. The scale bar in (a) is 1 nm long and is the same scale for (a-f).

Looking at the 2 DB chain on a 1050 °C sample (Fig. 6.2), the STM images (a,b) do not show two distinct DBs, the structure appearing as a single bright spot in both filled and empty states. In empty states,

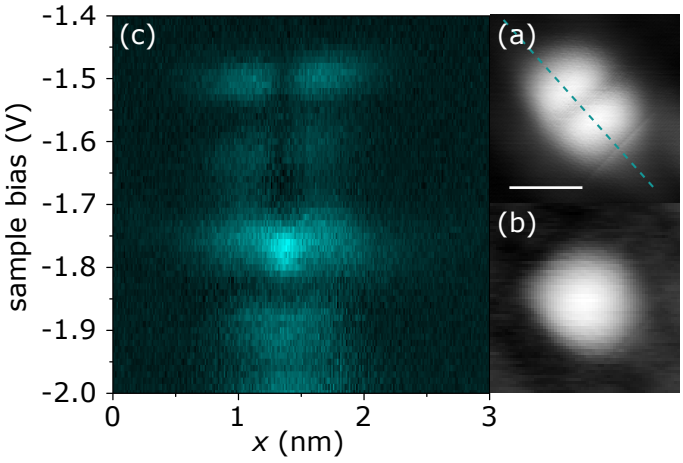

Figure 6.3: 2 DB chain on a 1250 °C sample. (a,b) Constant current images at –1.8 and 1.4 V, 50 pA. (c) Constant height dI/dV linescans over the dotted line in (a). The tip height for dI/dV mapping was –1.8 V, 20 pA over H-Si. The scale bar in (a) is 1 nm long and is the same scale for (b).

dI/dV linescans reveal one feature of spatial extent from about 0.75 to 1.25 nm at voltages between 0.6 and 0.8 V before disappearing, seen in the dI/dV map (c). As the voltage is increased further, another feature starts to appear at about 1.2 V between 0.5 and 1.5 nm. Its map is shown in (d), in which the black halo surrounding the feature is likely the same as a halo around a single DB, as discussed in Section 4.4.2. In both dI/dV linescans and maps, the first feature is spatially smaller than the second, the first approximately occupying the region from the centre of one DB to the centre of the other and the second occupying a region that encompasses both DBs. In filled state dI/dV linescans, a single feature appears at –0.5 V between 0.5 and 1.5 nm. The magnitude of its dI/dV signal peaks in intensity at –0.7 V, before reducing until –1.0 V, where it begins to rise again; dI/dV maps are shown in (e) and (f).

Figure 6.3 shows a 2 DB chain on a 1250 °C flashed sample, with filled and empty state constant current images visible in (a) and (b). This early result does not have constant height dI/dV maps associated with it, only the constant height dI/dV linescans in (c). Looking at the dI/dV linescans, we see two features appear at –1.45 V, centred over each DB, until –1.73 V, where a central bright feature emerges, tapering off in intensity away from the centre to each side above the two

DBs. At –1.8 V, we see only a single bright feature, with no apparent structure, until the maximum voltage probed.

6.2.4 *3 DB Chains*

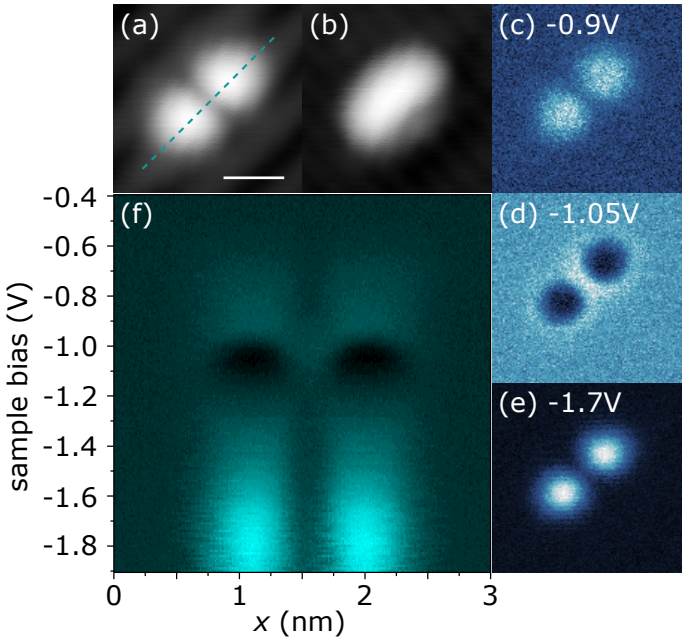

Figure 6.4: 3 DB chain on a 1050 °C sample. (a,b) Constant current images at –1.8 and 1.4 V, 50 pA. (c-e) Constant height dI/dV maps at constant voltages. (f) Constant height dI/dV linescans over the dotted line in (a). The tip height for dI/dV mapping was –1.8 V, 20 pA with 60 pm tip retraction over H-Si. The scale bar in (a) is 1 nm long and is the same scale for (a-e).

Figure 6.4 shows a typical 3 DB chain on a 1050 °C sample, exhibiting certain patterns in dI/dV mapping that have been replicated a total of four times. In dI/dV linescans (f), we first see two bright features as the voltage increases up to –1.0 V, upon which the two go 'dark', and exhibit negative differential resistance (NDR). In the dI/dV map (d), we see the NDR regions are in fact surrounded by two faint circles, the brightest part of which is the point where the two circles touch. The two bright features reappear at about –1.15 V, seen in map (e). As discussed in Chapter 4, NDR means that dI/dV is negative, and is apparent in dI/dV linescans (f) and maps (d) as

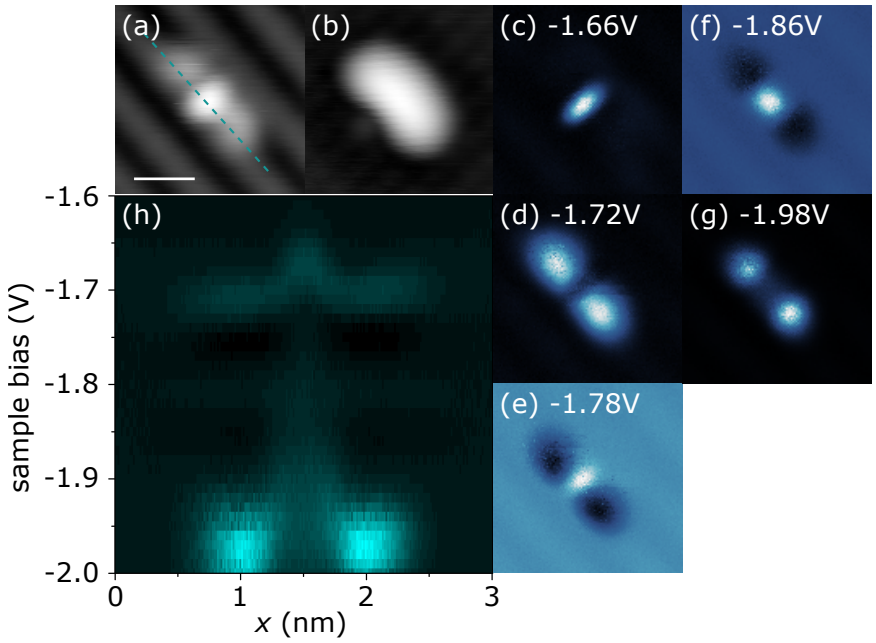

Figure 6.5: 3 DB chain on a 1250 °C sample. (a,b) Constant current images at –1.8 and 1.4 V, 50 pA. (c-g) Constant height dI/dV maps at constant voltages. (h) Constant height dI/dV linescans over the dotted line in (a). The tip height for dI/dV mapping was –2 V, 50 pA over H-Si. The scale bar in (a) is 1 nm long and is the same scale for (a-g).

black regions, darker than the background 'zero' signal obtained over H-Si.

Figure 6.5 shows our only example of a 3 DB chain on a 1250 °C sample. There is a repetition of dI/dV patterns evident, one cycle occurring from –1.65 to –1.8 V and the other from –1.8 V and above. In dI/dV linescans (h) there first appears one central feature, seen in the dI/dV map (c) that splits into two at about –1.68 V, seen in the map (d). At –1.74 V, the two features go 'dark' and exhibit NDR at their locations, while showing a central bright feature, as seen in the map shown in (e). For the second cycle, the single bright feature starts at about –1.82 V, seen in map (f), and exhibits NDR at the two positions mentioned before. This single feature turns to two at –1.92 V, seen in the map (g). We do not see the third pattern in the second cycle, presumably because we do not probe past –2.0 V.

For all 3 DB chains, in empty state STM images, we see a 'mushroom' shape, where the 'cap' is the elongated, slightly bent, bright

feature along the length of the chain and the 'stem' is the H atom, slightly brighter than all others, on the other side of the dimer row in the middle of the chain. This bright H atom images brighter because it is likely raised in relation to the other H atoms on the surface. This is a strong indication of major lattice relaxation present with DB chains.

6.2.5 *4 DB Chains*

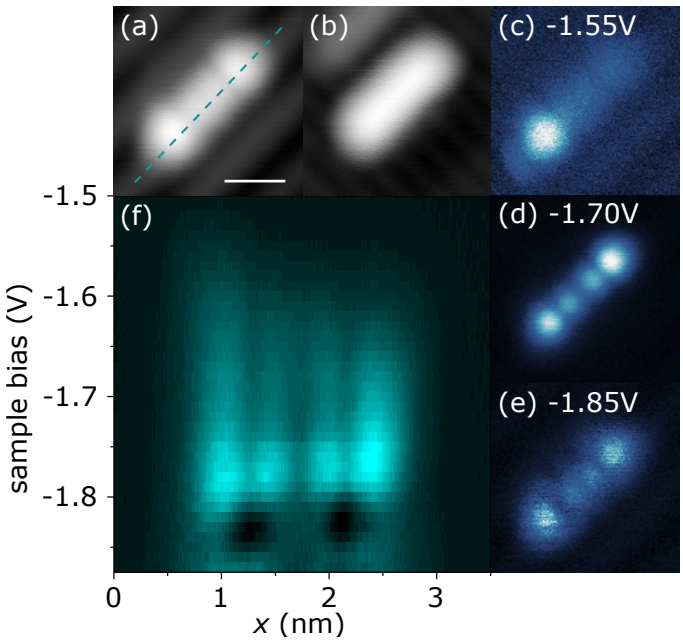

Figure 6.6: 4 DB chain on a 1050 °C sample. (a,b) Constant current images at –1.8 and 1.4 V, 50 pA. (c-e) Constant height dI/dV maps at constant voltages. (f) Constant height dI/dV linescans over the dotted line in (a). The tip height for dI/dV mapping was –1.8 V, 20 pA over H-Si. The scale bar in (a) is 1 nm long and is the same scale for (a-e).

The 4 DB chain on a 1050 °C flashed sample shown in Figure 6.6 appears in dI/dV linescans as four bright features up to –1.8 V, seen in dI/dV map (d), at which point the central two features merge and form a total of three, with two slight NDR regions interspersed, until –1.85 V. There are the beginnings of a further pattern evident in the linescans of this 1050 °C chain, but we do not resolve it.

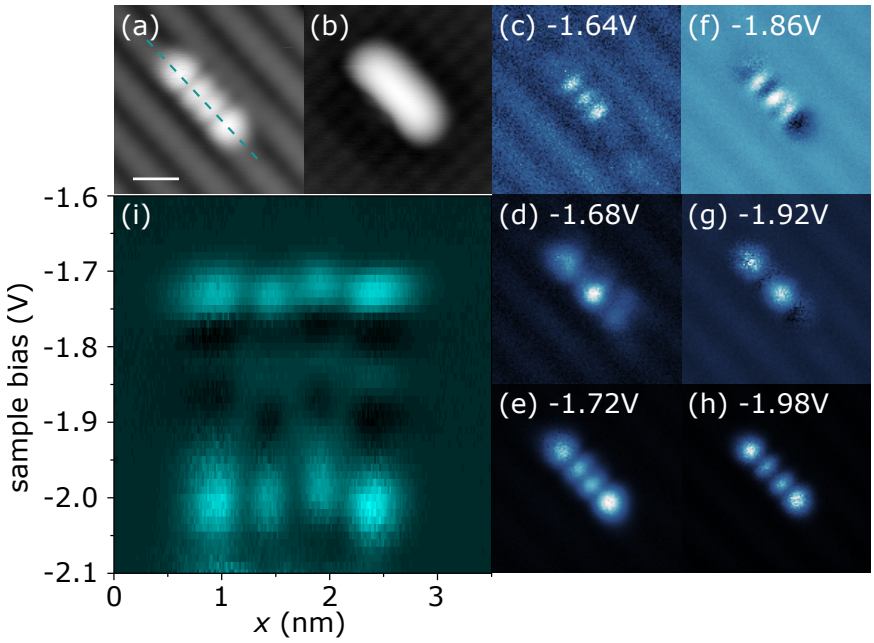

Figure 6.7: 4 DB chain on a 1250 °C sample. (a,b) Constant current images at –1.8 and 1.4 V, 50 pA. (c-h) Constant height dI/dV maps at constant voltages. (i) Constant height dI/dV linescans over the dotted line in (a). The tip height for dI/dV mapping was –2 V, 20 pA over H-Si. The scale bar in (a) is 1 nm long and is the same scale for (a-h).

The 1250 °C chain in Figure 6.7 was made by extending the 3 DB chain seen in Figure 6.5. Just as its progenitor, in dI/dV linescans (h), there is a cycling between certain patterns twice, once from –1.64 to –1.8 V and again from –1.86 to –2.1 V. There are first three features until –1.7 V, seen in the dI/dV map (c), followed by four bright features, seen in map (e). The central energies of the four features appear to alternate with respect to an equipotential line, an asymmetry borne out in the dI/dV map (d), possibly indicating a buckling of the molecule. When the pattern repeats, the first three bright features show four regions of NDR interspersed, exhibiting the same asymmetry, where the four bright features once were. The dividing voltages for the second repetition are –1.95 and -2.05 V.

6.2.6 *5 DB Chains—A Type*

Examining 5 DB chains, we identify two different types, which we call A and B type. In experiments, the two exhibit a different progression of dI/dV patterns, each having been replicated three times.

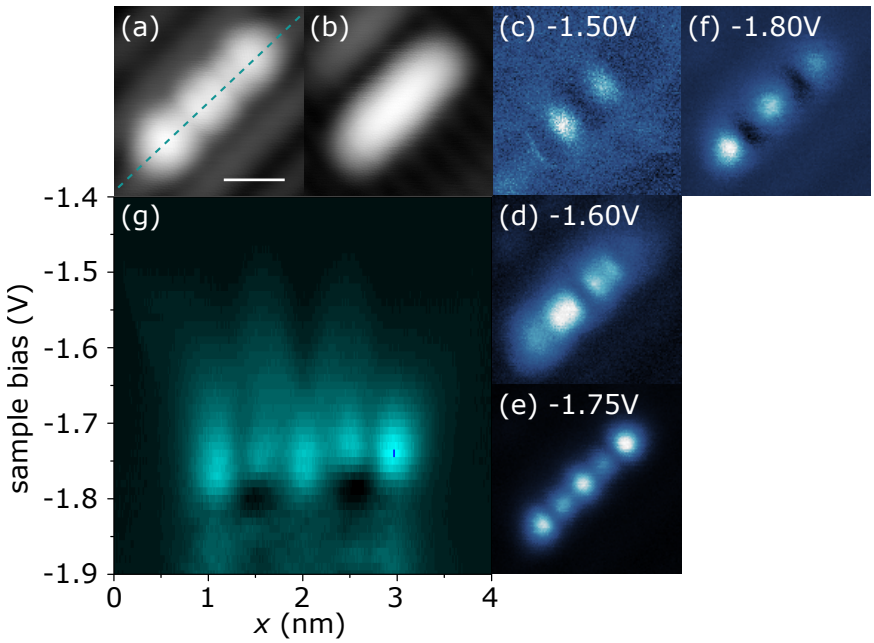

Figure 6.8: 5 DB chain on a 1050 °C sample. (a,b) Constant current images at –1.8 and 1.4 V, 50 pA. (c-f) Constant height dI/dV maps at constant voltages. (g) Constant height dI/dV linescans over the dotted line in (a). The tip height for dI/dV mapping was –1.8 V, 20 pA over H-Si. The scale bar in (a) is 1 nm long and is the same scale for (a-f).

Two examples of A types are shown in Figures 6.8 and 6.9, chains which were made by extending the 4 DB chains shown in Figures 6.6 and 6.7. In the dI/dV linescans of Fig. 6.8 (g) and 6.9 (k) we see two bright features, shown in dI/dV maps Fig. 6.8 (c) and 6.9 (c) that split into four at about –1.55 V. These four, as seen in maps Fig. 6.8 (d) and 6.9 (d), persist until –1.74 V, where we see five whose central energies appear to alternate with respect to an equipotential line in linescans, much as described for the 4 DB chain in Figure 6.7, possibly indicating physical lattice buckling. dI/dV maps of the five are found in Figures 6.8 (e) and 6.9 (e). At –1.8 V the five go dark, and on the 1050 °C chain we see three bright features with two NDR regions interspersed, as in

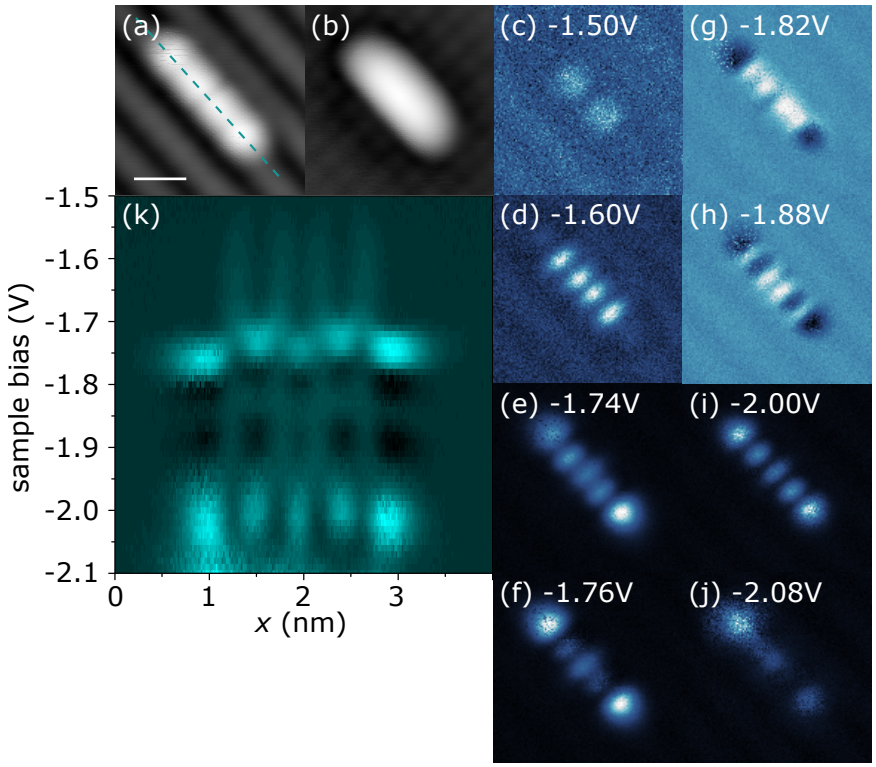

Figure 6.9: 5 DB chain on a 1250 °C sample. (a,b) Constant current images at –1.8 and 1.4 V, 50 pA. (c-j) Constant height dI/dV maps at constant voltages. (k) Constant height dI/dV linescans over the dotted line in (a). The tip height for dI/dV mapping was –2 V, 20 pA over H-Si. The scale bar in (a) is 1 nm long and is the same scale for (a-j).

map Fig. 6.8 (f). On the 1250 °C chain we see five NDR regions where the five bright features once were.

In the 1250 °C chain we see this pattern occurring at the voltages above before repeating once more starting at about –1.82 V. The dividing voltages for the second repetition are –1.85, –1.9, –1.95, and –2.5 V. This repetition is much like that of the 3 and 4 DB chains in Figures 6.5 and 6.7 that the 5 DB chain was made from.

6.2.7 *5 DB Chains—B Type*

We show two B type chains in Figures 6.10 and 6.11. While sharing the same progression, the dI/dV patterns of the two do not appear at the same voltages.

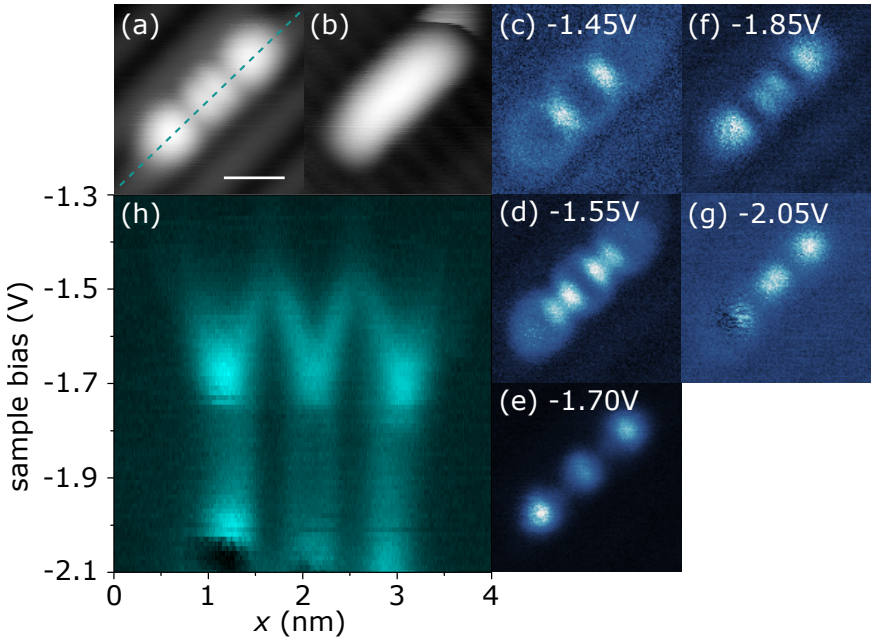

Figure 6.10: 5 DB chain on a 1050 °C sample. (a,b) Constant current images at –1.8 and 1.4 V, 50 pA. (c-g) Constant height dI/dV maps at constant voltages. (h) Constant height dI/dV linescans over the dotted line in (a). The tip height for dI/dV mapping was –1.8 V, 20 pA with 40 pm tip retraction over H-Si. The scale bar in (a) is 1 nm long and is the same scale for (a-g).

On linescans of the 1050 °C chain, Fig. 6.10 (h), we see four features until –1.5 V which appear as three bright circles in the dI/dV map (c). The three circles split off from one another, as seen in map (d), the brightest regions being the parts of each circle adjacent to another. In linescans this stage appears as the central two of the four features splitting into two each, these four more pronounced than the outer two. The six features merge into three at –1.6 V, seen in map (e), until –1.75 V. Here the central feature splits into two until –2 V, seen in map (f), where the two again merge to form three, seen in map (g) until the maximum voltage probed.

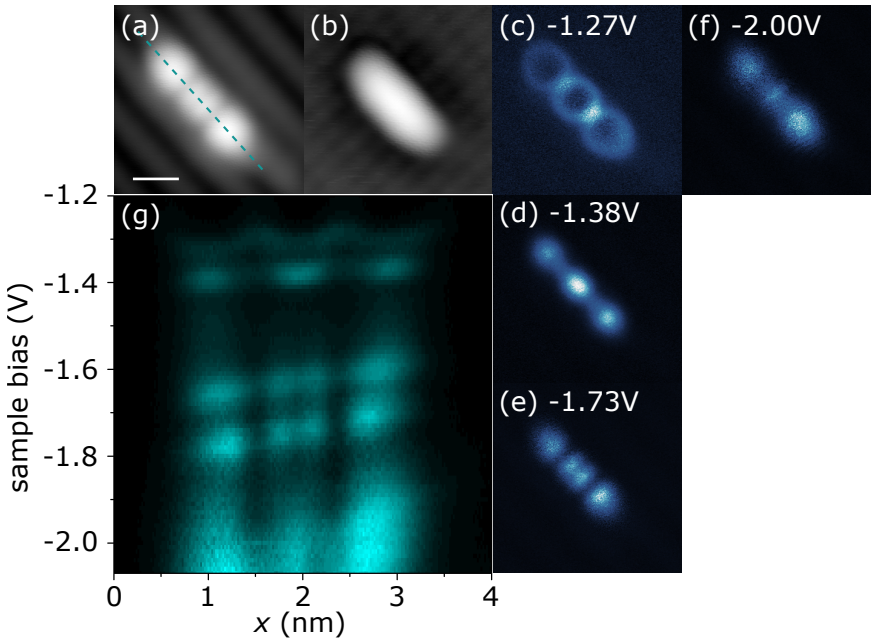

Figure 6.11: 5 DB chain on a 1250 °C sample. (a,b) Constant current images at –1.8 and 1.4 V, 50 pA. (c-f) Constant height dI/dV maps at constant voltages. (g) Constant height dI/dV linescans over the dotted line in (a). The tip height for dI/dV mapping was –2 V, 20 pA over H-Si. The scale bar in (a) is 1 nm long and is the same scale for (a-f).

On the linescans of the 1250 °C chain, Fig. 6.11 (h), the boundaries between patterns are at –1.3 V, –1.35 V, –1.5 V, and –1.9 V. The second state seen when the three circles split is absent in its dI/dV maps, because of its thin voltage range. However, it is clearly visible in linescans as the middle of the 'triple v' shape from –1.3 to –1.35 V.

6.2.8 *6 DB Chains*

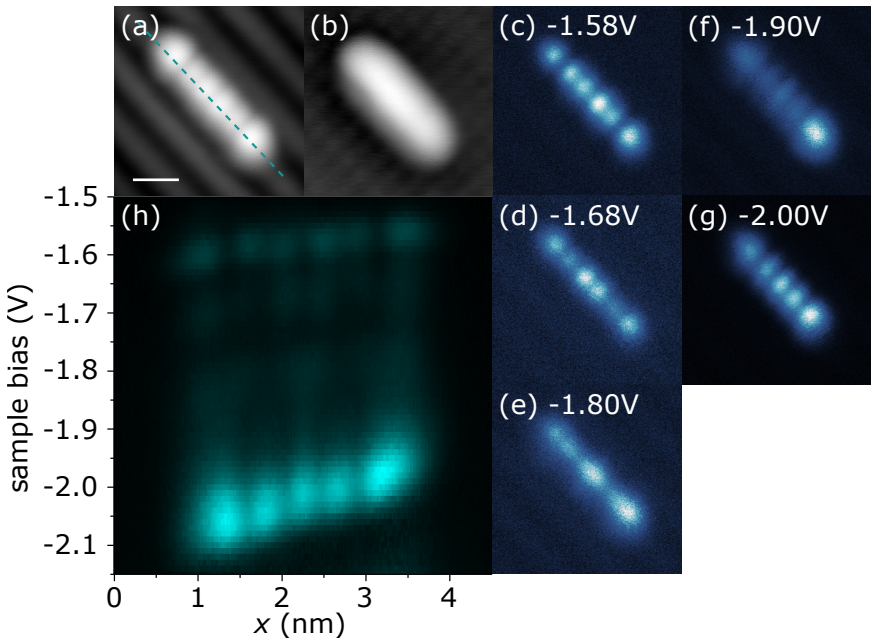

Figure 6.12: 6 DB chain on a 1250 °C sample. (a,b) Constant current images at –1.8 and 1.4 V, 50 pA. (c-g) Constant height dI/dV maps at constant voltages. (h) Constant height dI/dV linescans over the dotted line in (a). The tip height for dI/dV mapping was –2.0 V, 20 pA over H-Si. The scale bar in (a) is 1 nm long and is the same scale for (a-g).

The 6 DB chains shown here share the same progression of dI/dV patterns, replicated a total of 4 times in our experiments. Looking at their linescans, Fig. 6.13 (h) and 6.12 (h) for 1050 and 1250 °C respectively, six bright features are evident from –1.55 V, seen in dI/dV maps Fig. 6.13 (d,e) and 6.12 (c,d). They end at about –1.77 V, those in the middle of the chain at a sooner voltage than those at the end. Three features then come forward until about –1.85 V, seen in maps Fig. 6.13 (f) and 6.12 (e), before two more appear interspersed between the three, for a total of five features, seen in maps Fig. 6.13 (g) and 6.12 (f,g), up to the maximum voltage.

The 1050 °C chain is an extension of the 5 DB chain in Figure 6.8. Compared to the 1250 °C chain, its dI/dV linescans Fig. 6.13 (h) show four features before the inner two split into the familiar six at –1.55 V, also seen in the dI/dV map Fig. 6.13 (c). The four features may not

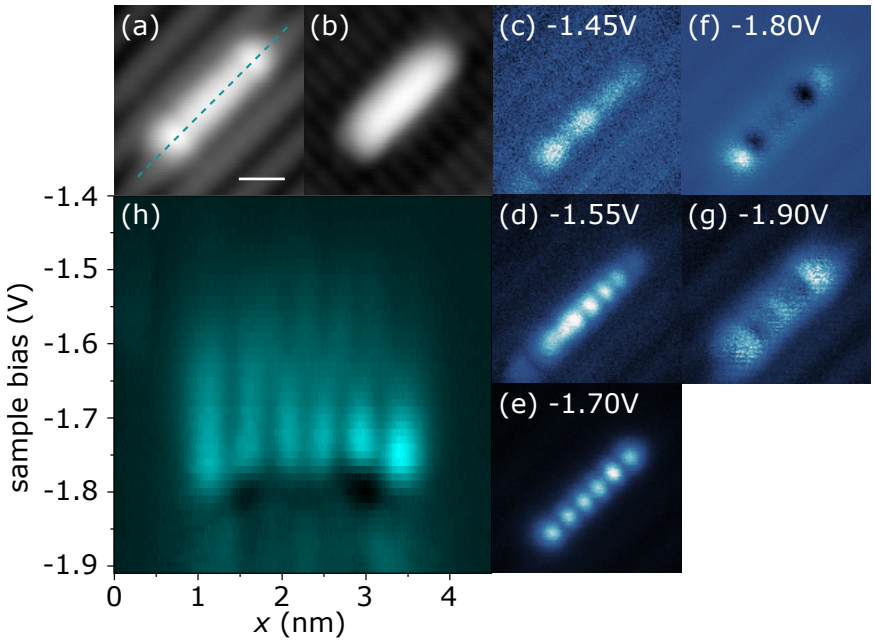

Figure 6.13: 6 DB chain on a 1050 °C sample. (a,b) Constant current images at –1.8 and 1.4 V, 50 pA. (c-g) Constant height dI/dV maps at constant voltages. (h) Constant height dI/dV linescans over the dotted line in (a). The tip height for dI/dV mapping was –1.8 V, 20 pA over H-Si. The scale bar in (a) is 1 nm long and is the same scale for (a-g).

be apparent on the 1250 °C chain because the doping level is too low to allow current at these voltages. The 1050 °C chain also shows NDR regions between the three bright features at about –1.8 V, seen in the dI/dV map Fig. 6.13 (f).

6.2.9 *7 DB Chains*

Because the likelihood of successfully fabricating chains reduces as their length increases, we only characterized one 7 DB chain, shown in Figure 6.14. It is our longest chain, our preeminent example of electronic complexity formed through close-spaced DB coupling.

In Figure 6.14, looking at the dI/dV linescans (h) we see five features at the lowest voltages with the central one dominant, also seen in dI/dV maps (c,d). That central feature splits into two before merging with those on either side at about –1.1 V, where roughly four equally prominent features are evident. The central two are tilted

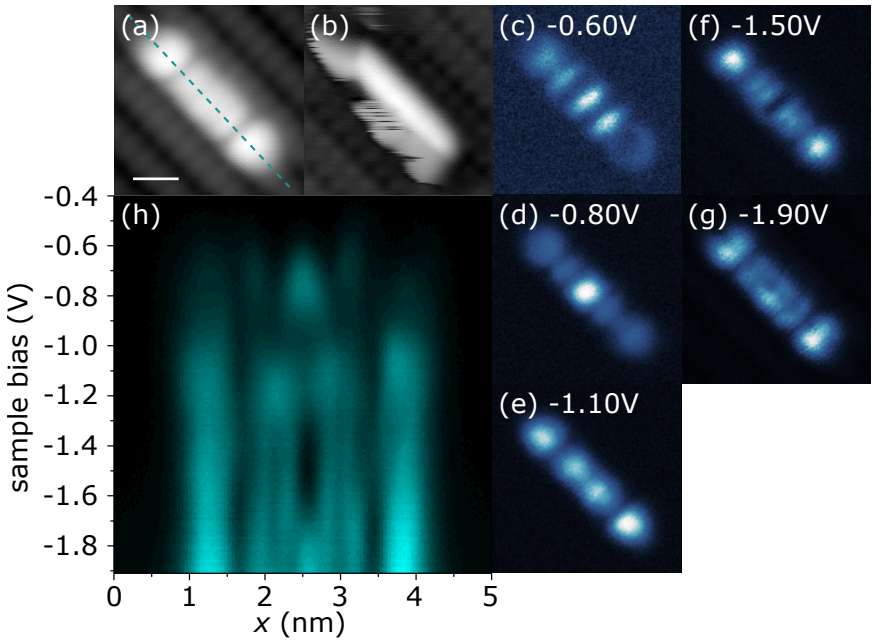

Figure 6.14: 7 DB chain on a 1050 °C sample. (a,b) Constant current images at –1.8 and 1.4 V, 50 pA. (c-g) Constant height dI/dV maps at constant voltages. (h) Constant height dI/dV linescans over the dotted line in (a). The tip height for dI/dV mapping was –1.8 V, 20 pA with 60 pm tip retraction over H-Si. The scale bar in (a) is 1 nm long and is the same scale for (a-g).

with respect to the equipotential line, possibly indicating buckling, although map (e) reveals no comparable asymmetry. At about –1.3 V the central two features split into two finer lines, also seen in map (f), which continue with only a little broadening at –1.6 V up to –1.7 V. Beyond this voltage, a new central feature emerges, which seems to merge with the inner two of the fine lines to form a total of five features, seen in map (g), before the maximum voltage –1.9 V. We remind the reader that scanning to larger voltages, though tempting, leads to destruction of the artificial molecule.

6.3 ANALYSIS OF 3 DB CHAINS

We see immediately that the filled state LDOS of DB chains do not resemble those 1 D particle in a box states predicted by the multiple interacting well model of Section 5.3. The single particle solutions are not sufficient.

We must also consider the perturbative effect of the tip, which bends bands locally and forces a tunnelling current originating from the bulk through the chain. In an attempt to tease out the myriad effects, we start by analyzing the negative differential resistance evident in 3 DB chains on a 1050 °C sample.

6.3.1 *NDR in 3 DB Chains*

On many DB chains, most often on 1050 °C samples, we observe NDR on the end atoms at near the same voltages as on isolated DBs. The clearest example is the 3 DB chain in Figure 6.4, where the two DBs on either end exhibit NDR from −1.0 V to −1.3 V, as shown in Figure 6.15. Furthermore, in $\mathrm{d}I/\mathrm{d}V$ maps, a bright ring is visible above each of them, much like the bright ring visible when scanning a single DB in the NDR regime (Fig. 4.4 (b)). We conclude that they each still have their two transition levels available inside the gap, their energetic position not modified very much. In contrast, the centre DB does not contribute any signal: it is 'dark', as opposed to the 'bright' DBs on either side.

The bright appearance of a DB hinges on the ability of the (0/−) level to be filled by the dopant band and pass current. A bright DB is fully occupied and thus negatively charged when probed by the tip. Clearly, the (0/−) transition level of the centre DB is inaccessible to be filled by the dopant band when the tip is above it. Either the (0/−) level or both it and the (+/0) levels of the centre DB have been raised in energy beyond the highest energy electrons of the dopant band. The former implies that the DB is neutral, the latter that it is positive.

We posit that this level raising is a result of other extra electrons on the chain, likely residing in one or both of the two DBs on each end. The Coulomb energy required to localize further electrons, this time

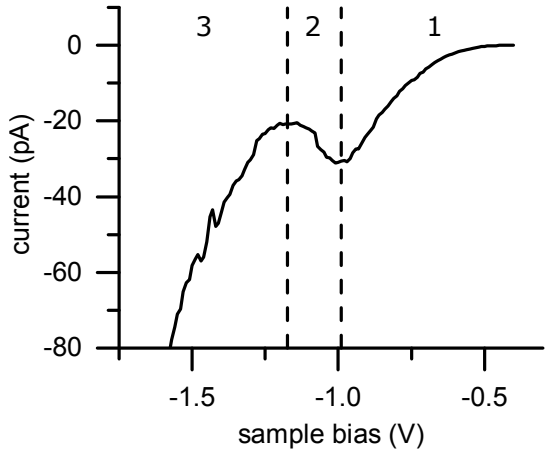

Figure 6.15: *I–V* curve taken over a bright DB of a 3 DB chain on a 1050 °C sample at a –60 pm tip offset from the initial tip height of –1.8 V and 20 pA set over H-Si. NDR is apparent in region 2.

on the middle DB, is beyond the capability of those available in the dopant band. We conclude that, when the tip is in proximity of the chain, the middle DB is either neutral or positive, and the two DBs on either side are negatively charged.

6.3.2 *Quantized Charge Model*

To explain more fully the results evident for a 3 DB chain and allow us to predict the charging behaviour of longer chains, we develop a simple model to determine how to populate a chain with charge for a given number of electrons and tip position, under the assumption that we have quantized charge. We will only allow a DB to hold units of the elementary charge, and will not consider fractional charge sharing between tunnel coupled DBs. This is a very large assumption, as previous experiments have shown significant charge sharing between DBs much farther apart [18, 19]. However, we will find that the results are satisfactory for a simple, intuitive, model that captures how the chains behave in the presence of the STM tip. The number of electrons and rules for populating will determine how a chain should look in experiment. We will find the self-consistent rules for smaller chains, allowing us to predict the behaviour of longer chains and compare

with experiment. We note that it is possible that the chains do not populate in this manner when unperturbed by a positive tip.

The tip creates a highly localized field at the surface. When above a certain DB, it is capable of lowering its surface levels slightly with respect to other DBs on the chain—the tip can 'drag' charge beneath it to a certain degree. Notably, this effect is not enough to make certain DBs conduct current, as we know is the case for the middle DB of the 3 DB chain.

We first assume a certain number of extra electrons, or negative DBs, on the chain, place them for every tip position, and then for that population decide how the chain should look in experiment, where a DB is bright if it is negative when the tip is above it. The DBs are highly tunnel-coupled and so electrons can move freely within the chain to lower the total energy. Our previous work estimates that tunnelling between coupled atoms occurs at roughly 10^{14} times per second [22].

Assuming one extra electron on the 3 DB chain, as in Figure 6.16 (a), we expect the tip is able to make every DB negative when it is imaging it. All three DBs should image bright. They do not.

Assuming two extra electrons on the 3 DB chain (Fig. 6.16 (b,c)), we must consider Coulomb repulsion in determining where the electrons reside. Intuitively, without a tip, one would expect the two electrons to reside at either end of the chain. When the tip is above each of the end atoms, we expect them to be negative, because both Coulomb repulsion and the tip field act to make it so. When the tip is above the central atom, the tip field tries to make the DB more negative, while Coulomb repulsion tries to keep it from becoming negative. From experiment, we know that the central DB cannot be negative, so we conclude that in this case Coulomb repulsion overcomes the tip field. We expect the 3 DB chain to image with the end DBs bright and the central dark. It does.

To extend our model to make predictions for longer chains, we postulate that Coulomb repulsion acts to keep negative DBs within the chain at least 7.68 Å apart, such that two can never be adjacent.

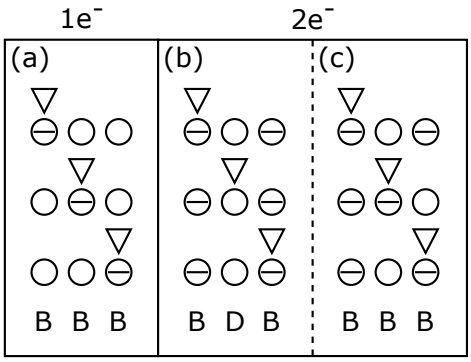

Figure 6.16: Populating a 3 DB chain for every tip position assuming one electron (a) and two electrons (b,c). DBs are represented by open circles; a negative DB has a minus sign within the circle. Tip position is represented by the downward triangles. Letters 'B' and 'D' signify if the DB images bright or dark when the tip is above it. For two electrons, either Coulomb repulsion overcomes the tip field effect (b), or the tip field overcomes Coulomb repulsion (c).

6.4 PREDICTING CHAIN OCCUPATION

We can now test our proposed rules, and attempt to predict the occupation and expected experimental results of different DB chain lengths, assuming a high surface dopant concentration, as on a 1050 °C sample.

1. Charge is quantized.
2. Negative DBs are not allowed to be adjacent.
3. The tip can move negative charge to the DB being imaged, so long as rule 2 is not violated.

6.4.1 *2 DB Chains*

Under these rules the predicted occupation of a 2 DB chain is trivial: only one extra electron is able to be held on one of the two DBs. The tip is able to make the DB it is currently probing negative. Therefore, both DBs image as bright. In experiment, we see that this is true, although we do not understand why the 2 DB chain on the 1050 °C

sample images as one bright spot over both DBs, while the 2 DB chain on the 1250 °C sample images as two distinct bright spots, one over each DB.

6.4.2 *4 DB Chains*

For one extra electron on the 4 DB chain, we expect all four DBs to be bright, as the tip is able to draw the electron along with it. For two extra electrons, we also expect all four DBs to be bright because the tip is able to force any DB it images to be negative without allowing any adjacent negative DBs, as seen in Figure 6.17 (b). Three or four electrons cannot be placed without allowing adjacent negative DBs.

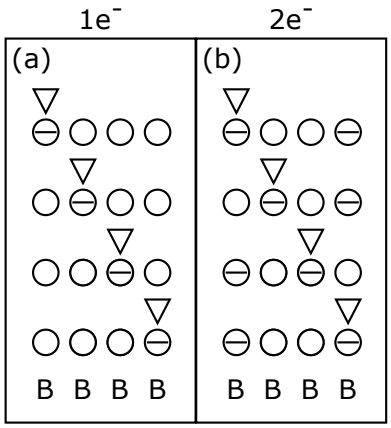

Figure 6.17: Populating a 4 DB chain for every tip position assuming one electron (a) or two electrons (b). DBs are represented by open circles; a negative DB has a minus sign within the circle. Tip position is represented by the downward triangles. Letters 'B' and 'D' signify if the DB images bright or dark when the tip is above it.

All experiments on 4 DB chains have shown that all four DBs image bright (Fig. 6.6, 6.7); there must be either one or two electrons on the chain. Upon considering all this, and given that the three DB chain has two extra electrons, it is clear that the 4 DB chain has two electrons.

6.4.3 *5 DB Chains*

For one or two extra electrons on a 5 DB chain, we expect all four DBs to be bright. In the case of 3 electrons, however, there are only three DBs that they can be placed into: the two on each end and the centre DB, which image brightly. When the tip is over those two DBs on either side of the central DB, it is unable to draw electrons into them without forcing adjacent negative DBs. The result is that those DBs appear dark in images. Four or five negative DBs are not allowed on the chain.

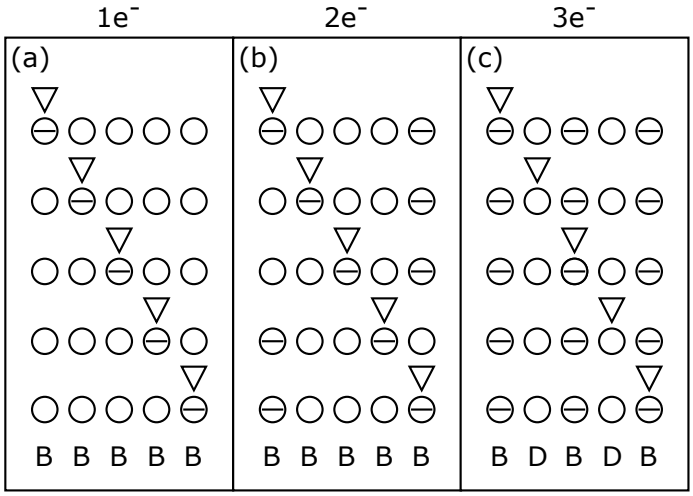

Figure 6.18: Populating a 5 DB chain for every tip position assuming one (a), two (b), and three electrons (c). DBs are represented by open circles; a negative DB has a minus sign within the circle. Tip position is represented by the downward triangles. Letters 'B' and 'D' signify if the DB images bright or dark when the tip is above it.

Type B 5 DB chains show that the two end DBs and the middle DB image brightly, the other two appear dark (Fig. 6.10, 6.11). The three bright DBs show three NDR rings that change into three spots as voltage is increased, much like the three DB chain which showed two circles and spots on the bright DBs. Therefore, we conclude that 5 DB chains of type B have three negative DBs.

Type A 5 DB chains show all five bright DBs (Fig. 6.8, 6.9). Here we must conclude that they have one or two negative DBs. We believe

that the difference between A type and B type is the surface dopant concentration near the chain, as will be discussed below.

6.4.4 *6 DB Chains*

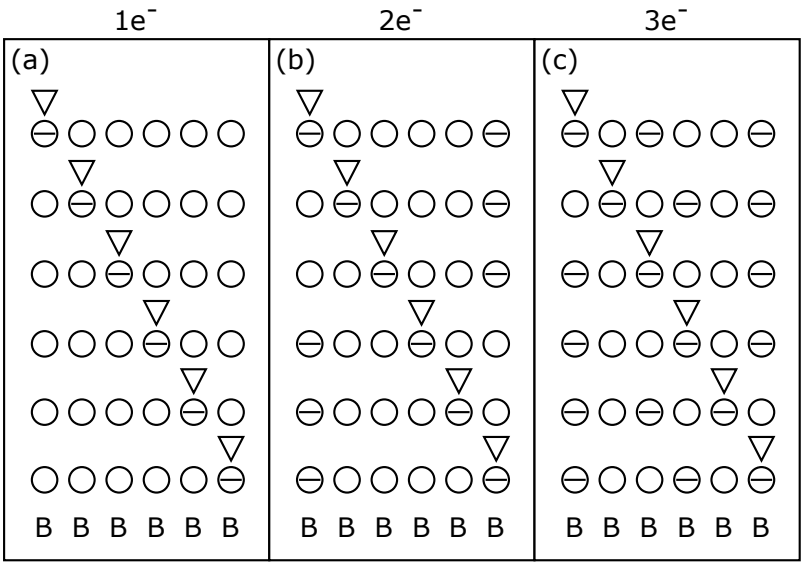

Figure 6.19: Populating a 6 DB chain for every tip position assuming one (a), two (b), and three electrons (c). DBs are represented by open circles; a negative DB has a minus sign within the circle. Tip position is represented by the downward triangles. Letters 'B' and 'D' signify if the DB images bright or dark when the tip is above it.

For one, two, and three extra electrons on the 6 DB chain, all DBs should image bright. Four or more electrons are not able to fit according to rule 2. In our experiments, all six DBs image bright (Fig. 6.13, 6.12). We conclude that they have 3 negative DBs, because previously we concluded that 5 DB chains had three.

6.4.5 *7 DB Chains*

For one, two, and three extra electrons, all seven DBs should image bright. For four extra electrons, a similar situation as with the 3 DB and 5 DB chains takes place, the DBs alternating from bright to dark as one goes along the chain, where the two end DBs are bright. Once

again the tip is unable to draw current through the dark DBs because it cannot make two adjacent DBs negative.

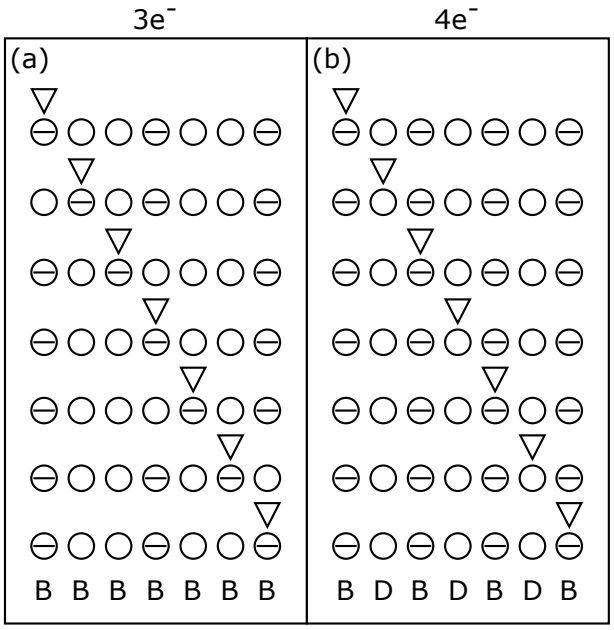

Figure 6.20: Populating a 7 DB chain for every tip position assuming three (a) and four electrons (b). DBs are represented by open circles; a negative DB has a minus sign within the circle. Tip position is represented by the downward triangles. Letters 'B' and 'D' signify if the DB images bright or dark when the tip is above it.

We have one example of a 7 DB chain, and it agrees with this population of electrons, exhibiting four bright DBs. The initial five bright features at –0.6 V we believe are in fact simply the intersection of the four rings we expect for four DBs within the NDR regime. At –1.10 V, the four DBs are bright as expected.

We find that for odd numbered DB chains we are able to get the maximum density packing of extra electrons that is possible: one negative DB for every two DBs.

6.5 EFFECTS OF THE BULK

For a low surface dopant concentration, as is the case on 1250 °C samples, it may be difficult for the chain to achieve its maximum number of negative DBs, because of the absence of the dopant band

in the near surface region. For a high surface dopant concentration, the dopant band extends to the surface, so there is a multitude of free charge carriers available to fill the chain to its brim, the case for 1050 °C samples and certain rare regions on 1250 °C samples.

The consequences of low surface dopant concentration are evident on the 1250 °C 3 DB chain of Figure 6.5 and the type A 5 DB chains of Figures 6.8 and 6.9. Each have less than the maximum number of extra electrons possible, so display three and five bright DBs respectively, instead of two and three were they fully charged.

Many chains, especially those on 1250 °C samples, show great variation of $\mathrm{d}I/\mathrm{d}V$ with voltage, variation seemingly unrelated to the properties of the DB itself, the 'regular' NDR effects. As discussed in Section 4.4.4, spectroscopy of single DBs on 1250 °C samples is characterized by tip field ionization and neutralization of randomly distributed single dopants nearby, modifying the conduction path and resulting in a near unique I-V curve for a given local area. This is no different for bright DBs of a chain. Because of their spatial proximity, each bright DB will experience nearly the same dopant network, so the entire chain will have near the same variation of $\mathrm{d}I/\mathrm{d}V$ as a function of voltage.

Negative differential resistance can be observed a result of this dopant network, not for those reasons discussed in Section 4.5. This is clear in those 3, 4, and 5 DB chains of Figures 6.5, 6.7, and 6.9 made by extending the initial 3 DB chain.

6.6 VARIATION BETWEEN BRIGHT DBS

There is clear experimental evidence that bright DBs are not equivalent on some chains. Our model is very rudimentary, useful only for determining which DBs are bright or dark, not considering any simple energetic differences between bright DBs as a function of specific charge arrangement, let alone the complexities that arise when allowing for fractional charge and interactions involving the spin of electrons within the chain.

The simplest variation to be noticed between bright DBs are the offsets in $\mathrm{d}I/\mathrm{d}V$ features sometimes found for different bright DBs probed along a chain. The most clear example is the 4 DB chain of Fig-

ure 6.7, where all four bright DBs show the same features in dI/dV linescans, a bright spot followed by two dark spots followed by another bright spot, but the sequence occurs at a slight offset in voltage between the DBs. We posit that the different local environmental and charge configuration for different probed DBs results in shifted energy levels and therefore shifts in spectroscopy.

More complicated are instances where dI/dV linescans reveal the single feature of a bright DB 'splitting' into two thin features, often merging back into one. We see this in the central bright DB of type B 5 DB chains (Fig. 6.10, 6.11) and the two central bright DBs of the 7 DB chain studied (Fig. 6.14). We posit that it is a similar effect as the bright ring seen when imaging a DB in the NDR regime: the DB is in a different charge state and thus images differently when the tip is directly over or slightly to the side of the DB. Our current model has no way to predict when a DB will show a ring, except for those rings seen in the NDR voltage regime.

Knowing that bright DBs can image as either 'ring-like' or 'spot-like', we can account for any complex patterns that emerge in dI/dV at a specific bias voltage as sums of different bright DBs imaging in either of these two modes. For example, the five bright spots at –2.0 V of the 6 DB chain in Figure 6.12 can be constructed by letting the two end DBs image as spots and the four inner DBs image as rings. The overlapping signal from the four rings forms the three bright central spots. It seems that the end DBs of any length of chain always image as spots with the exception of the NDR ring, and more inner bright DBs image as either rings or spots, depending on the bias voltage.

6.7 ELECTROSTATIC CONSIDERATIONS

Our experiments can only tell us which DBs are negative when the tip is above them; we cannot tell if dark DBs are positive or neutral. Positive charge will act to stabilize more negative charge on the chain. Here, we consider simple electrostatics of multiple point charges to determine the stability of various configurations. We will attempt to rationalize our requirement that two negative charges are not adjacent, and determine if dark DBs are likely neutral or positively charged.

It takes a certain amount of energy to localize an electrons on a DB. These are the charge transition levels discussed in Section 4.4.1. To place an electron on a positive DB, it must have energy $E^{+/0}$, 0.35 eV above the valence band edge. Similarly, to place an electron on a neutral DB, it needs energy $E^{0/-}$, 0.85 eV above the valence band edge [3]. The electrons are stably localized because their energies are within the bandgap of Si, 1.17 eV at 0 K. Were they greater than the gap, they would delocalize as they gain resonance with a crystal band.

Placing charges close to one another has energy associated with it. The work necessary to bring a single charge q_1, from infinitely far away to a distance $\mathbf{r}$ from another charge q_2 is given by

$$W = \frac{1}{4\pi\epsilon}\frac{q_1 q_2}{\mathbf{r}} \tag{20}$$

where ϵ is the permittivity of the surrounding material. As DBs reside on the surface, we use the average of the vacuum and silicon permittivity, $\epsilon = (\epsilon_0 + \epsilon_{Si})/2$ [36]. If there are multiple charges, then each pairwise energy must be summed to obtain the total work done on q_1 to localize it.

To place an electron on a DB in the presence of other charges, we must provide the energy associated with the charge transition level (+/0) or (0/−), along with this electrostatic contribution. We effectively shift the relevant charge transition level up by the energy of the electrostatic contribution of Equation 20. We reason that if the sum of energies is greater than the silicon bandgap, then the electron is unable to localize on the DB; it is dispersed in the conduction band.

For each charge configuration, we take the highest energy electron in each DB, and assuming all other charges are fixed, see if the energy required to place it exceeds the bandgap. If any electron on any DB exceeds the bandgap energy, we conclude that the given charge configuration is unstable and does not form in experiment.

To place an electron in a DB adjacent to a negative DB requires about 0.6 eV of electrostatic energy. Adding this to the 0.85 eV necessary to render an isolated DB negative results in a total energy of 1.45 eV, greater than the bandgap of silicon—this charge configuration is unstable.

6.7.1 *Charge of Dark DBs*

To explore the likely charge of a dark DB, we consider the 3 DB chain. We concluded two possible configurations: either the centre DB is neutral or positive while the DBs on either side are negative. We start by looking at the neutral case. Here, we must examine the extra electron on each of the two DBs on the end, rendering them negative, and the electron on the central DB, rendering it neutral.

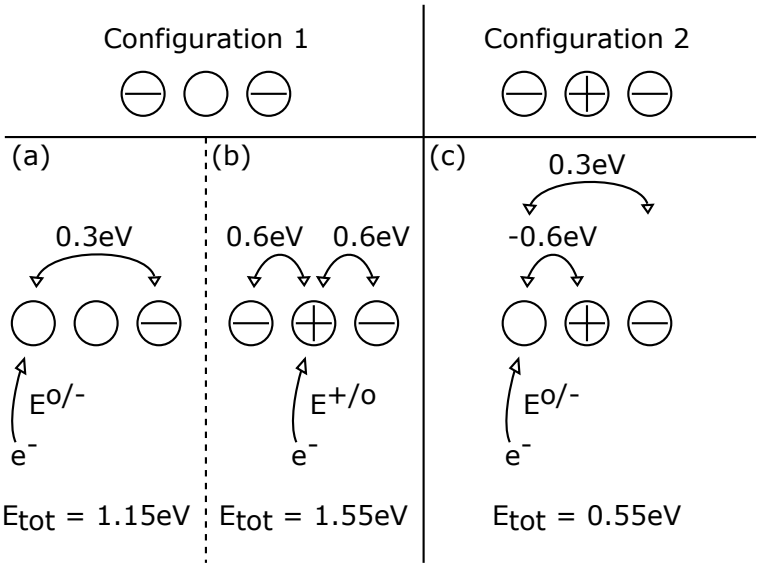

Figure 6.21: Energy required to place each electron for the neutral (a,b) and the positive (c) central DB configuration of the 3 DB chain. The electrostatic energy that each electron must overcome for each pairwise interaction is indicated by arrows. Open circles represent DBs, minus and plus signs represent DBs charged with −1 or +1 elementary charge. The electron, e^-, is added to the DB pointed to, with the relevant transition level energy indicated.

As in Figure 6.21 (a), the electrostatic energy required to place the extra electron on an end DB assuming the other is also negative is about 0.3 eV. Adding this to $E^{0/-}$ gives 1.15 eV, just below the bandgap energy. Placing the electron on the central DB, turning it neutral from positive, assuming the DBs on each end are negative, takes about 1.2 eV of electrostatic energy. Summing this and $E^{+/0}$ gives a total energy of 1.55 eV, much greater than the silicon bandgap (Fig. 6.21 (b)). We conclude that this charge configuration is unstable.

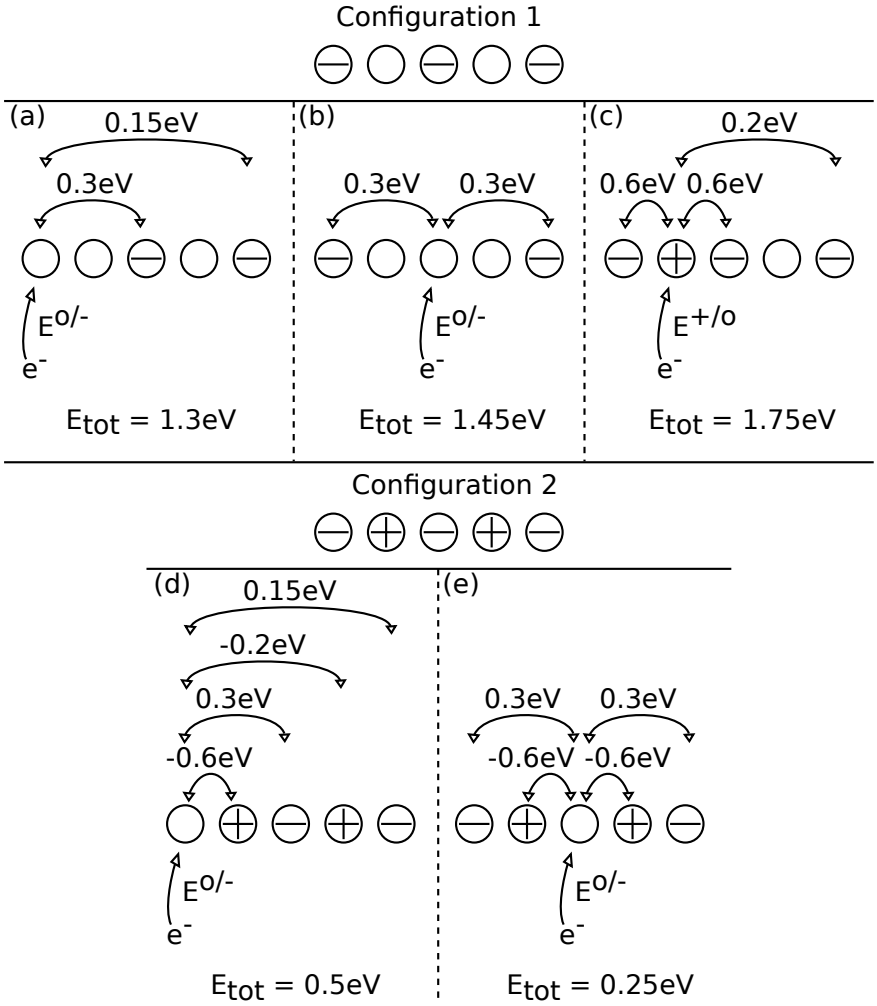

Figure 6.22: Energy required to place each electron for the neutral (a,b,c) and the positive (d,e) dark DB configuration of the 5 DB chain. The electrostatic energy that each electron must overcome for each pairwise interaction is indicated by arrows. Open circles represent DBs, minus and plus signs represent DBs charged with −1 or +1 elementary charge. The electron, e^-, is added to the DB pointed to, with the relevant transition level energy indicated.

The second possible configuration is two negative end DBs and a central positive DB (Fig. 6.21(c)). We must only consider the energy required to place an electron on one end DB, assuming the central DB is positive and the other end DB is negative. The electrostatic energy required is –0.3 eV, which when added to $E^{0/-}$ yields a final energy of 0.55 eV: this electron is within the bandgap. Therefore, this configuration is stable and can occur in experiment.

We examine the 5 DB chain using this model, as in Figure 6.22. We find, as with the 3 DB chain, that the only stable configuration that also matches experiment is the case where the bright DBs are negative and the dark DBs are positive.

For the three and the five DB case, this electrostatic argument seems to indicate that dark DBs are positive. For longer chains, there are likely positive DBs interspersed between and stabilizing the negative DBs, lowering the energy of constituent negative charge levels.

As the centre DB of a 3 DB chain is positive, we expect downward band bending in its vicinity. In filled state imaging, this would correspond to a reduction in conductance from the valence band—we should see the centre DB as less conductive than the surrounding silicon. Experimentally, we observe the centre DB as equally conductive (Fig. 6.4), implying that it is neutral. It is possible that the great conductance of the two bright DBs on either side 'drown out' any small signal from both the H-Si and the centre DB.

This electrostatic model ignores the essential quantum mechanical nature of the system, assuming point charges for wavefunctions and neglecting exchange interactions and charge sharing through tunnel-coupling, all likely to lower predicted energies. We note that if negative DBs are allowed to share charge and thus lower the total negative charge on a chain, then interspersed positive DBs may be unnecessary. Dark DBs could be neutral in this case.

6.8 EMPTY STATE APPEARANCE

In filled states, band bending acts to fill the chain 'to the brim' with electrons. This, as discussed, has the effect of rendering some DBs unable to pass current as the electrostatic energy necessary to fill the conducting levels is beyond that of the dopant band.

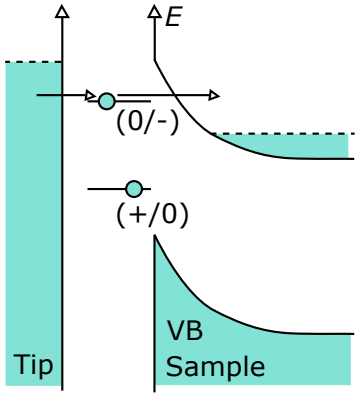

Figure 6.23: Band diagram depicting empty state imaging of DB chains. The charge transition levels of all the DBs on the chain are available to pass current from the tip to the bulk.

In empty states, band bending acts to push surface levels upward in energy, bringing filled DB levels on the chain above the Fermi level (Fig. 6.23). Thus, this extra charge leaks into the bulk, rendering the chain neutral or even positive. It has many empty levels available, with no Coulomb repulsion acting to keep electrons out.

When passing a tunnelling current into the chain, the tip injects electrons into chain DB levels, which leave the chain and pass into the bulk bands. The tip has available the great number of empty levels discussed above to inject electrons into, so it is able to pass a current easily for any position above the chain owing to the multitude of conduction pathways. Consistent with this expectation, we see the chains image brightly along their entire length.

6.9 DENSITY FUNCTIONAL THEORY & SPIN CONTAMINATION

To find precise energetics of electron occupation and spin orientation of DB chains in isolation, we must turn to more sophisticated, quantitative, modelling techniques. Density functional theory is the premier ab initio, numerical theory for quantum chemistry applications, capable of modelling relatively large systems of atoms and electrons with manageable computational time.

Density functional theory makes two major assumptions: the external potential acting on a particle is determined in part by the ground

state electron density $\rho(\mathbf{r})$ and the density with the lowest total energy represents the true ground-state. As entailed by the former, the potential V is formulated as a function of both the nuclear structure, $V_n(\mathbf{r})$, and the electron density, $V_e(\rho)$, making the potential a function of a function, or a functional [52].

An iterative method is used, where an initial guess for electron density is used to compute the potential, which is used to find a new, updated solution for the density. These steps are cycled until a self consistent solution is found, where the computed potential produces a set of wavefunctions and an electron density that match, to a chosen error, those of the previous iteration [53, 54].

Modelling DB chains has unique challenges associated with it as we enter into the theory blind to the exact charge state and spin configuration of the chain, the latter leading to the currently unresolved phenomenon known as spin contamination. By not restricting the spin configuration of the chain during the energy minimization in DFT, electronic spin configurations that cannot be physically concurrent are mixed, artificially reducing the energy below the true ground state [54]. Mixing is allowed by the approximate wavefunctions that are necessary for short computation times. As we are ignorant to the true ground state spin configuration, we cannot justify fixing it before computation, and to compute results for all possible configurations would take a prohibitive amount of time.

7

PERTURBING A 7 DB CHAIN

Up to this point we have only examined chains in isolation. Of great interest is how they behave when in proximity to other surface structures. To that end, we took the 7 DB chain of Figure 6.14 and explored the effects that a single DB and a bare dimer have when placed in proximity.

7.1 EXPERIMENTAL DETAILS AND MEASURED EFFECTS

After the 7 DB chain was patterned and fully characterized (Fig. 6.14), the STM tip was used to create a single DB near one end of the chain. It was placed on the same side of the same dimer row as the chain, with one intervening H atom between it and the last DB of the 7 DB chain. A diagram and a constant current image of the resulting structure are shown on the right side of Figure 7.1 (b). dI/dV linescans and maps across a wide range of voltages were taken on the region in its entirety, fully characterizing the chain and the single DB in proximity.

The single DB was turned into a bare dimer by desorbing the other H atom on its dimer. The structure is shown on the right side of Figure 7.1 (c) in a constant current image and a similar diagram. As before, dI/dV linescans and maps were taken of the entire structure.

In Figure 7.1 we present dI/dV linescans on the left and constant current images on the right. Looking at linescans, the unperturbed chain (Fig. 7.1 (a)) exhibits LDOS patterns described in Chapter 6 that are symmetric about the centre of the chain, at 2.25 nm, and begin in significant intensity at -0.6 V.

Once perturbed by the single DB (Fig. 7.1 (b)), the dI/dV patterns, or LDOS, of the chain changed dramatically, with little electronic structure identified in the unperturbed chain (Fig. 6.14) to be found in the perturbed chain. Some broad observations of the perturbed 7 DB chain LDOS can be made. State density begins with significant intensity at –0.9 V and is not symmetric about the centre of the chain. State density over the voltage range of the linescans appears greater on the

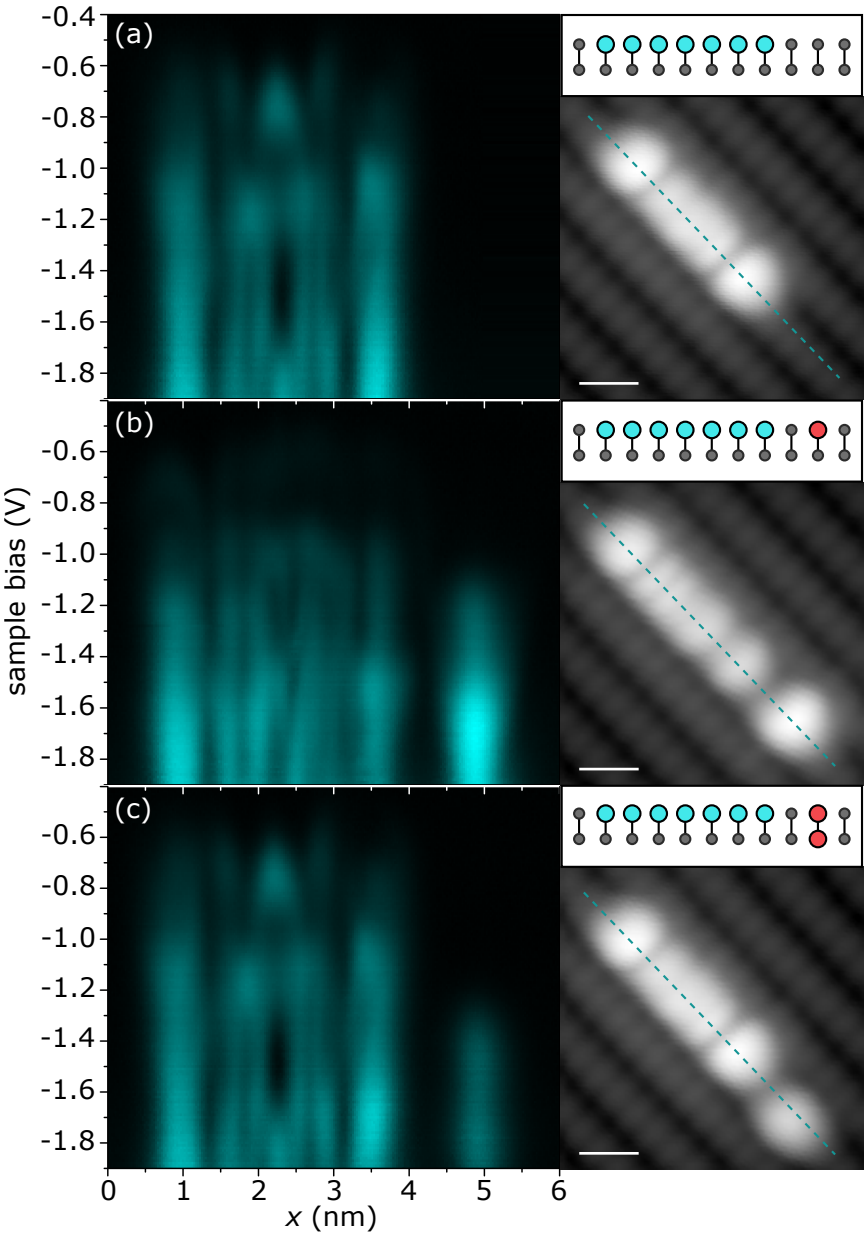

Figure 7.1: A 7 DB chain (a) controllably perturbed by a single DB (b) and a bare dimer (c). In (a-c) dI/dV linescans are on the left, taken over the dotted line on the constant current image at –1.8 V, 50 pA on the right. Above each image is a diagram of the structure. Vertical lines represent single dimers, small grey circles H atoms, and larger blue and red circles DBs of the chain and the perturbing feature. In linescans, state density of the 7 DB chain is found at 0.5–4 nm and that of the perturbing feature from 4.5–5.5 nm. Linescans were taken at a tip height of –1.8 V 20 pA with 60 pm tip retraction over H-Si; each scale bar is 1 nm long.

'left' side of the chain, the end furthest from the perturbing DB, than on the 'right'. This is also evident in the constant current image; the end of the chain on the left appears brighter than that on the right.

To our initial surprise, upon creating the bare dimer, the perturbative effects of the single DB disappear and the 7 DB chain takes on its original character. Its measured LDOS when in proximity to a bare dimer (Fig. 7.1 (c)) is nearly identical to that when it is totally isolated from any surface structure (Fig. 7.1 (a)). This effect is clearly seen in the difference map of Fig. 7.2 (b).

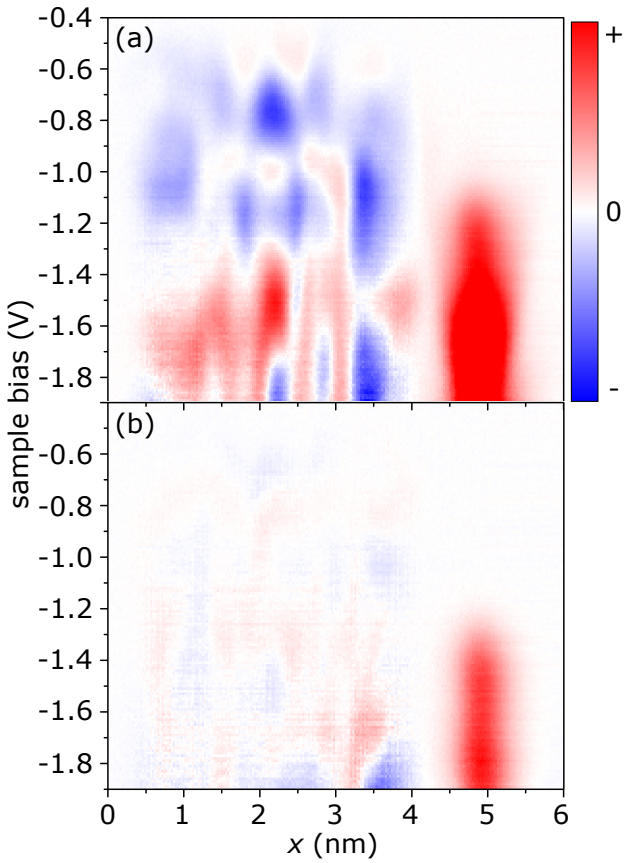

Figure 7.2: Difference maps demonstrating the electronic structure of the 7 DB chain in Figure 7.1 changing upon perturbation by a single DB (a), and a bare dimer (b), formed by subtracting the linescans of Figure 7.1 (a) from those of Figure 7.1 (b) and Figure 7.1 (c). Red corresponds to an increase in state density and blue to a reduction. State density associated with the 7 DB chain is found from 0.5 to 4 nm and that of the perturbing single DB or bare dimer from 4.5 to 5.5 nm.

We endeavour to understand the effect, or lack of effect, of a single DB and a bare dimer on a 7 DB chain when placed in proximity. The answer lies in the different electronic nature of the two: one can hold a localized charge and one cannot.

7.2 SINGLE DBS AS LOCALIZED CHARGES

A single DB, as discussed before, is a mid-gap state that can hold up to one extra electron. In filled states on a highly n-doped sample, as is the case in our experiment, it is usually negatively charged, so acts as a localized negative surface charge. The DB chain, so close to one, experiences a great electrostatic perturbation, lending a plausible explanation of our experimental results.

Figure 7.2 is a difference map constructing by subtracting the $\mathrm{d}I/\mathrm{d}V$ linescans of the unperturbed 7 DB chain (Fig. 7.1 (a)) from that of the chain perturbed by a single DB (Fig. 7.1 (b)). It shows where and at what energy electron density is diminished, in blue, and increased, in red, when the single DB is placed.

Looking at the $\mathrm{d}I/\mathrm{d}V$ linescans and the difference map of the two, we see that the action on the chain is to both shift electron state density upwards in voltage and to the side spatially, away from the local charge of the DB. Electron density between -0.6 and -0.9 V, which was apparent on the unperturbed chain, nearly disappears, and state density from -0.9 to -1.2 V is lower compared to the unperturbed chain. Higher than -1.2 V, the state density of the perturbed chain is greater than the unperturbed chain, except in regions adjacent to the perturbing DB.

LDOS maps become non-symmetric, with state density greater in regions of the chain farther away from the perturbing DB, seen also in its constant current images. The electrostatic effect of the local charge causes electrons to energetically favour regions of the chain farther away from it, distorting the observed molecular orbitals greatly. The difference map shows this as the right side of the chain is reduced in state density for all voltages and the left is increased for voltages above -1.3 V. These observations are consistent with our expectation that negative charges cause upward band bending, thus destabilizing nearby electronic energy levels.

7.3 BARE DIMERS AS LINKS TO THE BULK

As described before, in Chapter 4, when two DBs are created on a single dimer, they are separated by only 2.34 Å and so strongly couple to form a covalent bond. The bonding and antibonding orbitals are known as the π and π^* orbitals, whose energy splitting is a little over 1 eV [37, 38] from the initial mid-gap state of the single DB, each overlapping significantly with the valence and conduction bands respectively.

Any electron placed in the bare dimer, either in the π or the π^* orbital, is resonant with a crystal band. The initially localized electron will 'leak into' the delocalized crystal bands. No local charge means that there is no electrostatic perturbation on the 7 DB chain. It takes on its isolated character because electronically, it is isolated.

Because bare dimer states have density within the bandgap somewhat as well as within the valence and conduction bands, it is conceivable that they could act as a link to the bulk for other mid-gap states that are not quite resonant with either bulk band. They could thus act to couple certain atomic scale surface structures to bulk bands.

8

THE ANTINODE

In empty state constant current images of two DBs at a distance of one to three and occasionally four intervening H atoms, there is a bright spot between the two that does not correspond to any surface defect; it occurs over an H-Si region. The feature is evident if the DBs are on different sides of the same row, on different rows, or at any angle with respect to the dimer rows, seeming to be independent of the orientation of the intervening lattice. Images of the phenomenon are found in Figures 8.2 (b) and 8.3 (b). The feature, called 'the antinode' within our group, has been observed in an existing publication [4].

8.1 PREVIOUS EXPERIMENTS & MODELLING

The authors, in the number of examples they give, find that for two DBs the antinode is visible when scanning at higher voltages or lower setpoint currents, and invisible for lower voltages or higher setpoint currents. They claim that the antinode is an "excited state" caused by coupling between the two DBs. Producing an antinode experimentally for a number of structures, they focus on a particular structure, that with two DBs on the same side of the same dimer row with one intervening H atom. We patterned a similar structure; the relevant constant current image is in Figure 8.3 (b).

To model the structures, the authors construct a 1 D potential for which they numerically solve the 1 D Schrödinger equation, yielding a certain number of bound states at specific energies. Each DB is represented by a 1 D Pöschl-Teller potential well, as described in Section 5.1.

The two DB structure with one intervening H atom is formed by summing two wells with a 0.77 Å separation. We replicated their model and solved the 1 D Schrödinger equation numerically using a finite difference implementation, finding three bound states. Our solutions are shown in Figure 8.1, the only variation a slightly different energy for the highest energy state, –0.06 eV instead of –0.07 eV.

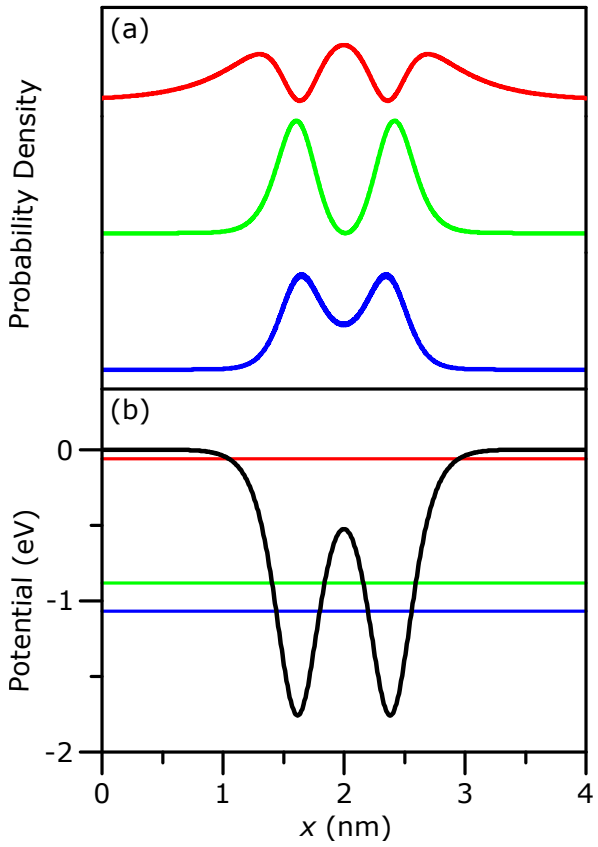

Figure 8.1: A replication of the model for two DBs with one intervening H atom given in [4] using a 1 D potential well constructed by summing two Pöschl-Teller potentials. (a) Probability density of the three bound states, with lower to higher energy states plotted from bottom to top. (b) Plot of the potential well, with horizontal lines at –1.07, –0.88, and –0.06 eV marking the energies of the three states.

Looking at the solutions, we see that the ground state for the single well has split into two levels, the lower energy one a symmetric 'bonding-like' state and the higher an antisymmetric 'antibonding-like' state. These two have probability density maximums approximately centred over each DB, with the symmetric attributed to filled state images and the antisymmetric to empty state images that do not show the antinode. The third state, however, has density at its maximum exactly between the two wells, along with two peaks on either side located slightly beyond the centres of each well. This is the eponymous excited state. Tunnelling through it would form a bright feature in constant current images between two DBs.

This model is consistent with their observations. At lower imaging voltages or higher setpoint currents only the two states with maximum density above the DBs are accessible for tunnelling: the antinode is not visible. A higher imaging voltage brings tip levels up and a lower setpoint current increases tip-sample separation, drops more voltage across the vacuum, and therefore reduces surface band bending. These both act to bring the excited state, which is higher energy than the 'regular states', into resonance with the tip level.

8.2 CHARACTERIZING THE ANTINODE

We decided to explore the antinode feature with $\mathrm{d}I/\mathrm{d}V$ mapping techniques, to try to learn more about its LDOS and precise energetic position with respect to the regular DB features that appear on either side. Our experiments focused on DB pairs on the same side of the same dimer row, studying three different separations: two intervening H atoms, one intervening H atom, and no intervening H atom, or a 2 DB chain.

We fully characterized one example for each of the three separations. They were patterned in the same region of the same 1050 °C sample; each should have a similar enough doping level between them to allow for some meaningful comparison. Following the same procedure as with DB chains, $\mathrm{d}I/\mathrm{d}V$ linescans and maps were taken in both filled and empty states.

8.2.1 *Two Intervening H Atoms*

Looking at Figure 8.2, the familiar empty state antinode is visible in the constant current image of (b). In empty state $\mathrm{d}I/\mathrm{d}V$ linescans, found in the upper panel of (g), its signal, located at 1.5 nm, extends from 0.7 to beyond the maximum voltage. The signals associated with each DB, at 0.75 and 2.25 nm, appear over much the same voltage, starting slightly earlier at 0.4 V. To find the onset of the two DBs, an examination of the constant height images (c,d), taken alongside $\mathrm{d}I/\mathrm{d}V$ maps, was necessary as the $\mathrm{d}I/\mathrm{d}V$ signal from the two DBs was too weak at these voltages to appear. The dark halo around each DB in (f) arises when looking at isolated DBs and is a consequence of

the DB changing charge states and thus bending the bands differently, as discussed in Section 4.4.2. The antinode is still visible between the two DBs, though partially obscured by the two halos.

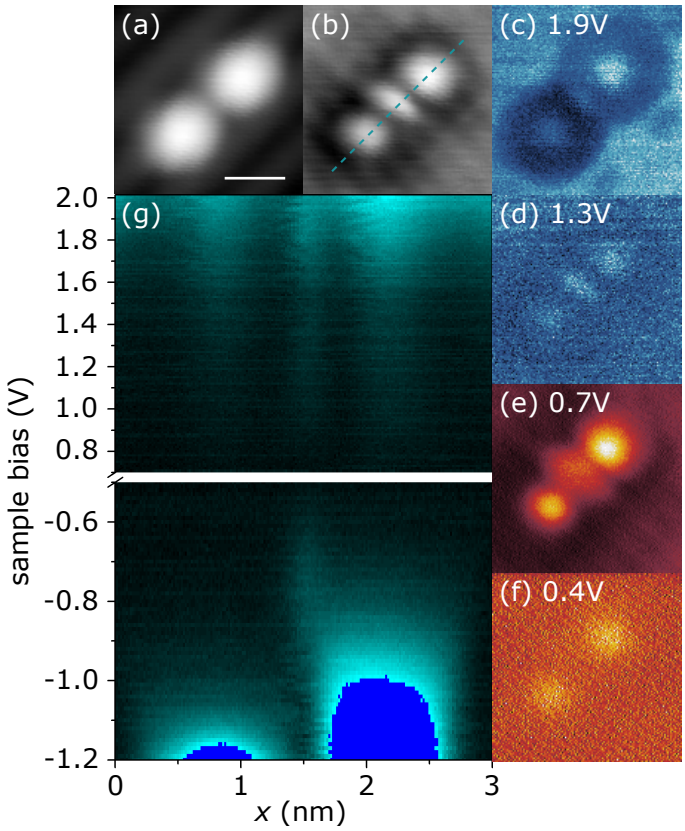

Figure 8.2: Two DBs with two intervening H atoms, showing an antinode on a 1050 °C sample. (a,b) Constant current images at –1.8 and 1.4 V, 50 pA. (c,d) Constant height dI/dV maps at constant voltages. (e,f) Constant height images. (g) Constant height dI/dV linescans over the dotted line in (b). The blue regions in (g) are clipped data values because they exceed the display range. The tip height for current images and dI/dV mapping was –1.8 V, 20 pA with 20 pm tip retraction over H-Si. The scale bar in (a) is 1 nm long and is the same scale for (a-f).

Filled state dI/dV linescans, found in the lower panel of (g), clearly show an antinode of sorts from –0.6 to –0.9 V. This kind of filled state antinode has not been observed in our group before. The DB states are inequivalent, likely because of differing local environments, such as closer proximity to a dopant. The 'left' DB has major onset at –1.1 V

and the 'right' at –0.9 V. Their high state density 'drowns out' the signal from the filled state antinode, rendering it invisible in constant current images. To resolve it necessitated clipping the signal from the two DBs, visible as the blue regions in the dI/dV linescans (g).

8.2.2 *One Intervening H Atom*

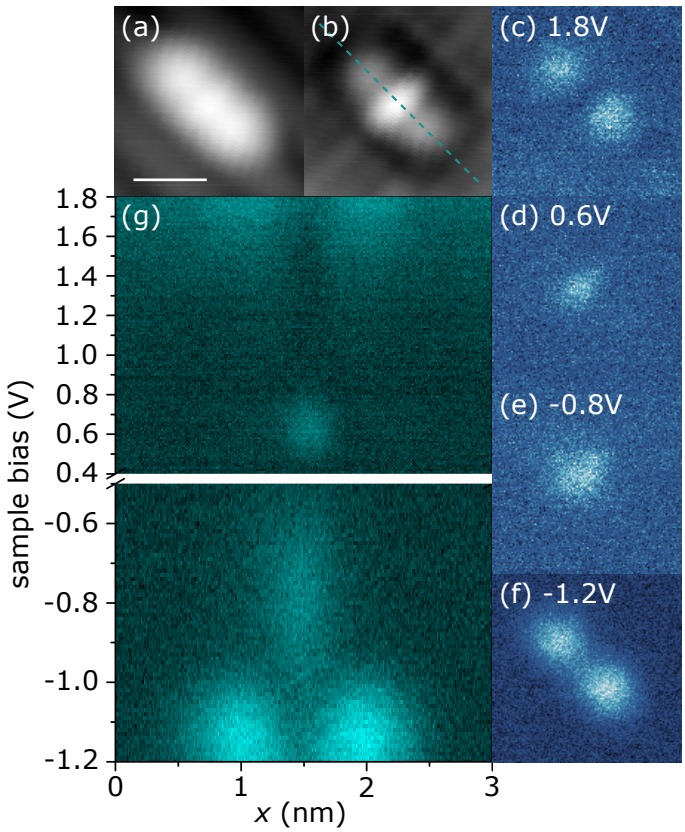

Figure 8.3: Two DBs with one intervening H atoms, showing an antinode on a 1050 °C sample. (a,b) Constant current images at –1.8 and 1.4 V, 50 pA. (c-f) Constant height dI/dV maps at constant voltages. (g) Constant height dI/dV linescans over the dotted line in (b). The tip height for dI/dV mapping was –1.8 V, 20 pA with 60 pm tip retraction over H-Si. The scale bar in (a) is 1 nm long and is the same scale for (a-f).

We examine Figure 8.3, and find that both filled and empty state constant current images (a,b) display an antinode. In the dI/dV empty state linescans of the upper panel of (g), we see that signals from the

antinode are separate in energy from the those of the DBs. The antinode, located at 1.5 nm, appears at voltages from 0.5 to 0.8 V. The DBs, found at 1 and 2 nm, appear at voltages of 1.3 V to the maximum voltage. These distinct distributions of state density are imaged in $\mathrm{d}I/\mathrm{d}V$ maps: that of the antinode in (c) and the DBs in (d), showing one and two spots respectively. This separation in energy between the antinode and the DBs features is in contrast with our observations in the case of two intervening H atoms.

The filled state antinode appears at voltages from –0.6 to –1.0 V in the filled state linescans of the lower panel of (g), separate in energy from the signal of the DBs whose onset is –1.0 V. $\mathrm{d}I/\mathrm{d}V$ maps of these two states (e,f) reinforce their separate nature, showing one and two spots respectively. This filled state antinode occurs at nearly the same voltages as in the case of two intervening H atoms.

This structure is of particular interest because it is a replica of one found in the previous publication mentioned earlier [4] with a particularly detailed characterization and theoretical treatment outlined in Section 8.1—a prime candidate for comparison.

8.3 COMPARISON WITH PREVIOUS WORK

The ambient temperature and silicon doping level are different between our experiments and those of the previous publication. We operate at 4.5 K necessitating degenerately doped silicon. Our wafers are n-type, As-doped, with a resistivity of 0.003 to 0.004 Ω·cm. We flashed to 1050 °C , leaving an intact donor band to the surface.

In contrast, the authors of the previous work operated at 77 K and used n-type, Sb-doped, silicon with a resistivity of 0.05 to 0.01 Ω·cm of much lower doping concentration. Furthermore, their silicon have thermal carriers in the conduction band. Their flashing temperature of 1200 °C likely removes dopants in the near surface region, similar to 1250 °C flashed samples (Sec. 4.1). Despite the differences in experimental conditions, we compare the recent results with those of the past to gauge their divergence and test the theoretical treatment, which does not take into account bulk doping effects.

In the case of two DBs separated by two H atoms, we find a marginal agreement with the previous publication: current from only the two

DBs begins at a lower voltage than current from the antinode. However, we find that the two relevant onsets occur at much lower voltages, –0.4 and –0.7 V instead of –1.5 and –1.9 V. This 1 V discrepancy seems too great to be explained by the different band bending produced by different doping and tip-sample separation, where our separation is smaller. We observe that for this DB separation, state density through the antinode occurs for a wide range of voltages concurrent with state density associated with the two DBs, from its appearance at –0.7 V up to the maximum voltage probed. This seems contrary to the proposal that the antinode and the two DB features are different states in the same system: they should not appear at the same voltages. Finally, we observe an antinode in filled states, a feature not observed or predicted in the previous work.

The structure consisting of two DBs separated by a single H atom is of particular interest because of its great experimental and theoretical elucidation previously. The three states calculated consisted of a symmetric and an antisymmetric state with maximum density centred over the centre of the DBs and a third, at higher energy, with maximum state density between the two DBs and two smaller maxima on either side. The lower energy two were attributed to the filled and empty state images of the two DBs, the third to the antinode, seen at higher energies as expected. In our experiments, we observe state density associated with the antinode at lower energy than that associated with the two DBs. This is totally contrary to the model, where the antinode should be at higher energy. Differences in band bending can account for a shift in observed voltages, but not a reversal as we observe. To cast further doubt, our LDOS map of the antinode only includes a single feature, lacking the two lower intensity peaks predicted in the model. We observe a filled state antinode here as well, again not touched on by the previous authors.

Our experimental results hold little to no correspondence with those of the previous authors; their model proves inadequate for us as well. Unfortunately, we have not the volume of experimental data necessary to describe the typical behaviour of the antinode on our samples or for different doping levels and temperature. Were that the case, we could perhaps offer a different explanation for its appearance, as the current view is unable to capture the behaviour of the few examples we give here. Considering our contrary observations to

those previously, it seems likely that properties of the antinode vary greatly as a function of doping level and specific local environment.

9

CONCLUSIONS & FUTURE WORK

The experimental results of this work have been collated and elucidated. What remains is to discuss their significance, those gaps in knowledge yet to fill, and what future possibilities exist.

9.1 SUMMARY OF MAJOR RESULTS

We begin with a brief overview of the structures patterned, the experiments performed, and any interpretations formulated.

9.1.1 *DB Chains*

DB chains, linear arrangements of DBs along a dimer row in the closest spacing allowed by the lattice, heretofore unstudied in our group, were patterned of length from two to seven DBs, using an automated technique that controllably removed each DB one at a time (Sec. 6.1). To characterize the chains, we employed a combination of constant current STM imaging (Sec. 6.2.1) and $\mathrm{d}I/\mathrm{d}V$ mapping techniques (Sec. 3.6.2, 6.2.2), from which their complex electronic structure was recovered (Sec. 6.2.3–6.2.9).

The most salient feature of DB chains in filled state imaging is the emergence of 'dark' DBs, DBs that do not conduct significant tunnelling current when the tip is overhead, on chains of odd numbered length. We found that dark DBs, when evident, are interspersed with 'bright' DBs, those that do conduct significant tunnelling current and exhibit the same negative differential resistance effects we observe on isolated DBs (Sec. 4.5). Our current understanding is that on odd length chains a maximal configuration of negative DBs—the bright DBs—are able to exist, their Coulomb repulsion great enough render the charge transition levels of the intervening DBs—the dark DBs—inaccessible to be filled by the dopant band and unable to pass current. Even length chains seem to not display dark DBs, as the tip field

is able to draw charge beneath it, and the incredible tunnel-coupling of DBs on the chain allows them to reconfigure as the tip moves, ensuring a bright DB wherever the tip moves; this reconfiguration is impossible in odd chains because there is not enough 'room'.

9.1.2 *Perturbing a 7 DB Chain*

In Chapter 7, we perturbed a 7 DB chain with a single DB and a bare dimer at a distance of 7.68 Å from the end of the chain, such that there was one intervening H atom between the perturbing feature and the end of the chain. Upon addition of the single DB, state density along the chain was no longer symmetric about its centre, instead shifting such that less state density was present near the perturbing DB and more was present far from it. State density was also shifted to higher negative voltages.

When the single DB was turned into a bare dimer, the electrostatic perturbation was completely reversed, and the 7 DB chain took on its isolated character. We concluded that the bare dimer is unable to support localized charge.

9.1.3 *The Antinode*

In a previous publication, it was argued that the bright feature between two DBs, known as the antinode within our group, was the result of a higher energy "excited state" formed through coupling of the two DB wells. We replicated their structures (Sec. 8.2.1, 8.2.2), and using dI/dV mapping, observed the antinode-like state at lower energy than the regular DB-like states, an observation at odds with the hypothesis of a higher energy excited state. We further showed evidence for a filled state antinode, a feature not seen before in the literature.

9.2 UNEXPLAINED PHENOMENA

We have measured the electronic structure of DB chains, with energetic and spatial precision not yet seen in the literature, and proven that the energy of DB levels on the chain, and therefore their acces-

sibility to tunnelling, depend on the occupation of other DBs on the chain. We have explained the emergence of dark DBs.

There still remain unexplained phenomena in our multitude of experimental data (Sec. 6.2.3–6.2.9). Interior bright DBs seem to split and show a bright ring, not associated with NDR rings. Chains on 1250 °C flashed samples do not seem to follow our populating rules, likely a consequence of the totally unknown dopant network. Bright DBs often show an offset in energy that is currently unaccounted for.

We have not been able to state exactly how much charge resides on a given chain, or a given DB on a chain. We only know that bright DBs are negative and dark DBs are either negative or positive. Tunnel coupling and the subsequent charge sharing between the DBs make this question very difficult to answer with simple models like those presented here. We are also ignorant to how much the tip field affects the charge state of the chain. It is possible that when isolated it takes on a much different charge configuration.

Lastly, the lattice distortion caused by DB chains is unknown at this moment. Previous literature [23] and our filled state images of 3 DB chains indicate that there is significant rearrangement of Si atoms beneath the chain. DFT or other complex computational methods are necessary to answer this and the other questions listed above.

9.3 FUTURE EXPERIMENTS

It has been observed in our group that filled state spectroscopy on a DB shifts if a second DB is placed on the order of 10 nm away. At this distance the DBs are not tunnel coupled but still experience electrostatic effects from the other. The shift, we believe, is caused by the electric field of the charge localized on the second DB. By turning the second single DB into part of a 2 DB chain, then a 3 DB chain, and so on and so forth, the shifts in spectroscopy of the first single DB for each chain length will tell us how much total charge exists on each chain length. For example, if a 3 DB chain has a total charge of 1 e, then the spectroscopy of the first single DB will be the same as for the single second DB, before it was turned into the 3 DB chain. If it contains 2 e, then the spectroscopy of the single DB will change when the single second DB is turned into a 3 DB chain.

Non-contact atomic force microscopy, a technique capable of sub-atomically resolving surfaces at zero bias, can examine DB chains without introducing the perturbative effect of a tip field and a tunnelling current. Not only will it be able to clarify the exact lattice shifts present, but with Kelvin probe force microscopy [55], it may be able to find the precise charge distribution of DBs in the chain and energies of transitions thereof [56].

Understanding how chains react to perturbation is essential if we wish to employ them as functional elements in atomic devices. To that end, experiments could be easily conducted exploring the distant dependent perturbative effects on a chain of single DBs or other chains in proximity.

Further, one could explore 2 D patterns of close coupled DBs. The geometric arrangements possible with this extra degree of freedom are staggering, and would allow the true engineering of structures with desired charging configurations and interactions between those thereof. These kind of 2 D experiments may only be possible with the hydrogen terminated Si(111) surface, where dimers do not form and so spacing between DBs of 3.84 Å, as in DB chains, is possible for 2 D structures.

9.4 CONSEQUENCES & FAR-REACHING POSSIBILITIES

We have demonstrated the controllable placement of multiple Å-size quantum dots at Å-scale spacing. We have shown that they have clear rigid charging configurations that can be controlled through electrostatic perturbation.

We can imagine, after a plethora of experimental and theoretical elucidation, the commonplace engineering of close-spaced quantum dot structures, like those shown here, with well understood charging configurations. The further design of their interaction with similar structures, forming classical switches and logic gates, and the ability to control and read from certain elements with external electric fields would allow for computation. One such proposal has been the QCA architecture, but many architectural possibilities exist; we must simply find the one most suited for our physical system. Beyond classical computation, we could employ lines or other structures of close-

spaced DB quantum dots to couple surface qubits to one another, allowing for atomic-scale quantum computation.

Whatever will be, this work opens more doors than it closes. We are assured that its agnate revelations will have great scientific and technological implications in the time to come.

BIBLIOGRAPHY

[1] J. A. Wood, M. Rashidi, M. Koleini, J. L. Pitters, and R. A. Wolkow. *Multiple Silicon Atom Artificial Molecules*. 2016. eprint: arXiv:1607.06050.

[2] M. Rashidi, M. Taucer, I. Ozfidan, E. Lloyd, H. Labidi, J. L. Pitters, J. Maciejko, and R. A. Wolkow. *Time-Resolved Imaging of Negative Differential Resistance on the Atomic Scale*. 2016. eprint: arXiv:1608.06344.

[3] M. Taucer, L. Livadaru, P. G. Piva, R. Achal, H. Labidi, J. L. Pitters, and R. A. Wolkow. "Single-Electron Dynamics of an Atomic Silicon Quantum Dot on the H-Si(100)-(2×1) Surface." In: *Phys. Rev. Lett.* 112 (25 June 2014), p. 256801. DOI: 10.1103/PhysRevLett.112.256801. URL: http://link.aps.org/doi/10.1103/PhysRevLett.112.256801.

[4] S. R. Schofield, P. Studer, C. F. Hirjibehedin, N. J. Curson, G. Aeppli, and D. R. Bowler. "Quantum engineering at the silicon surface using dangling bonds." In: *Nature Communications* 4.1649 (2013).

[5] G. Binnig, H. Rohrer, C. Gerber, and E. Weibel. "Tunneling through a controllable vacuum gap." In: *Applied Physics Letters* 40.2 (1982), pp. 178–180. DOI: http://dx.doi.org/10.1063/1.92999. URL: http://scitation.aip.org/content/aip/journal/apl/40/2/10.1063/1.92999.

[6] G. Binnig, H. Rohrer, C. Gerber, and E. Weibel. "7×7 Reconstruction on Si(111) Resolved in Real Space." In: *Phys. Rev. Lett.* 50 (2 Jan. 1983), pp. 120–123. DOI: 10.1103/PhysRevLett.50.120. URL: http://link.aps.org/doi/10.1103/PhysRevLett.50.120.

[7] M. Crommie, C. Lutz, D. Eigler, and E. Heller. "Quantum corrals." In: *Physica D: Nonlinear Phenomena* 83.1 (1995), pp. 98–108. ISSN: 0167-2789. DOI: http://dx.doi.org/10.1016/0167-2789(94)00254-N.

[8] J. Repp, G. Meyer, S. M. Stojkovi ć, A. Gourdon, and C. Joachim. "Molecules on Insulating Films: Scanning-Tunneling Microscopy Imaging of Individual Molecular Orbitals." In: *Phys. Rev. Lett.* 94 (2 Jan. 2005), p. 026803. DOI: 10.1103/PhysRevLett.94.026803. URL: http://link.aps.org/doi/10.1103/PhysRevLett.94.026803.

[9] J. Tersoff and D. R. Hamann. "Theory of the scanning tunneling microscope." In: *Phys. Rev. B* 31 (2 Jan. 1985), pp. 805–813. DOI: 10.1103/PhysRevB.31.805. URL: http://link.aps.org/doi/10.1103/PhysRevB.31.805.

[10] A. D. Gottlieb and L. Wesoloski. "Bardeen's tunnelling theory as applied to scanning tunnelling microscopy: a technical guide to the traditional interpretation." In: *Nanotechnology* 17.8 (2006), R57. URL: http://stacks.iop.org/0957-4484/17/i=8/a=R01.

[11] N. Nilius, T. M. Wallis, and W. Ho. "Development of One-Dimensional Band Structure in Artificial Gold Chains." In: *Science* 297.5588 (2002), pp. 1853–1856. ISSN: 0036–8075. DOI: 10.1126/science.1075242. eprint: http://science.sciencemag.org/content/297/5588/1853.full.pdf. URL: http://science.sciencemag.org/content/297/5588/1853.

[12] S. Fölsch, P. Hyldgaard, R. Koch, and K. H. Ploog. "Quantum Confinement in Monatomic Cu Chains on Cu(111)." In: *Phys. Rev. Lett.* 92 (5 Feb. 2004), p. 056803. DOI: 10.1103/PhysRevLett.92.056803.

[13] J. Lagoute, X. Liu, and S. Fölsch. "Electronic properties of straight, kinked, and branched CuCu(111) quantum wires: A low-temperature scanning tunneling microscopy and spectroscopy study." In: *Phys. Rev. B* 74 (12 Sept. 2006), p. 125410. DOI: 10.1103/PhysRevB.74.125410. URL: http://link.aps.org/doi/10.1103/PhysRevB.74.125410.

[14] B. Schuler, M. Persson, S. Paavilainen, N. Pavliček, L. Gross, G. Meyer, and J. Repp. "Effect of electron-phonon interaction on the formation of one-dimensional electronic states in coupled Cl vacancies." In: *Phys. Rev. B* 91 (23 June 2015), p. 235443. DOI: 10.1103/PhysRevB.91.235443. URL: http://link.aps.org/doi/10.1103/PhysRevB.91.235443.

[15] K. Seufert, W. Auwärter, F. J. García de Abajo, D. Ecija, S. Vijayaraghavan, S. Joshi, and J. V. Barth. "Controlled Interaction of Surface Quantum-Well Electronic States." In: *Nano Letters* 13.12 (2013), pp. 6130–6135. DOI: 10.1021/nl403459m. eprint: http://dx.doi.org/10.1021/nl403459m. URL: http://dx.doi.org/10.1021/nl403459m.

[16] L. Livadaru, P. Xue, Z. Shaterzadeh-Yazdi, G. A. DiLabio, J. Mutus, J. L. Pitters, B. C. Sanders, and R. A. Wolkow. "Dangling-bond charge qubit on a silicon surface." In: *New Journal of Physics* 12.8 (2010), p. 083018. URL: http://stacks.iop.org/1367-2630/12/i=8/a=083018.

[17] M. B. Haider, J. L. Pitters, G. A. DiLabio, L. Livadaru, J. Y. Mutus, and R. A. Wolkow. *Controlled Coupling and Occupation of Silicon Atomic Quantum Dots*. 2008. eprint: arXiv:0807.0609.

[18] M. B. Haider, J. L. Pitters, G. A. DiLabio, L. Livadaru, J. Y. Mutus, and R. A. Wolkow. "Controlled Coupling and Occupation of Silicon Atomic Quantum Dots at Room Temperature." In: *Phys. Rev. Lett.* 102 (4 Jan. 2009), p. 046805. DOI: 10.1103/PhysRevLett.102.046805. URL: http://link.aps.org/doi/10.1103/PhysRevLett.102.046805.

[19] J. L. Pitters, L. Livadaru, M. B. Haider, and R. A. Wolkow. "Tunnel coupled dangling bond structures on hydrogen terminated silicon surfaces." In: *The Journal of Chemical Physics* 134.6, 064712 (2011). DOI: http://dx.doi.org/10.1063/1.3514896. URL: http://scitation.aip.org/content/aip/journal/jcp/134/6/10.1063/1.3514896.

[20] C. S. Lent, P. D. Tougaw, W. Porod, and G. H. Bernstein. "Quantum cellular automata." In: *Nanotechnology* 4.1 (1993), p. 49.

[21] L. Livadaru, J. Pitters, M. Taucer, and R. Wolkow. "Understanding Charge Dynamics in Silicon Dangling Bond Structures for Nanoscale Devices." In: *Nanotech 2012 Vol. 2*. Ed. by NSTI. CRC Press, 2012. Chap. 1, pp. 35–37.

[22] L. Livadaru, P. Xue, Z. Shaterzadeh-Yazdi, G. A. DiLabio, J. Mutus, J. L. Pitters, B. C. Sanders, and R. A. Wolkow. "Dangling-bond charge qubit on a silicon surface." In: *New Journal of Physics*

12.8 (2010), p. 083018. URL: http://stacks.iop.org/1367-2630/12/i=8/a=083018.

[23] T. Hitosugi, S. Heike, T. Onogi, T. Hashizume, S. Watanabe, Z.-Q. Li, K. Ohno, Y. Kawazoe, T. Hasegawa, and K. Kitazawa. "Jahn-Teller Distortion in Dangling-Bond Linear Chains Fabricated on a Hydrogen-Terminated Si(100)- 2×1 Surface." In: *Phys. Rev. Lett.* 82 (20 May 1999), pp. 4034–4037. DOI: 10.1103/PhysRevLett.82.4034. URL: http://link.aps.org/doi/10.1103/PhysRevLett.82.4034.

[24] B. Naydenov and J. J. Boland. "Engineering the electronic structure of surface dangling bond nanowires of different size and dimensionality." In: *Nanotechnology* 24.27 (2013), p. 275202. URL: http://stacks.iop.org/0957-4484/24/i=27/a=275202.

[25] J. Bardeen. "Tunnelling from a Many-Particle Point of View." In: *Phys. Rev. Lett.* 6 (2 Jan. 1961), pp. 57–59. DOI: 10.1103/PhysRevLett.6.57. URL: http://link.aps.org/doi/10.1103/PhysRevLett.6.57.

[26] M. Hablanian. *High-Vacuum Technology: A Practical Guide, Second Edition*. Mechanical Engineering. Taylor & Francis, 1997. ISBN: 9780824798345. URL: https://books.google.ca/books?id=5L8uIAFm4SoC.

[27] O. N. GmbH. *LT STM User's Guide*. Oxford Instruments, 2013.

[28] A. I. Oliva, A. Romero G., J. L. Peña, E. Anguiano, and M. Aguilar. "Electrochemical preparation of tungsten tips for a scanning tunneling microscope." In: *Review of Scientific Instruments* 67.5 (1996), pp. 1917–1921. DOI: http://dx.doi.org/10.1063/1.1146996. URL: http://scitation.aip.org/content/aip/journal/rsi/67/5/10.1063/1.1146996.

[29] E. Müller and T. Tsong. *Field ion microscopy: principles and applications*. American Elsevier Pub. Co., 1969. URL: https://books.google.ca/books?id=GxG2AAAAIAAJ.

[30] M. Rezeq, J. Pitters, and R. Wolkow. "Tungsten nanotip fabrication by spatially controlled field-assisted reaction with nitrogen." In: *The Journal of Chemical Physics* 124.20, 204716 (2006). DOI: http://dx.doi.org/10.1063/1.2198536. URL: http:

//scitation.aip.org/content/aip/journal/jcp/124/20/10.1063/1.2198536.

[31] J. L. Pitters, R. Urban, and R. A. Wolkow. "Creation and recovery of a W(111) single atom gas field ion source." In: *The Journal of Chemical Physics* 136.15, 154704 (2012). DOI: http://dx.doi.org/10.1063/1.3702209. URL: http://scitation.aip.org/content/aip/journal/jcp/136/15/10.1063/1.3702209.

[32] K. Hata, T. Kimura, S. Ozawa, and H. Shigekawa. "How to fabricate a defect free Si(001) surface." In: *Journal of Vacuum Science & Technology A* 18.4 (2000), pp. 1933–1936. DOI: http://dx.doi.org/10.1116/1.582482. URL: http://scitation.aip.org/content/avs/journal/jvsta/18/4/10.1116/1.582482.

[33] J. L. Pitters, P. G. Piva, and R. A. Wolkow. "Dopant depletion in the near surface region of thermally prepared silicon (100) in UHV." In: *Journal of Vacuum Science & Technology B* 30.2, 021806 (2012). DOI: http://dx.doi.org/10.1116/1.3694010. URL: http://scitation.aip.org/content/avs/journal/jvstb/30/2/10.1116/1.3694010.

[34] C. C. Cheng and J. T. Yates. "H-induced surface restructuring on Si(100): Formation of higher hydrides." In: *Phys. Rev. B* 43 (5 Feb. 1991), pp. 4041–4045. DOI: 10.1103/PhysRevB.43.4041. URL: http://link.aps.org/doi/10.1103/PhysRevB.43.4041.

[35] Y. J. Chabal and K. Raghavachari. "New Ordered Structure for the H-Saturated Si(100) Surface: The (3x1) Phase." In: *Phys. Rev. Lett.* 54 (10 Mar. 1985), pp. 1055–1058. DOI: 10.1103/PhysRevLett.54.1055. URL: http://link.aps.org/doi/10.1103/PhysRevLett.54.1055.

[36] L. Livadaru, J. Pitters, M. Taucer, and R. A. Wolkow. "Theory of nonequilibrium single-electron dynamics in STM imaging of dangling bonds on a hydrogenated silicon surface." In: *Phys. Rev. B* 84 (20 Nov. 2011), p. 205416. DOI: 10.1103/PhysRevB.84.205416. URL: http://link.aps.org/doi/10.1103/PhysRevB.84.205416.

[37] D. Chen and J. J. Boland. "Chemisorption-induced disruption of surface electronic structure: Hydrogen adsorption on the Si(100)-2x1 surface." In: *Phys. Rev. B* 65 (16 Apr. 2002), p. 165336. DOI:

10.1103/PhysRevB.65.165336. URL: http://link.aps.org/doi/10.1103/PhysRevB.65.165336.

[38] A. Bellec, D. Riedel, G. Dujardin, O. Boudrioua, L. Chaput, L. Stauffer, and P. Sonnet. "Electronic properties of the *n*-doped hydrogenated silicon (100) surface and dehydrogenated structures at 5 K." In: *Phys. Rev. B* 80 (24 Dec. 2009), p. 245434. DOI: 10.1103/PhysRevB.80.245434. URL: http://link.aps.org/doi/10.1103/PhysRevB.80.245434.

[39] M. Berthe et al. "Electron Transport via Local Polarons at Interface Atoms." In: *Phys. Rev. Lett.* 97 (20 Nov. 2006), p. 206801. DOI: 10.1103/PhysRevLett.97.206801. URL: http://link.aps.org/doi/10.1103/PhysRevLett.97.206801.

[40] L. Esaki. "New Phenomenon in Narrow Germanium p-n Junctions." In: *Physical Review* 109 (Jan. 1958), pp. 603–604. DOI: 10.1103/PhysRev.109.603.

[41] S. Fölsch, J. Martínez-Blanco, J. Yang, K. kanisawa, and S. C. Erwin. "Quantum dots with single-atom precision." In: *Nature Nanotechnology* 9.129 (2014), pp. 505–508. DOI: 10.1038/nnano.2014.129.

[42] C. Chen, C. A. Bobisch, and W. Ho. "Visualization of Fermi's Golden Rule Through Imaging of Light Emission from Atomic Silver Chains." In: *Science* 325.5943 (2009), pp. 981–985. ISSN: 0036–8075. DOI: 10.1126/science.1174592. eprint: http://science.sciencemag.org/content/325/5943/981.full.pdf. URL: http://science.sciencemag.org/content/325/5943/981.

[43] E. H. Do and H. W. Yeom. "Electron Quantization in Broken Atomic Wires." In: *Phys. Rev. Lett.* 115 (26 Dec. 2015), p. 266803. DOI: 10.1103/PhysRevLett.115.266803. URL: http://link.aps.org/doi/10.1103/PhysRevLett.115.266803.

[44] S. Fölsch, J. Yang, C. Nacci, and K. Kanisawa. "Atom-By-Atom Quantum State Control in Adatom Chains on a Semiconductor." In: *Phys. Rev. Lett.* 103 (9 Aug. 2009), p. 096104. DOI: 10.1103/PhysRevLett.103.096104. URL: http://link.aps.org/doi/10.1103/PhysRevLett.103.096104.

[45] R. J. Hamers, R. M. Tromp, and J. E. Demuth. "Surface Electronic Structure of Si (111)-(7×7) Resolved in Real Space." In: *Phys. Rev. Lett.* 56 (18 May 1986), pp. 1972–1975. DOI: 10.1103/PhysRevLett.56.1972. URL: http://link.aps.org/doi/10.1103/PhysRevLett.56.1972.

[46] M. V. Bollinger, J. V. Lauritsen, K. W. Jacobsen, J. K. Nørskov, S. Helveg, and F. Besenbacher. "One-Dimensional Metallic Edge States in MoS_2." In: *Phys. Rev. Lett.* 87 (19 Oct. 2001), p. 196803. DOI: 10.1103/PhysRevLett.87.196803. URL: http://link.aps.org/doi/10.1103/PhysRevLett.87.196803.

[47] J. N. Crain and D. T. Pierce. "End States in One-Dimensional Atom Chains." In: *Science* 307.5710 (2005), pp. 703–706. ISSN: 0036–8075. DOI: 10.1126/science.1106911. eprint: http://science.sciencemag.org/content/307/5710/703.full.pdf. URL: http://science.sciencemag.org/content/307/5710/703.

[48] T. Matsui, C. Meyer, L. Sacharow, J. Wiebe, and R. Wiesendanger. "Electronic states of Fe atoms and chains on InAs(110) from scanning tunneling spectroscopy." In: *Phys. Rev. B* 75 (16 Apr. 2007), p. 165405. DOI: 10.1103/PhysRevB.75.165405. URL: http://link.aps.org/doi/10.1103/PhysRevB.75.165405.

[49] T. Hitosugi, T. Hashizume, S. Heike, H. Kajiyama, Y. Wada, S. Watanabe, T. Hasegawa, and K. Kitazawa. "Scanning tunneling microscopy/spectroscopy of dangling-bond wires fabricated on the Si(100)-2×1-H surface." In: *Applied Surface Science* 130–132 (1998), pp. 340–345. ISSN: 0169-4332. DOI: http://dx.doi.org/10.1016/S0169-4332(98)00081-6. URL: http://www.sciencedirect.com/science/article/pii/S0169433298000816.

[50] J. Lyding, T.-C. Shen, G. Abeln, C. Wang, P. Scott, J. Tucker, P. Avouris, and R. Walkup. "Ultrahigh Vacuum Scanning Tunneling Microscope-Based Nanolithography and Selective Chemistry on Silicon Surfaces." In: *Israel Journal of Chemistry* 36.1 (1996), pp. 3–10. ISSN: 1869-5868. DOI: 10.1002/ijch.199600003. URL: http://dx.doi.org/10.1002/ijch.199600003.

[51] P. Avouris, R. Walkup, A. Rossi, H. Akpati, P. Nordlander, T.-C. Shen, G. Abeln, and J. Lyding. "Breaking individual chemical bonds via STM-induced excitations." In: *Surface Science* 363.1

(1996), pp. 368–377. ISSN: 0039-6028. DOI: http://dx.doi.org/10.1016/0039-6028(96)00163-X.

[52] W. Kohn and L. J. Sham. "Self-Consistent Equations Including Exchange and Correlation Effects." In: *Phys. Rev.* 140 (4A Nov. 1965), A1133–A1138. DOI: 10.1103/PhysRev.140.A1133. URL: http://link.aps.org/doi/10.1103/PhysRev.140.A1133.

[53] M. Koleini. *Computational Methods in Material Science*. Lecture notes for Phys595 Principles of Nanotechnology. Edmonton, Alberta: Faculty of Physics, University of Alberta, Mar. 2015.

[54] D. C. Young. *Computational Chemistry*. John Wiley & Sons, Inc., 2002. ISBN: 9780471220657. DOI: 10.1002/0471220655. URL: http://dx.doi.org/10.1002/0471220655.

[55] S. Sadewasser and T. Glatzel. *Kelvin Probe Force Microscopy: Measuring and Compensating Electrostatic Forces*. Springer Series in Surface Sciences. Springer Berlin Heidelberg, 2011. URL: https://books.google.ca/books?id=ATQckvVUH74C.

[56] L. Cockins, Y. Miyahara, S. D. Bennett, A. A. Clerk, S. Studenikin, P. Poole, A. Sachrajda, and P. Grutter. "Energy levels of few-electron quantum dots imaged and characterized by atomic force microscopy." In: *Proceedings of the National Academy of Sciences* 107.21 (2010), pp. 9496–9501. DOI: 10.1073/pnas.0912716107. eprint: http://www.pnas.org/content/107/21/9496.full.pdf. URL: http://www.pnas.org/content/107/21/9496.abstract.